

Biometric Person Identification Using Near-infrared Hand-dorsa Vein Images

Kefeng Li

A thesis submitted in partial fulfilment for the requirements for the degree of Doctor of Philosophy at the University of Central Lancashire in collaboration with North China University of Technology

July 2013

Student Declaration

I declare that while registered as a candidate for the research degree, I have not been a registered candidate or enrolled student for another award of the University or other academic or professional institution.

I declare that no material contained in the thesis has been used in any other submission for an academic award and is solely my own work.

Signature of Candidate:

Type of Award:

Doctor of Philosophy

School:

School of Computing, Engineering and Physical Sciences

Acknowledgements

This thesis and research could not have been accomplished had it not been for the guidance and aid of multitude individuals. Many of you have had an important influence on me during my study at NCUT and UCLAN, in a variety of ways, both academic and personal. To all of you I express my sincere gratitude, and I hope I can repay you in some small ways as I can. I would like to single out the following people who had a major impact on me in the last few years.

My deepest gratitude goes first and foremost to Professor Yiding Wang, my supervisor during my master and PhD study, for his constant encouragement and guidance. He has provided a good balance of freedom and interest, while teaching me not only how to do research, but also how to write papers and give presentations. Without his consistent and illuminating instruction, this thesis could not have reached its present form.

I am also greatly indebted to Professor Lik-Kwan Shark for his supervision and introducing me into my PhD study, to Dr Martin Varley for his suggestion on all the stages of the writing of this thesis, to Dr Bogdan Matuszewski for his technical advice and consistent support. They gave me a lot of help not only in academic but also in my personal life in UK.

I would also like to express my heartfelt gratitude to the professors and teachers at the College of Information Engineering in NCUT: Professor Jingzhong Wang and Professor Jiali Cui, who have instructed and helped me a lot in the past years.

My years at NCUT and UCLAN have been priceless. The people I have met over the

years have made the experience unique and one that I will remember forever. My thanks go also to my friends and fellow classmates, Qingyu Yan, Yun Fan and Weiping Liao in IRIP in NCUT, and Qian Hong, Xingzi Tang and Lili Tao in UCLAN. They gave me their help and time in listening to me and helping me work out my problems during the difficult course of the thesis.

Last but not least, a hearty thanks to the most significant people in my life, my parents, I would have never got this far without the constant encouragement, support and love of my father and mother.

Abstract

Biometric recognition is becoming more and more important with the increasing demand for security, and more usable with the improvement of computer vision as well as pattern recognition technologies. Hand vein patterns have been recognised as a good biometric measure for personal identification due to many excellent characteristics, such as uniqueness and stability, as well as difficulty to copy or forge. This thesis covers all the research and development aspects of a biometric person identification system based on near-infrared hand-dorsa vein images.

Firstly, the design and realisation of an optimised vein image capture device is presented. In order to maximise the quality of the captured images with relatively low cost, the infrared illumination and imaging theory are discussed. Then a database containing 2040 images from 102 individuals, which were captured by this device, is introduced.

Secondly, image analysis and the customised image pre-processing methods are discussed. The consistency of the database images is evaluated using mean squared error (MSE) and peak signal-to-noise ratio (PSNR). Geometrical pre-processing, including shearing correction and region of interest (ROI) extraction, is introduced to improve image consistency. Image noise is evaluated using total variance (TV) values. Grey-level pre-processing, including grey-level normalisation, filtering and adaptive histogram equalisation are applied to enhance vein patterns.

Thirdly, a gradient-based image segmentation algorithm is compared with popular algorithms in references like Niblack and Threshold Image algorithm to demonstrate its

effectiveness in vein pattern extraction. Post-processing methods including morphological filtering and thinning are also presented.

Fourthly, feature extraction and recognition methods are investigated, with several new approaches based on keypoints and local binary patterns (LBP) proposed. Through comprehensive comparison with other approaches based on structure and texture features as well as performance evaluation using the database created with 2040 images, the proposed approach based on multi-scale partition LBP is shown to provide the best recognition performance with an identification rate of nearly 99%.

Finally, the whole hand-dorsa vein identification system is presented with a user interface for administration of user information and for person identification.

Contents

Chapter 1. Introduction	1
1.1. Background and Research Aim.....	1
1.2. Physiological and Anatomic Basis	5
1.2.1. Uniqueness.....	5
1.2.2. Time-invariance.....	9
1.3. Current Research on Vein Patterns for Biometrics	12
1.4. Thesis Organisation	14
Chapter 2. Image Acquisition Device and Database	16
2.1. Introduction.....	16
2.2. Image Acquisition Device	17
2.2.1. Infrared Illumination.....	17
2.2.2. Imaging Module	21
2.2.3. Design and Implementation.....	27
2.3. Database	30
2.4. Summary and System Approach.....	32
Chapter 3. Image Analysis and Pre-processing	34
3.1. Introduction.....	34
3.2. Geometrical Pre-processing	36
3.2.1. Analysis of Image Consistency	36
3.2.2. Geometrical Correction.....	38

3.2.3.	Region of Interest Extraction	42
3.3.	Grey-level Pre-processing.....	44
3.3.1.	Grey-level Normalisation	44
3.3.2.	Noise Measurement.....	45
3.3.3.	Noise Reduction by Filtering	47
3.3.4.	Experimental Results of Filtering	50
3.4.	Image Enhancement	53
3.5.	Summary	55
Chapter 4.	Segmentation of Vein Images.....	57
4.1.	Introduction.....	57
4.2.	Segmentation Algorithms.....	58
4.2.1.	Threshold Methods	58
4.2.2.	Boundary Methods.....	63
4.2.3.	Gradient Based Image Segmentation.....	64
4.3.	Post-processing.....	67
4.3.1.	Morphological Filtering.....	68
4.3.2.	Thinning.....	69
4.4.	Summary	69
Chapter 5.	Feature Extraction and Pattern Recognition.....	71
5.1.	Introduction.....	71
5.2.	Classification Methods.....	73
5.2.1.	Distance Measurements	73
5.2.2.	Classifiers	74

5.3.	Recognition Based on Structure Features	79
5.3.1.	Integral Features.....	79
5.3.2.	Moment Methods	80
5.3.3.	Keypoint Methods.....	82
5.3.4.	Experimental Results	87
5.4.	Recognition Based on Texture Features	90
5.4.1.	Local Binary Patterns.....	90
5.4.2.	Partition Local Binary Patterns (PLBP)	92
5.4.3.	Weighted Partition Local Binary Patterns (WPLBP).....	95
5.4.4.	Experimental Results	97
5.5.	Recognition based on multi-feature fusion	102
5.5.1.	PLBP and Vein Structure	102
5.5.2.	Multi-scale Partition Local Binary Patterns (MPLBP).....	108
5.5.3.	Experimental Results	109
5.6.	Summary	112
Chapter 6.	Software Integration with User Interface	114
6.1.	Introduction.....	114
6.2.	Overall System Design.....	114
6.3.	Software Implementation.....	115
6.3.1.	Hardware Interface.....	116
6.3.2.	Software Interface	118
6.4.	Summary	121
Chapter 7.	Conclusions and Future Work	122

7.1. Conclusions.....	122
7.2. Original Contributions.....	125
7.2.1. Image Acquisition and Database.....	125
7.2.2. Image Analysis and Pre-processing.....	126
7.2.3. Feature Extraction.....	127
7.2.4. System Integration.....	128
7.3. Future Work.....	128
References.....	130
Appendix A. Results of ROI Extraction.....	140
Appendix B. Results of Segmentation.....	165
Appendix C. Publications.....	190

List of Figures

Figure 1-1 Example of a fractal vascular tree.....	8
Figure 1-2 The veins of the dorsum hand	9
Figure 1-3 X-ray of human hand at age 2 (left), approximately 8 (centre), and 20 (right) years old,.....	10
Figure 1-4 Pictures of vein pattern recognition systems.....	14
Figure 2-1 Vein images obtained by FIR imaging in indoor and outdoor environments..	18
Figure 2-2 Infrared-absorption spectrum of water and haemoglobin, modified from	19
Figure 2-3 Vein images obtained by NIR imaging at 850nm	20
Figure 2-4 NIR imaging modes	20
Figure 2-5 Structure of imaging module	21
Figure 2-6 Spectral response of BPF-850	22
Figure 2-7 A picture of WATEC 902B CCD camera.....	23
Figure 2-8 A picture of PENTAX H1214-M (1/2')	25
Figure 2-9 A picture of Mine 2860 USB capture card	27
Figure 2-10 Schematic of the image acquisition system.....	27
Figure 2-11 Schematic and picture of the image acquisition device	29
Figure 2-12 Interface of image acquisition software.....	29
Figure 2-13 Example images obtained.....	30
Figure 2-14 Proposed approach to person identification	33
Figure 3-1 Pre-processing diagram.....	35
Figure 3-2 PSNR results.....	37

Figure 3-3 Shearing correction	40
Figure 3-4 Results of shearing correction	41
Figure 3-5 Result of ROI extraction.....	43
Figure 3-6 Result of grey level normalisation	45
Figure 3-7 Grey level profile of middle row.....	46
Figure 3-8 A diagram of TV value pixels.....	46
Figure 3-9 Time domain representation of match filter	48
Figure 3-10 Results of filtering.....	51
Figure 3-11 Grey level profiles of middle rows from original and filtered images.....	52
Figure 3-12 Results of HE and CLAHE.....	55
Figure 4-1 Result of Otsu's method.....	61
Figure 4-2 Result of threshold image method.....	62
Figure 4-3 Result of Niblack methods	63
Figure 4-4 Result of boundary method.....	64
Figure 4-5 Result of gradient based method	67
Figure 4-6 Examples of spot, hole and burr.....	68
Figure 4-7 Results of morphological filtering	68
Figure 4-8 Result of thinning.....	69
Figure 5-1 Overview of feature extraction.....	71
Figure 5-2 Integral curves of two images for the same hand.....	79
Figure 5-3 Keypoints before and after removing	83
Figure 5-4 Results of match selection	85
Figure 5-5 Example of basic LBP operator.....	91

Figure 5-6 Circular neighbourhoods for LBP operator	91
Figure 5-7 36 rotation invariant patterns produced by $LBP_{8,R}^{ri}$ operator	92
Figure 5-8 Sketches of image partitions.....	93
Figure 5-9 Feature histograms of 64 sub-images PLBP and original LBP.....	94
Figure 5-10 Feature histogram of sub-image 1.....	95
Figure 5-11 Results of vein regions extraction	104
Figure 5-12 Intra-class distance of RPLBP.....	105
Figure 5-13 Inter-class distance of RPLBP.....	105
Figure 5-14 Intra-class distance of Fusion PLBP.....	106
Figure 5-15 Inter-class distance of Fusion PLBP.....	106
Figure 5-16 Distortion samples.....	111
Figure 6-1 Workflow of vein identification system.....	115
Figure 6-2 Flowchart of software	116
Figure 6-3 Main interface.....	119
Figure 6-4 Identification mode	120
Figure 6-5 Administration interface	121
Figure A-1 Results of ROI extraction with R ranging from 300 to 420.....	164
Figure B-1 Results Segmentation Methods	189

List of Tables

Table 1-1 Comparison of different biometric features	3
Table 2-1 Components and functions of illumination and imaging modules	16
Table 2-2 Comparison of three modes.....	21
Table 2-3 Parameters and optical performance.....	24
Table 2-4 Components of acquisition device.....	28
Table 2-5 Hand-dorsa vein image databases	31
Table 3-1 Results after removing poor quality images.....	38
Table 3-2 Examples and correction methods of affine transformation	39
Table 3-3 Poor quality images before and after geometrical correction	42
Table 3-4 Comparison of results of different ROI sizes.....	44
Table 3-5 Poor quality images before and after ROI extraction	44
Table 3-6 TV values of original and filtered images	53
Table 5-1 Recognition rate (%) of integral histogram.....	88
Table 5-2 Recognition rate (%) of Hu's invariant moments	89
Table 5-3 Recognition rate (%) of Zernike invariant moments	89
Table 5-4 Result of recognition performance	90
Table 5-5 Proportions of patterns.....	96
Table 5-6 Recognition results based on individual patterns.....	96
Table 5-7 Result of training sets experiments ($N_A=1$).....	98
Table 5-8 Result of training sets experiments ($N_A=2$).....	98
Table 5-9 Result of training sets experiments ($N_A=3$).....	98

Table 5-10 Result of training sets experiments ($N_A=4$).....	98
Table 5-11 Result of training sets experiments ($N_A=5$).....	98
Table 5-12 Result of training sets experiments ($N_A=6$).....	98
Table 5-13 Result of training sets experiments ($N_A=7$).....	99
Table 5-14 Result of training sets experiments ($N_A=8$).....	99
Table 5-15 Result of training sets experiments ($N_A=9$).....	99
Table 5-16 Recognition rate (%) of using different number of training images.....	99
Table 5-17 Recognition rate (%) of RPLBP with different M and N	100
Table 5-18 Recognition rate (%) of CPLBP with different M and N	101
Table 5-19 Comparison of WPLBP and RPLBP	102
Table 5-20 The ratio of inter-class distance to intra-class distance	107
Table 5-21 Comparison of FPLBP and RPLBP.....	108
Table 5-22 Recognition rate (%) of improved PLBP	109
Table 5-23 Recognition rate (%) of different classifiers (MPLBP).....	110

List of Abbreviations

A/D	Analogue/Digital
CCD	Charge-coupled Device
CMOS	Complementary Metal Oxide Semiconductor
CPLBP	Circular Partition Local Binary Patterns
DOG	Difference-of-Gaussian
FAR	False Acceptance Rate
FIR	Far-infrared
FRR	False Rejection Rate
FOV	Field of View
GLCM	Grey Level Co-occurrence Matrix
Hb	Haemoglobin
ISO	International Standard Organization
KNN	K-Nearest Neighbourhoods
LBP	Local Binary Patterns
LED	Light Emitting Diode
MD	Mean Distance
MIR	Mid-infrared

MOS	Mean Opinion Score
MPLBP	Multi-scale Partition Local Binary Patterns
MSE	Mean Squared Error
NIR	Near-infrared
NN	Nearest Neighbourhood
PLBP	Partition Local Binary Patterns
PSNR	Peak Signal-to-Noise Ratio
ROI	Region of Interest
RPLBP	Rectangular Partition Local Binary Patterns
RR	Recognition Rate
SDK	Software Development Kit
SNR	Signal-to-Noise Ratio
SVM	Support Vector Machine
TVL	TV Line
USB	Universal Serial Bus
WPLBP	Weighted Partition Local Binary Patterns

Chapter 1. INTRODUCTION

1.1. Background and Research Aim

It is conceivable that with the rapid progress into an information-based society, security will play a more and more important role. Personal identification is the first premise for protecting privacy. In recent decades, traditional methods, such as identity card, key and certificate, have gained tremendous popularity in the field of security. Unfortunately, these methods are not only easy to copy and forge, but also hardly meet the needs of the information era demanding fast and secured digital access [Huopio, 1998, Jain, Bolle and Pankati, 1999a, NSTC, 2006a] .

Biometric feature authentication, which is a process using inherent physiological or behaviour characteristics to enable identification of individuals, is becoming an increasingly important and widely used technique for security access systems. It has higher security and reliability compared with traditional authentication methods [Biotech-Weblog, 2005, Jain, Bolle and Pankati, 1999b, Jain and Ross, 2008]. Among various biometric methods, fingerprint based verification has a higher market share due to its maturity and low cost. However, there is no denying that it has some disadvantages, for example, it is easy to alter and forge, owing to the use of surface features.

From the operational viewpoint, identification work could be easier by using biometric methods. For administrators, it requires less management operations; for users, they just need to bring themselves. Furthermore, it is more robust due to their uniqueness. This is the reason that biometrics, such as iris and fingerprint, become the only choice in

Chapter 1. Introduction

some security departments like banks and national defence.

Adoption of a biometric feature for a particular application requires consideration of the following characteristics [Biotech-Weblog, 2005, Clarke, 1994, Jain, Bolle and Pankati, 1999b, Jain, Hong and Pankati, 1999]:

- 1) Uniqueness: unique feature patterns from each individual.
- 2) Stability: feature pattern invariant with time unless it is changed by external factors.
- 3) Universality: feature available from all people.
- 4) Acceptance: the extent of accepting the feature to be used by people.
- 5) Security: difficulty for the feature to be forged and copied.
- 6) Timeliness: time required to obtain and process the feature.
- 7) Acquisition: ease of acquisition of the feature.

To provide better biometric performance, some new features which are more effective than fingerprints have been investigated, such as vein patterns studied in this project. Recently, more and more emphasis is paid to hand-dorsa vein patterns [Jain, Bolle and Pankati, 1999a, Zhang, 2000]. As hand-dorsa veins can hardly be changed except by surgery, its pattern could be used as a secure and robust feature for personal identification.

Generally, biometric features can be classified into static features (hand shape, fingerprint, iris, face, signature, vein etc.) and dynamic features (voice, gait etc.). Adopted from [Jain, Hong and Pankati, 1999, Khairwa, Abhishek, Prakash *et al*, 2012], a

Chapter 1. Introduction

comparison of different biometric features is shown in Table 1-1.

Table 1-1 Comparison of different biometric features

Features	Finger-print	Iris	Voice	Face	Signature	Hand shape	Hand-dorsa Vein
Uniqueness	H	H	L	L	L	M	H
Stability	H	H	L	M	L	M	H
Universality	M	H	M	H	H	M	H
Acceptance	M	L	H	H	H	M	H
Security	H	H	L	L	L	M	H
Timeliness	H	H	L	L	L	M	H
Ease of Acquisition	M	M	M	H	H	H	M

(H: High M: Medium L: Low)

As can be seen from Table 1-1, hand-dorsa vein patterns have high scores in 6 out of 7 categories. In terms of uniqueness, even considering the right hand and left hand of the same person, and the hands of twins, the vein pattern features are different. In terms of stability, vein structure remains the same unless it is changed by surgery or some bone illnesses. In terms of acceptance, hand-dorsa vein images can be obtained by contact-less methods, which makes it easy for people to accept it. Finally, in terms of security, as a kind of characteristics of living bodies, it is hard to forge. Hence, hand-dorsa vein patterns have the potential of taking the place of the fingerprint for personal identification.

The adoption of a biometric feature for a particular application depends on their characteristics. The strengths and weaknesses of some widely studied biometric features are given in the following.

1) Fingerprint [Galy, Charlot and Courtois, 2007, Jain, Halici, Hayashi *et al*, 1999, NISTC, 2006d]

Fingerprints are the most widely used biometric feature for personal identification and commands around half of the total biometric market. It is convenient and mature, and

Chapter 1. Introduction

it has a long history of development. However, there are some technical difficulties which are not solved, such as easy to forge, hard to process noisy images.

2) Iris [Daugman, 2003, Daugman, 2004, He, Tan, Sun *et al*, 2008, NSTC, 2006e]

The iris highly unique and secure because of its complex texture. But two main drawbacks exist. One is low acceptance because it makes many users feel uncomfortable during image capture. The other is expensive devices. Hence, it is usually used in some high security departments.

3) Face [Brunelli and Poggio, 1993, Goldstein, Harmon and Lesk, 1971, Kirby and Sirovich, 1990, NSTC, 2006c]

As known to all, almost all the human beings identify others by face. So that it is a universal feature. However, it performs well only under controlled illumination and expression. Other issues include facial changes caused by aging.

4) Signature [Chapran, 2006, Faundez-Zanuy, 2007, NSTC, 2006b]

Signatures have been used as an authentication method for hundreds of years, and it is still in use in daily life. Nevertheless, it varies with the changes of environment, age, temperament etc. Therefore, it is not stable. Furthermore, it is easy to forge because a person can be trained to imitate the signature of others.

5) Gait [Johansson, 1973, Johansson, 1975, McGeer, 1990]

Gait is a viable means to filter the groups of interest at public areas, such as stations, airports and shops. Its computing complexity is high due to the high volume of data. Although there is much research in this area, it is hard to build an identification system

with good performance.

Although the fingerprint has the biggest market share in biometrics now, the vein pattern could emerge as another leading player if its problems related to application and commercialisation are solved. This leads to the project to build a framework of the vein pattern identification system with the required hardware and software for real application and commercialisation.

The aim of this project is to develop an accurate and efficient personal identity verification system based on hand-dorsa vein patterns. It will offer greater convenience (e.g. easier acquisition of data) and higher security (e.g. harder to falsify data) compared to more established biometric verification methods, with a comparable or improved recognition rate.

1.2. Physiological and Anatomic Basis

One of the most important conditions of an identification system based on a biometric feature is that it has a unique and time-invariant property for every individual, and that this property can somehow be captured and processed by an automated system. Therefore, if the hand vein pattern is the property upon which the identification process is based, it should comply with these conditions. In this section, the properties of the hand vein pattern concerning uniqueness and time-invariance are discussed.

1.2.1. Uniqueness

Although many papers state that the hand vein pattern is a unique property of each individual [Badawi, 2006, Choi, 2001, Fujitsu, 2003], scientific research on the uniqueness of veins in the hand is sparse. The mechanisms underlying the development

Chapter 1. Introduction

of the vascular system and studies on the spatial arrangement of the final vascular network could provide more evidence that no vein pattern will be the same between two individuals.

A. Vascular Development [Eichmann, Yuan, Moyon *et al*, 2005]

The smallest vessels of the vascular system, the capillaries, are composed solely of endothelial cells and are surrounded by a basement membrane. Larger vessels, such as arteries and veins, have additional layers constituting the vessel wall, which are composed of a muscular layer, an outer connective tissue layer and nerves. The endothelial cells represent the major cellular compartment of the vascular system.

Vascular endothelial growth factor (VEGF) and its receptor (VEGFR2) are the most critical drivers for embryonic vessel formation. The *in situ* differentiation of endothelial cells from the mesoderm and their fusion into tubes of the primary capillary system under the influence of VEGF is called vasculogenesis. Vasculogenesis results in the formation of the major embryonic vessels. Next, this primary system has to be remodelled into a system with arteries and veins, to accommodate the heart and to establish the primary circulation.

For a long time it was believed that differentiation into veins and arteries was influenced by haemodynamic forces. Recently, signalling molecules have been discovered to be present in early development stages in endothelial cells, already labelling them arterial or venous.

In addition, other recent research identified neural guidance receptors, which are expressed on arteries and veins. In the nervous system, these molecules are implicated in

Chapter 1. Introduction

establishment of cell boundaries and in the guidance of developing axons. Recent studies have shown that specialized cells ('tip' cells) are present at the ends of developing vessel sprouts, with extending sensors that explore their environment in much the same way as the growth cone of a developing axon. Moreover, the patterning of developing arteries in the limb skin of mouse embryos has been shown to depend on interactions with nerves.

As all the factors discussed above have their contributions to vascular systems development, any change of each factor would make the system different. Hence, the vascular system of each individual is more likely unique.

B. Spatial Arrangement

In vascular system development, the process of migration and dynamic aggregation results in a network that exhibits fractal behaviour on a small scale and on a large scale [Gamba, Ambrosi, Coniglio *et al*, 2003]. A fractal denotes a shape that is recursively constructed or self-similar, that is, a shape that appears similar at all scales of magnification and is therefore often referred to as "infinitely complex" [Mandelbrot, 1983].

Whether the *in vivo* spatial arrangement of vascular systems exhibits fractal behaviour is a popular basis for some of the proposed models for vascular spatial arrangement [Dokoumetzidis and Macheras, 2003, Ippolito, Peretti, Bellocci *et al*, 1994, West, Brown and Enquist, 1997]. If the blood vessel system can be considered having a fractal-like structure, it should be quite homogenous and containing the similar branching characteristics throughout the body, which is shown in Figure 1-1.

Chapter 1. Introduction

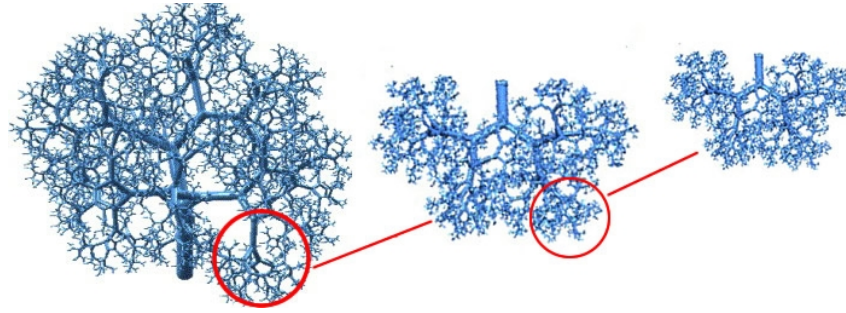


Figure 1-1 Example of a fractal vascular tree, modified from [Gabryśa, Rybaczuka and Kędziab, 2005]

Several studies found quasi-fractal structures in coronary patterns, because the branching parameters were not always identical but ranged between certain values [Zamir, 1999]. The pulmonary or renal vascular networks provide a processing function, which is supported by a uniform distributed vascular system. On the other hand, the remaining vascular network has a purely metabolic function that is primarily based on providing blood to all parts of the body, and is less uniformly distributed. Therefore, the latter is unlikely to contain a higher degree of fractal character, and a model based on branching geometry may be more appropriate for trees with a metabolic function such as the hand vein system.

A general biological model developed by West *et al.* [West, Brown and Enquist, 1997] predicts the essential features of transport systems and is based on three unifying principles: (1) a space-filling fractal-like branching pattern to supply the entire volume; (2) final branch of the network is a size-invariant unit; and (3) the energy required to distribute resources is minimised (minimising the total hydrodynamic resistance of the system). The last restriction will reduce homogeneous diffusion of vascular systems [Schreiner, Karch, Neumann *et al.*, 2003]. Perfusion heterogeneity is also described by [Marxen and Henkelman, 2003], in a model based on two parameters: branching asymmetry and the scaling properties (or fractal dimensions) of vessel resistance.

Chapter 1. Introduction

Branching asymmetry is based on the tissue volume that is fed by each vessel, and the fractal relationships for the length and diameter exist as a function of scale.

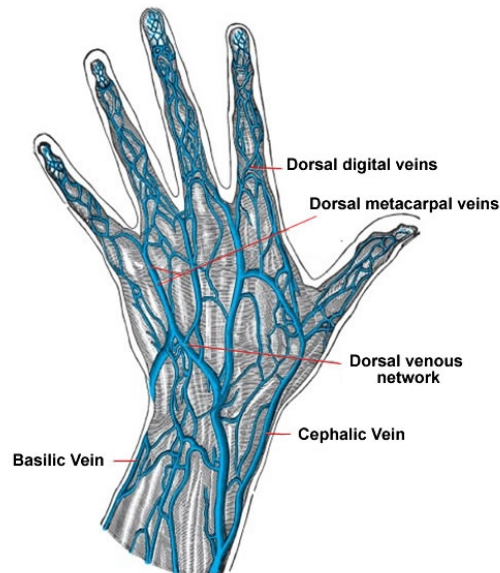


Figure 1-2 The veins of the dorsum hand, modified from [Gray and Standring, 2008]

Based on the analysis above, hand vein system is hard to be the same for its metabolic function, requirement of minimising the total hydrodynamic resistance of the system and perfusion heterogeneity. Figure 1-2 illustrates the generic vein map found on the dorsum hand. There are mainly two types of hand-dorsa veins, namely cephalic and basilic. The basilica veins are the group of veins attached with surface of hand, which will be the primary focus in this project.

1.2.2. Time-invariance

A biometric feature used to identify individuals is only useful when the feature measured at different time has not changed significantly. In other words, the features of the biometric property should be time-invariant. In case of the human hand vein pattern, two processes might change the pattern. One is natural change in the vascular system

Chapter 1. Introduction

throughout the life span of a healthy human being. The other one is non-natural change in the vascular system that is associated with some diseases or surgery. This section will reflect upon these two processes.

A. Natural vascular changes

The changes in the vascular system throughout a human life actually start with the development of the vascular tree in the embryonic phase, which has been discussed in section 1.2.1.

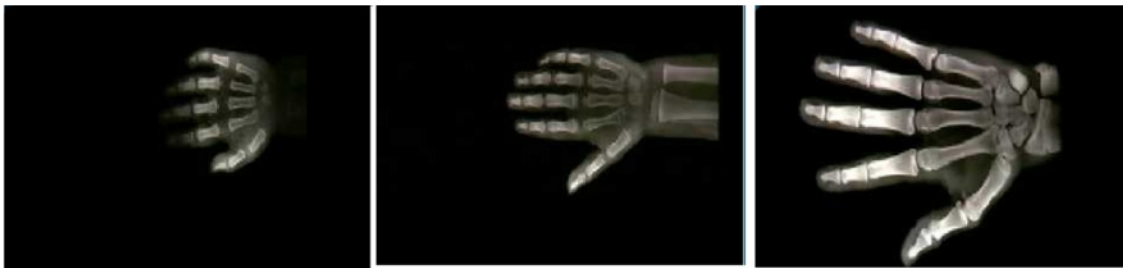


Figure 1-3 X-ray of human hand at age 2 (left), approximately 8 (centre), and 20 (right) years old, adopted from [BBC, 2012]

In this phase, the biggest changes are made as it grows from single cells into a whole network. After birth, the veins grow as the body grows. The length of the veins in the body will extend in the first 18 to 20 years of life [BBC, 2012, Riggs, Khosla and Melton, 1999]. In hands cartilage is being replaced by bones and they will develop into longer and thicker bones during childhood and puberty (see Figure 1-3). During adult life, no major skeletal growth occurs. On the contrary, at a certain point in life, the balance between bone formation and restoration is reversed. This leads to a loss over a lifetime of about 15% of the total skeletal mass in men and 30% in women. The function of the vascular networks is to provide oxygen to all places in the body and therefore it will adapt to the size of the body. It will extend and shrink throughout life, with major changes before 20

Chapter 1. Introduction

and minor changes during the ageing process from 20 years on. Also there is an inevitable slow decline in strength of bones and muscles in an ageing body due to a poorer blood supply to muscles [Rubins, 2012]. Other factors that influence the vascular system during a normal life are the environmental temperature, physical activity and the use of alcohol. This last factor should not be considered as unhealthy use of alcohol, which may result in permanent pathological changes in the vessels, but rather the temporary influence of alcohol while it is in the body. In this way alcohol is a vessel dilator: in healthy people it increases blood flow, reduces vessel resistance and therefore the blood volume increases [Conrad and Green, 1964]. Vessels also dilate if the body temperature is too high; the blood flow can increase 150 times to loose excess heat. In cold weather skin will constrict blood vessels and release heat loss During physical activities the vessels will also dilate to provide enough oxygen to the muscles [Cross and Smith, 1995].

B. Non-natural vascular changes

The vascular system is a large and essential system in the human body. Like almost all tissues, cells of the vascular system are continually replaced by new cells throughout life, which forms a dynamic structure of several layers. Due to the dynamic character of the vascular system, it is sensitive to conditions of the body that deviate from normal or healthy.

Diabetes, hypertension, atherosclerosis [Hoeks and deMay, 2002], metabolic diseases [Carretero, 2005] or tumours [Carmeliet and Jain, 2000] are deviated conditions which can remodel the vascular system. The first four examples induce an effect on the mechanical properties of the vessel wall, which gives rise to haemodynamic changes. The

Chapter 1. Introduction

endothelium is thought to be the main shear sensor and the cytoskeleton plays in general a key role in biological responses to mechanical factors [Hoeks and deMay, 2002]. Also mechanisms that are independent of the changes in pressure, e.g. new signalling pathways and signalling molecules, can participate in the mechanisms of vascular remodelling, shown by research on hypertension [Risler, Cruzado and Miatello, 2005]. The remodelling process results in thickening or thinning of the vessel wall, in both lumen and the external diameter.

Angiogenesis, a hallmark of cancer and various ischaemic and inflammatory diseases [Carmeliet, 2005 , Carmeliet and Jain, 2000], also influences the vascular system during disease. ‘Angiogenesis is a physiologic process which refers to the remodelling of the vascular tissue characterised by the branching out of a new blood vessel from a pre-existing vessel [D'Andrea, Del Gatto, Pedone *et al*, 2006]. It is related to the proliferation and migration of endothelial cells (ECs).

Another clinical interference in vessel formation can be surgery, the most common being the so-called bypass operation. The goal of coronary bypass surgery is to increase coronary artery blood flow. Healthy arteries or veins are ‘harvested’ and used to channel the needed blood flow around the blocked portions.

In summary, hand-dorsa vein system of an adult could be stable for a long time, which satisfies the biometrics requirement of time-invariant.

1.3. Current Research on Vein Patterns for Biometrics

As a new means of biometric recognition, vein patterns have attracted significant attention in the research community recently. Compared with more established biometric

Chapter 1. Introduction

verification methods, such as fingerprint, face and iris, vein patterns have higher convenience and higher security [Delac and Mislav, 2004, Ding, Zhuang and Wang, 2005].

The vein images are mostly obtained by Near-Infrared (NIR) imaging methods. NIR imaging has three modes, transmission, reflection and hybrid mode [Kumar and Prathyusha, 2009, Wang and Leedham, 2006]. In 1992, Shimizu discussed optical trans-body imaging and potential optical CT scanning applications [Shimizu, 1992]. In 1996, Yamamoto, in conjunction with Shimizu, presented another paper in which the two discussed the research they had undertaken since the earlier paper [Shimizu and Yamamoto, 1996]. In these two papers, NIR imaging methods to obtain pictures of subcutaneous tissues were proposed.

The first research paper about the use of vein patterns for biometric recognition was published in 2000 [Im, Park, Kim *et al*, 2000]. This paper presented a method that used a high-cost DSP processor suitable for floating-point operations and a real-time processor to optimise the recognition time. With an authentication reliability of 99.45% and a computation speed of 150 ms/person, it becomes the first commercially available vein pattern identification system in 2000. NEXTERN Corporation in Korea produced four hand-dorsa vein identification systems, BK100, BK200, BK300 and BK500 [Mainguest, 2012]. Fujitsu in Japan built an authentication system based on palm vein patterns with a reliability of 100% based on around 1000 checks [Fujitsu, 2003]. Figure 1-4 shows these two types of vein pattern recognition systems.



(a) BK Series by NEXTERN [Mainguest, 2012] (b) Fujitsu product [Fujitsu, 2003]

Figure 1-4 Pictures of vein pattern recognition systems.

In China, the research about vein pattern recognition began later than some other countries. In 2002, Lin *et al.* showed a self-made capturing device and the processed vein images [Lin, Zhuang, Su *et al.*, 2003]. In 2006, they presented an algorithm in which watershed transformation was firstly used to extract Feature Points of Vein Patterns (FPVP) from the images of hand-dorsa vein patterns with the False Acceptance Rate (FAR) of 2.6% and False Rejection Rate (FRR) of 4.7% [Zhou, Lin and Jia, 2006]. In 2005, Wang *et al.* presented a paper in which they proposed their improvements on pre-processing and segmentation [Ding, Zhuang and Wang, 2005].

As the vein pattern technology developed, related products started to be adopted by some departments. In the 2008 Beijing Olympic Games, hand-dorsa vein identification devices were used at the Women's Softball Centre [Ningbo-Website, 2007]. In the latest survey, vein pattern takes up only 3% in the security market, while fingerprint accounts for 25.3%. Hence, the vein pattern technology has a good development prospect.

1.4. Thesis Organisation

This thesis consists of seven chapters. The rest of the thesis is organised as follows.

In chapter 2, design and realisation of a low-cost vein image-capturing device is presented, while the hand vein images database obtained with it is introduced.

Chapter 1. Introduction

Chapter 3 discusses image consistency assessment and customised pre-processing methods which include geometrical correction, region of interest extraction, grey level normalisation, noise reduction and image enhancement.

In chapter 4, a gradient-based image segmentation algorithm is compared with popular algorithms in references like Otsu, Threshold Image and Niblack. Post-processing methods including morphological filtering and thinning are also presented.

Chapter 5 investigates some common structure and texture features, such as integral histogram and invariant moments, and proposes new feature extraction and recognition methods based on keypoints and partition local binary pattern (PLBP). Some classifiers, like NN, KNN and SVM are also studied in Chapter 5.

Chapter 6 gives an overview of a hand-dorsa vein recognition system developed and details of the software programmed with Visual C++ 6.0.

Finally, chapter 7 concludes this thesis by summarising the original contributions and provides an overview of possible future work.

Chapter 2. IMAGE ACQUISITION DEVICE AND DATABASE

2.1. Introduction

The first hand vein pattern images acquisition device was implemented by Im et al in 2000, in which a high-cost DSP processor suitable for floating-point operations and a real-time processor were used to improve the recognition time [Im, Park, Kim *et al*, 2000]. Figure 1-4 shows a BK series of hand-dorsa vein verification systems and a type of palm vein authentication system.

The principle and design of a hand-dorsa vein image acquisition device is discussed in this chapter. This device consists of an illumination module and an imaging module, the components of which are shown in Table 2-1

Table 2-1 Components and functions of illumination and imaging modules

Modules	Components	Functions
Illumination	series of Near-infrared (NIR) light emitting diode (LED)	enhance vein pattern by near infrared light
Imaging	camera, lens, optical filter, capture card	capture and save hand-dorsa vein images

A database, which contains 2,040 hand-dorsa vein images obtained from 102 individuals (52 females and 50 males), was created using the device implemented. Details and comparison with other databases will be also discussed in this section.

2.2. Image Acquisition Device

2.2.1. Infrared Illumination

Infrared imaging is classified into Far-infrared (FIR), Mid-infrared (MIR) and Near-infrared (NIR) imaging with the wavelength of 5~40 μm , 1~5 μm and 0.75~1 μm respectively. FIR and NIR are usually adopted to capture vein images. The two modes work in different ways. The former obtains images by receiving the infrared light radiated by the human body, which is easily influenced by the surroundings; and the latter captures images through the reflection or transmission of infrared light generated by infrared sources, which depends on the different absorption of infrared light between blood and other tissues [Wang and Leedham, 2006]. NIR imaging is generally adopted for acquisition of vein images.

A. FIR imaging principle

Every object could radiate infrared light, and human bodies emit infrared radiation at a wavelength of about 10 μm . The relationship of power density P and temperature [Cole and Woolfson, 2002] is given by:

$$P = e\sigma_{SB}T^4 \quad (\text{Js}^{-1}\text{m}^{-2}) \quad (2-1)$$

where, e is emissivity of the object, $\sigma_{SB}=5.67\times 10^{-8}\text{Js}^{-1}\text{m}^{-2}\text{K}^{-4}$ is Stefan-Boltzmann constant, and T is absolute temperature in K. The relationship between wavelength λ and temperature T [Cole and Woolfson, 2002] is given by:

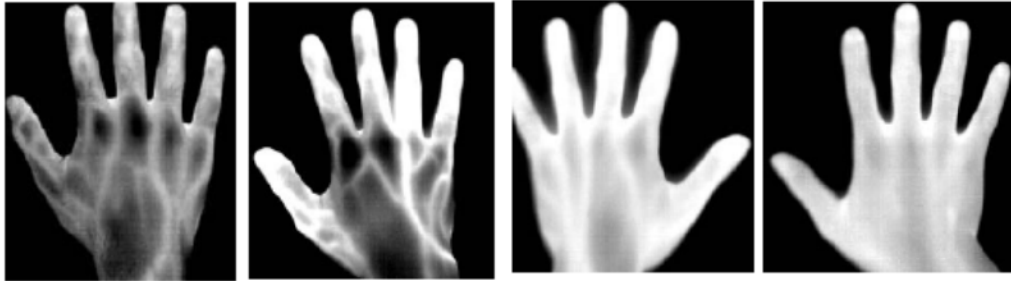
$$l = \sigma_w / T \quad (\text{m}) \quad (2-2)$$

where $\sigma_w=2.9\times 10^{-3}$ mK is Wien's displacement constant. As can be seen from equations (2-1) and (2-2), when the temperature is higher, the power is higher, and the wavelength is shorter.

Chapter 2. Image Acquisition Device and Database

FIR imaging obtains vein images by receiving the infrared light radiated by the hand-dorsa area. Because the vein temperature is higher than other tissues, the radiation power is higher, and the vein on the image is brighter than other parts of the hand. While the wavelength of the human body radiation is 3~14 μm , the wavelength of visible light is 0.4~0.7 μm . Hence, the vein images are hardly affected by visible light.

However, FIR imaging could be influenced by environment. If the environment were warm, the contrast between veins and other parts would be low; and if the environment were humid, there would be more shadows on the vein images. Furthermore, the FIR device is very expensive, and it is impossible to realise it with low cost, which is a requirement of the project. Figure 2-1 [Wang and Leedham, 2006] shows example images captured by FIR.



(a) Indoor

(b) Outdoor

Figure 2-1 Vein images obtained by FIR imaging in indoor and outdoor environments.

B. NIR imaging principle

When NIR illuminates the hand, due to the tissues' inhomogeneity, light will be transmitted, reflected and scattered. A NIR camera is used to get images by capturing the transmitted, reflected and scattered NIR light.

NIR imaging is based on the discovery in biomedicine. Research indicates that light

Chapter 2. Image Acquisition Device and Database

with wavelengths of 700~800 nm could pass through skin, and that infrared light with wavelengths shorter than 800 nm could easily travel through water, which is the main element of the human body. However, haemoglobin, the main ingredient of blood, absorbs infrared light differently to water, as shown in Figure 2-2.

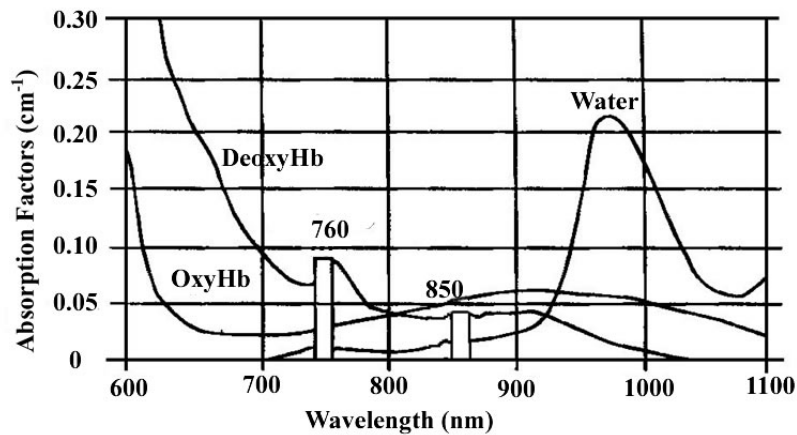


Figure 2-2 Infrared-absorption spectrum of water and haemoglobin, modified from

[Chen, Li and Lu, 2000]

As can be seen from the above graph, haemoglobin (Hb), including OxyHb and DeoxyHb (with or without oxygen), reaches absorption peak between 700 nm to 900 nm (DeoxyHb: 760 nm, 850 nm; OxyHb: 900 nm), and its absorption factor is higher than water before 900 nm. Considering there is more DeoxyHb than OxyHb in vein blood, infrared sources of 760 nm or 850 nm could be used for illumination. Although the absorption factor of DeoxyHb is higher at 760 nm than it is at 850 nm, the NIR light sources of 760 nm cost more with fewer choices, compared with NIR LED of 850 nm. Hence, an 850 nm NIR source is selected for image capture. Sample images obtained from the left and right hands of a person by NIR imaging with 850 nm LED are shown in Figure 2-3.

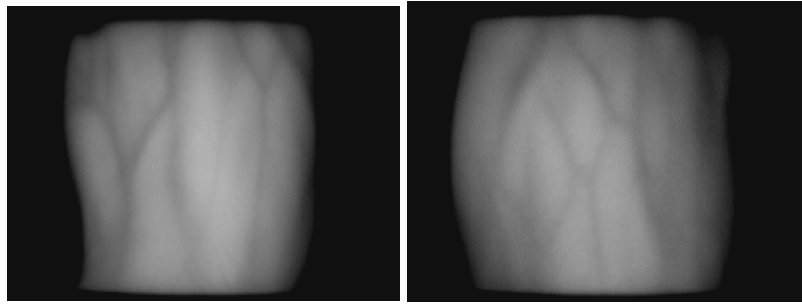


Figure 2-3 Vein images obtained by NIR imaging at 850nm

C. NIR imaging modes

NIR imaging has three modes, transmission, reflection and hybrid mode. They are shown in Figure 2-4.

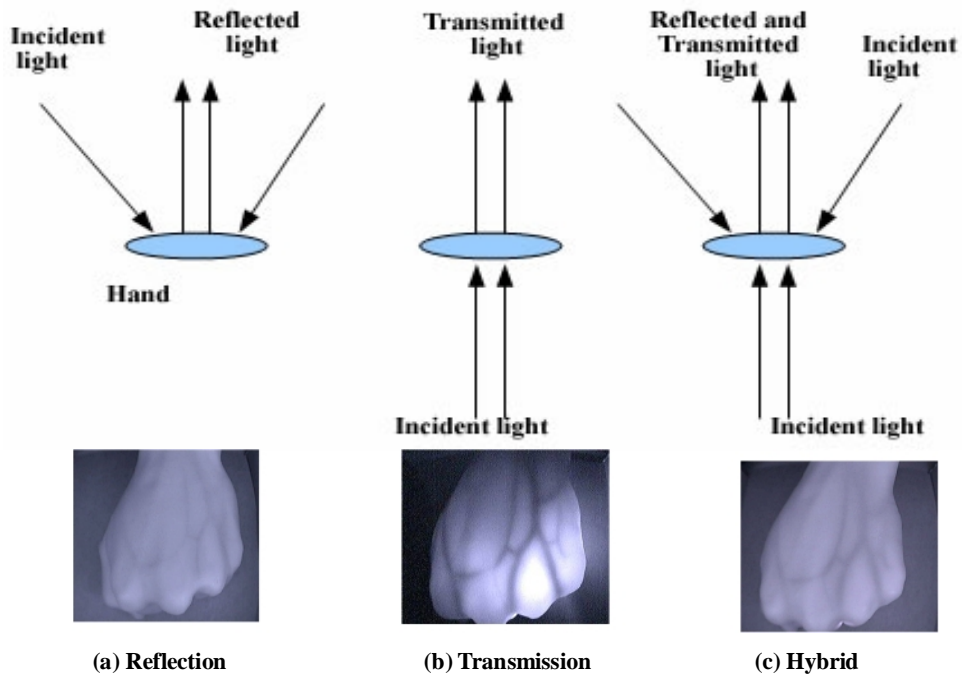


Figure 2-4 NIR imaging modes

A comparison of the three modes is shown in Table 2-2.

Table 2-2 Comparison of three modes

	Advantages	Disadvantages
Reflection	High contrast after optimising Low cost Low power	High quality requirement for NIR sources and components
Transmission	High contrast	Inhomogeneity in images with contrast differences between regions
Hybrid	Higher definition and contrast than images obtained by reflection	Complicated and high cost

Reflection mode is selected for the implementation, because it is low cost and hardly affected by environment. Furthermore, the images quality is good enough with hand veins visible and can be further improved by increasing illumination intensity and coverage as well as image processing.

2.2.2. Imaging Module

The imaging module consists of a lens and an optical filter to control the incident light to improve the image quality and a camera to form images by capturing the light through the lens and optical filter. The structure of the imaging module is shown in Figure 2-5.

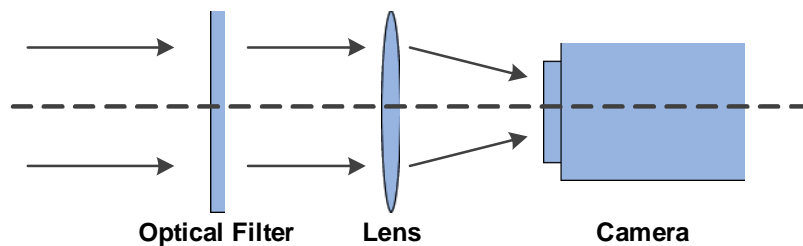


Figure 2-5 Structure of imaging module

A. Optical filter

Infrared optical filters are classified into infrared-pass filters, infrared-cut-off filters, and infrared-band-pass filters. Considering the NIR imaging principle and the cost, an infrared-band-pass filter is selected. As shown in Figure 2-6, BPF-850 has the centre

Chapter 2. Image Acquisition Device and Database

wavelength of 850 nm, a half-main-lobe width of 60 ± 10 nm and its transmittance at 850 nm is 91.99%.

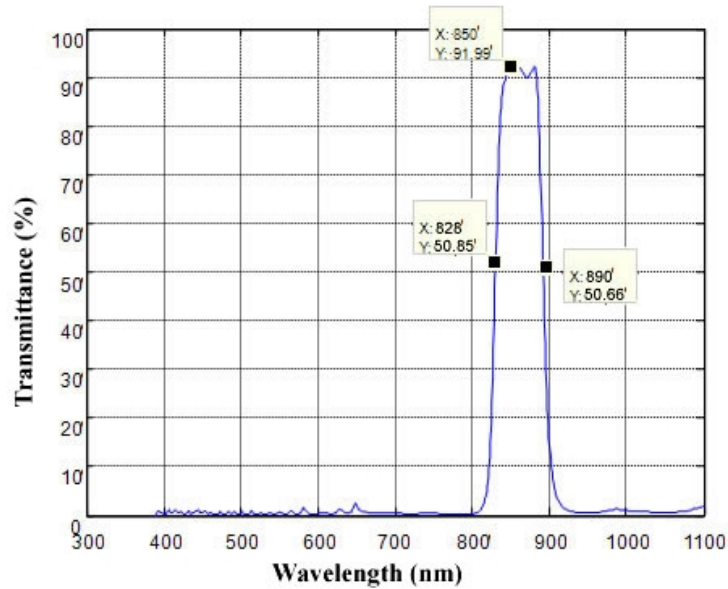


Figure 2-6 Spectral response of BPF-850, modified from [Accute Optical Tecnology Co., 2012]

B. Camera

Cameras usually use two kinds of imaging sensors, Charge-coupled Device (CCD) and Complementary Metal Oxide Semiconductor (CMOS). Both of them can convert light into electric charge and process it into electronic signals. It is better to select a CCD imager for capturing vein images because of its higher precision [Alper, 2011].

There are two basic parameters of CCD cameras, the pixel scale and the field of camera view, which should be considered in order to choose the right camera. The pixel scale is used to determine whether an object that is a small round spot is covered by enough pixels to appear as a round spot in the resulting image. After achieving the right pixel scale, a larger field of view can be obtained by purchasing a CCD camera with a larger CCD chip.

Chapter 2. Image Acquisition Device and Database

As researchers on hand-dorsa vein recognition usually use images with resolutions of 640×480 pixels, the camera should satisfy this requirement. For the same resolution, the bigger the CCD chip, the higher the image quality. Thus, the CCD chip of the camera should be as big as possible under a certain cost. A common size of industrial grade camera CCD chip at 1/2 inch is chosen. Integrating the various requirements, a WATEC 902B CCD camera shown in Figure 2-7 is finally selected. Its main parameters are listed as follows [Watec Co., 2010]:

- Physical size: $35.5 \times 36 \times 58$ mm
- Scanning system: 2:1 interlace
- Resolution: 570 TVL
- Effective pixels: 752 (H) \times 582 (V)
- Unit cell size: $8.6 \mu\text{m}$ (H) \times $8.3 \mu\text{m}$ (V)
- S/N: 50dB
- Power: DC12 V \times 160 mA
- Minimum illumination: 0.003 Lux F1.2



Figure 2-7 A picture of WATEC 902B CCD camera

Chapter 2. Image Acquisition Device and Database

C. Lens

A camera lens is an optical lens used in conjunction with a camera body to make images of objects.

The two fundamental parameters of an optical lens are the focal length f and the maximum aperture D . The lens' focal length determines the magnification of the image projected onto the image plane and the angle of view. The aperture determines the light intensity of the image and the depth of field.

The maximum usable aperture of a lens is specified as the focal ratio or f-number F [Smith, 2007], which can be calculated by:

$$F = f / D \quad (2-3)$$

where, f is the focal length in mm, and D is the maximum aperture (or entrance pupil) in mm. A smaller f-number leads to higher light intensity at the focal plane.

The effects of main parameters on the optical performance of lens are shown in Table 2-3

Table 2-3 Parameters and optical performance

Parameters	Optical Performance
Focal length (short)	Depth of field: deep Distortion: high Vignetting: big
Aperture (small)	Illumination: weak Depth of field: deep Resolution: low
Image field (small)	Higher resolution in centre, strong illumination
Incident wavelength (short)	Resolution: high

To get a hand-dorsa vein image, the field of view (FOV) should be bigger than $8 \text{ cm} \times 8 \text{ cm}$. Moreover, the camera is about 15 cm far from the hand, thus the focal length f could be calculated by [Smith, 2007]:

Chapter 2. Image Acquisition Device and Database

$$f = wE / W \quad (2-4)$$

$$f = hE / H \quad (2-5)$$

where, w and h are the width and height of CCD chip, W and H are the width and height of the field of view, E is the distance between hand and camera, the unit of all of them is in mm. For the chosen camera, WATEX 902B, the size of CCD chip is $4.8 \text{ mm} \times 6.4 \text{ mm}$, which leads to a focal length of $9 \text{ mm} \sim 12 \text{ mm}$. Considering the stability of device and that a prime lens of 12 mm focal length is easily obtained, a PENTAX H1214-M (1/2') shown in Figure 2-8 is adopted in this work. Its main parameters are listed as follows [PENTAX Precision Co., 2012]:

- Size: $\phi 34.0 \times 43.5 \text{ mm}$
- Focal length: 12 mm
- Relative aperture: F1.4
- FOV (D/H/V, mm): (102.3~47.6/81.3~38.2/60.4~28.7)



Figure 2-8 A picture of PENTAX H1214-M (1/2')

D. Capture Card

The function of capture card is to do Analogue/Digital (A/D) conversion and data transmission. Its parameters refer to the selected CCD camera. In this work, it should satisfy the following requirements:

Chapter 2. Image Acquisition Device and Database

1) Colour depth

8-bit grey image or 16/24/32 bit colour image. As colour information is not required in this work, 8-bit grey image is selected to save storage space.

2) Decoder mode

Phase Alternating Line (PAL).

3) Output resolution

It should be higher than camera resolution. Here it should be higher than 640×480 pixels.

4) Interface mode

In this work, image resolution is 640×480 pixels, and the frame rate is 25 frames per second. To guarantee the real-time preview and capture, the transmission speed should be higher than 60Mbps, which can be satisfied by 1394 FireWire and Universal Serial Bus (USB) mode. Considering the convenience and low cost, USB mode is the best choice.

5) Software Development Kit (SDK)

A SDK package should be provided to develop capture software.

Based on the analysis above, Mine 2860 USB capture card shown in Figure 2-9 is adopted, the parameters of which are shown as follows [Shenzhen Mine Technology Co., 2013]:

- Size: 103×60×19 mm
- Interface port: USB 2.0

Chapter 2. Image Acquisition Device and Database

- Standard: PAL, NTSC
- Resolution: 720×576, 640×480, 352×288



Figure 2-9 A picture of Mine 2860 USB capture card

2.2.3. Design and Implementation

The structure of the image acquisition device is illustrated in Figure 2-10.

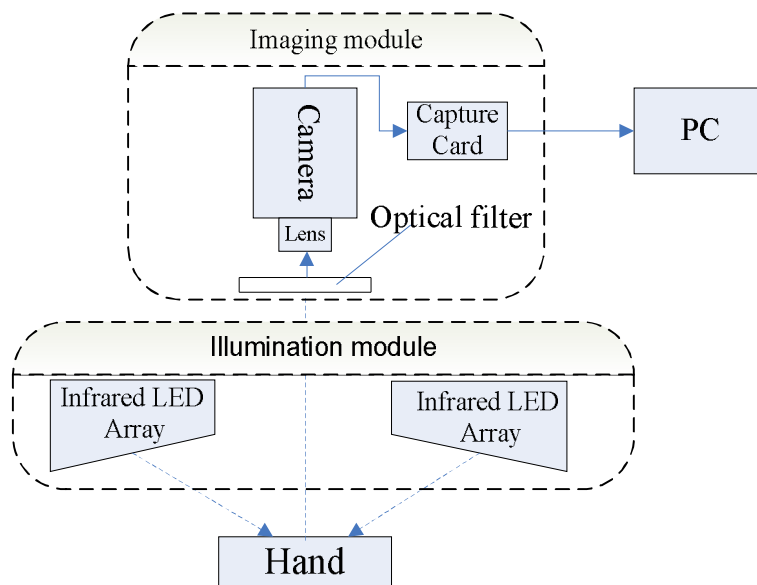


Figure 2-10 Schematic of the image acquisition system

The hand reflects NIR light coming from infrared LED arrays with 850 nm wavelength to CCD sensors of the camera through an infrared filter and lens, forming an image of hand-dorsa vein.

Chapter 2. Image Acquisition Device and Database

Based on the analysis in section 2.2, the components adopted in this work are shown in Table 2-4.

Table 2-4 Components of acquisition device

Modules	Components	Parameters
Illumination	2 Near-infrared LED array (reflection)	Size: ϕ 8 mm LED Type: Round LED Power: 1.5 V \times 200 mA Wavelength: 850 nm Array size: 3 \times 3 Lighting distance: 100 mm Distance between 2 LED arrays: 56 mm (at two sides of the CCD camera)
Imaging	Camera: WATEC 902B CCD (1/2')	Size: 35.5 \times 36 \times 58 mm Scanning system: 2:1 interlace Resolution: 570 TVL Effective pixels: 752 \times 582 Unit cell size 8.6 μ m \times 8.3 μ m S/N: 50 dB Power: DC12 V \times 160 mA Minimum illumination: 0.003 Lux F1.2
	Lens: Pentax H1214-M(KP) (1/2')	Size: ϕ 34.0 \times 43.5 mm Focal length: 12 mm Relative aperture: F1.4 FOV(D/H/V, mm): (102.3~47.6/81.3~38.2/60.4~28.7)
	Optical filter: 850 nm	Size: ϕ 30.0 \times 3 mm Half-main-lobe width: 60 \pm 10 nm Transmittance: 91.99%
	Capture card: Mine V2860 USB	Size: 103 \times 60 \times 19 mm Interface port: USB 2.0 Standard: PAL, NTSC Resolution: 720 \times 576 Dynamic adjusting

To reduce the influence of visible light, a box with black spraying plastic is designed to cover the camera, lens and infrared LED sources. A handle is added to limit the hand position to improve the image quality. Then a new handle is designed to make it more comfortable and a new box is adopted to improve the appearance. The implementation of the image acquisition device is shown in Figure 2-11.

Chapter 2. Image Acquisition Device and Database



Figure 2-11 Schematic and picture of the image acquisition device

Image acquisition software is programmed using visual C++ 6.0 with the SDK of the capture card. The interface of it is shown in Figure 2-12.



Figure 2-12 Interface of image acquisition software

The interface provides a video window showing the hand-dorsa vein images to be captured in real time. It also allows different settings of the capture card parameters, such as intensity, contrast and chroma. When auto capture button is pressed, 10 images of each hand for one individual will be captured by placing alternately the left hand and right hand under the image acquisition with an interval of 5 seconds between each. Single

capture is to obtain one image of hand-dorsa vein.

2.3. Database

A database of hand-dorsa vein images was created using the device implemented. The database contains 2,040 images from 102 individuals in which 52 are female and 50 are male. Ten images of each hand were captured for every individual with each individual placing alternately the left hand and right hand under the image acquisition device. Each image in the database has a size of 640×480 pixels and 256 grey levels. For each hand, the quality of captured images were assessed by eyes with error images removed and new images recaptured to ensure 10 good images for each hand. Some image samples acquired from the device are reproduced in Figure 2-13.

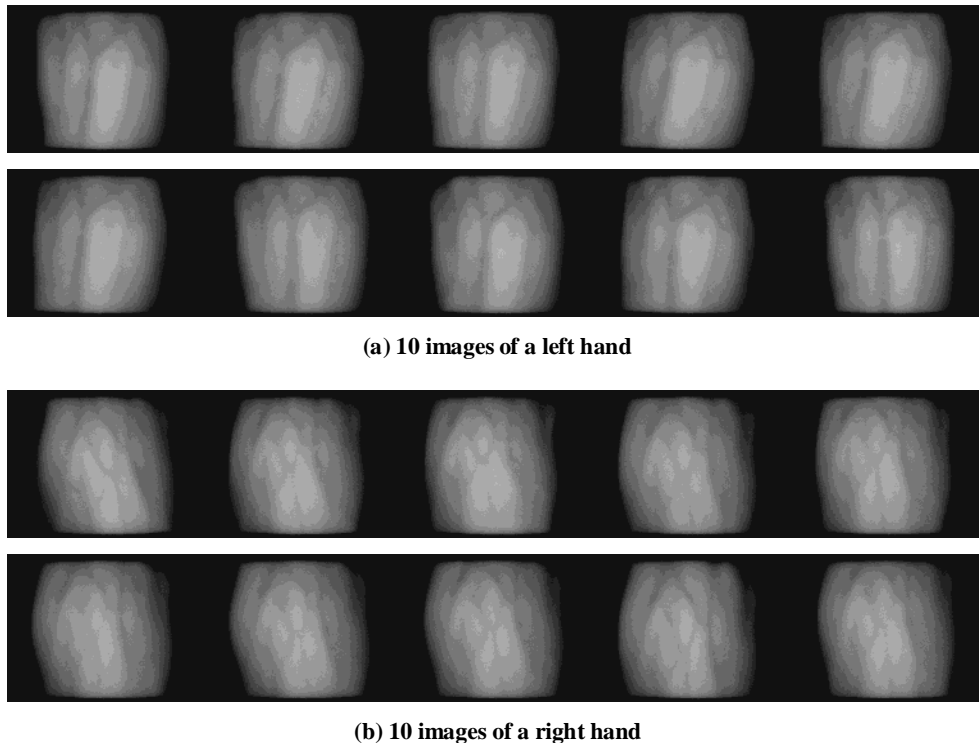


Figure 2-13 Example images obtained

The database has been used by researchers all over the world on vein pattern

Chapter 2. Image Acquisition Device and Database

recognition, and a comparison with some other databases is given in Table 2-5.

Table 2-5 Hand-dorsa vein image databases

Authors	Title	Total	Users	Hands	Male	Female	Age (Yr)
A. Kumar and K. Venkata Prathyusha [Kumar and Prathyusha, 2009]	Personal Authentication Using Hand Vein Triangulation and Knuckle Shape	300	100	100	81	19	14-55
C. L. Lin and K. C. Fan [Lin and Fan, 2004]	Biometric Verification Using Thermal Images of Palm-Dorsa Vein Patterns	960	32	32	-	-	-
L. Wang and G. Leedham [Wang and Leedham, 2005]	A thermal hand-vein pattern verification system	108	12	12	-	-	-
J.M. Cross and C.L. Smith [Cross and Smith, 1995]	Thermographic imaging of the subcutaneous vascular network of the back of the hand for biometric identification	100	20	20	-	-	-
T. Tanaka and N. Kubo [Tanaka and Kubo, 2004]	Biometric authentication by hand vein patterns	-	25	25	-	-	-
Y. Ding, D. Zhuang and K. Wang [Ding, Zhuang and Wang, 2005]	A Study of Hand Vein Recognition Method	240	48	48	-	-	-
K. Wang, Y. Zhang, Z. Yuan and D. Zhuang [Wang, Zhang, Yuan <i>et al</i> , 2006]	Hand Vein Recognition Based on Multi Supplemental Features of Multi-Classifer Fusion Decision	500	100	100	-	-	-
L.Wang and G. Leedham [Wang and Leedham, 2006]	Near- and Far-Infrared Imaging for Vein Pattern Biometrics	540(FIR)	30	30	-	-	-
		2700(NIR)	150	150	97	53	-
NCUT team	This work	2040	102	204	50	52	18-30

2.4. Summary and System Approach

In this chapter, the design and implementation of a low-cost hand vein image acquisition device are provided and two modules of the device, namely, illumination module and imaging module, are discussed in details. The analysis of the operational requirements for these two modules form the selection basis of suitable components.

A database of hand-dorsa vein images was created using the device implemented with capture software coded by Visual C++ 6.0. The database contains 2,040 images from 102 individuals in which 52 are female and 50 are male. The algorithms investigated in this work were tested on this database.

The author has worked as a member of the team in development of the NIR based hand-dorsa vein imaging system and a leader of the team in establishment of the database. For the former, the author was responsible for manufacturing of the prototype device shown in Figure 2-11 and development of the image acquisition software shown in Figure 2-12. For the latter, the author led the image capture campaign with a full spectrum of responsibilities, which included recruitment, management and organisation of work among team members, design of measurement protocol and procedure, supervision of image capture and quality of images captured.

With the hand-dorsa vein image acquisition device implemented and database established, Figure 2-14 illustrates the proposed approach to person identification by comparing the current input image from the hand-dorsa vein image acquisition device with all of the previously saved hand-dorsa images in the database based on the image features extracted. To minimise the recognition time, the required image pre-processing

Chapter 2. Image Acquisition Device and Database

and feature extraction operations for the training samples (hand-dorsa vein images of the registered people) are pre-executed off-line. With each training image represented and stored in computer memory as a feature vector, the identification task is implemented by using a classifier to perform one-to-many matching based on the distances between the training sample feature vectors and the input image feature vector produced by applying the same image pre-processing and feature extraction operations to the input hand-dorsa vein image. All the operations will be discussed in the following chapters.

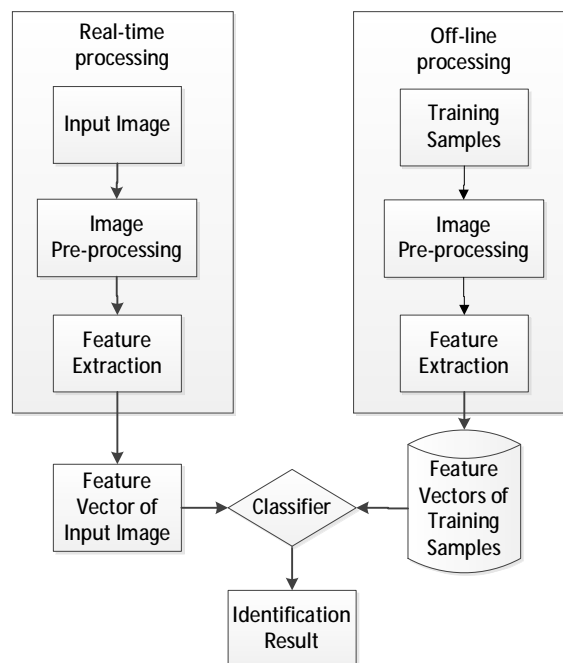


Figure 2-14 Proposed approach to person identification

Chapter 3. IMAGE ANALYSIS AND PRE-PROCESSING

3.1. Introduction

Image quality measurement is crucial for most image processing applications. Generally speaking, an image quality metric has three kinds of applications: First, it can be used to monitor image quality for quality control systems. Second, it can be employed to benchmark image processing systems and algorithms. Third, it can be embedded into an image processing system to optimise the algorithms and the parameter settings.

The International Standard Organisation (ISO) has defined a standard that specifies generic guidelines [ISO, 2011], where data conventions, capture requirement and format specification of vascular images have been given. However, the standard focuses on the data interchange without helping data evaluation for improving recognition results. In this work, geometrical distortion and grey-level variation are focused on.

Michael *et al.* implemented a quality controller accepting samples for which a Grey Level Co-Occurrence Matrix (GLCM) metric meets predefined thresholds [Michael, Connie, Hoe *et al.*, 2010]. Pascual *et al.* built a vein recognition system in which quality of the produced samples was measured through objective measurements such as contrast, variance and light distribution between vein and skin area [Pascual, Uriarte-Antonio, Sanchez-Reillo *et al.*, 2010]. Sanchez-Reillo *et al.* examined the impact of different light, temperature and humidity environments on the performance of a vein recognition system [Sanchez-Reillo, Fernandez-Saavedra, Liu-Jimenez *et al.*, 2007]. Raghavendra *et al.*

Chapter 3. Image Analysis and Pre-processing

[Raghavendra, Imran, Rao *et al*, 2010] and Lee *et al*. [Lee, Lee and Park, 2009] artificially degraded the sample images' quality to prove a decrease in biometric recognition performance. Yang *et al*. [Yang, Shi and Yang, 2010] and Wu *et al*. [X. Wu, Tang and Wang, 2010] investigated different hand areas and found differences in the performance.

Vein images obtained cannot be used for identification directly. It is necessary to do some pre-processing on them for the following reasons:

- 1) Geometrical variations, such as shift, rotation and scale caused by different hand poses.
- 2) Images containing background in addition to the back of the hand require region of interest (ROI) to be extracted.
- 3) Non-uniform and non-constant illumination resulting in different image qualities.
- 4) Inherent noise in the vein images.

The diagram of the pre-processing stages implemented is shown in Figure 3-1 and each stage is described in detail in the following sub-sections.

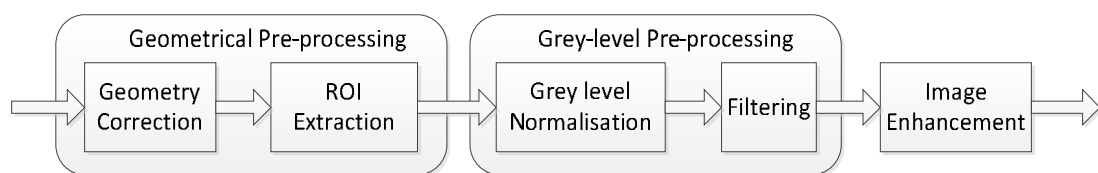


Figure 3-1 Pre-processing diagram

In this research, image quality assessment was investigated for improving pre-processing and the final results.

3.2. Geometrical Pre-processing

3.2.1. Analysis of Image Consistency

The best way to assess the quality of an image is perhaps to look at it because human visual system is the ultimate receiver in most image processing environments. The subjective quality measurement, Mean Opinion Score (MOS), which is the mean value of all the scores given by viewers and ranged from 1 (worst) to 5 (best), has been used for many years [ITU, 2003].

However, the MOS method is too inconvenient, slow and expensive for practical usage. The goal of objective image quality assessment research is to supply quality metrics that can produce perceived image quality automatically. Mean Squared Error (MSE) [Lehmann and Casella, 1998] and Peak Signal-to-Noise Ratio (PSNR) [Huynh-Thu and Ghanbari, 2008] are the most widely used objective image quality/distortion metrics. Here, they are used to evaluate the consistency of database images. The m th image of the n th hand that has C pixels can be represented by:

$$G_{n,m} = \{g_{n,m,1} \quad g_{n,m,2} \quad \mathbf{L} \quad g_{n,m,C}\} \quad (n=1,2,\mathbf{L},204; m=1,2,\mathbf{L},10) \quad (3-1)$$

Reference image of the n th hand $R_n = \{r_{n,1} \quad r_{n,2} \quad \mathbf{L} \quad r_{n,C}\}$ can be obtained based on the average by:

$$R_n = \frac{1}{10} \sum_{m=1}^{10} G_{n,m} \quad (3-2)$$

MSE and PSNR values can be calculated with respect to the reference image by:

$$MSE(G_{n,m}, R_n) = \frac{1}{C} \sum_{k=1}^C (g_{n,m,k} - r_{n,k})^2 \quad (3-3)$$

Chapter 3. Image Analysis and Pre-processing

$$PSNR(G_{n,m}, R_n) = 10 \log_{10} \left[\frac{B^2}{MSE(G_{n,m}, R_n)} \right] \quad (3-4)$$

where C is the number of pixels and B is maximum possible pixel value ($2^8 - 1 = 255$ for 8-bit images).

In Figure 3-2, two example reference images R_{80} and R_{51} are shown in (a) and (e), two images most similar to the corresponding reference images are shown in (b) and (f), and two images least similar to the corresponding reference images are shown in (c) and (g). Moreover, the PSNR values of $G_{80,1}$ and $G_{51,6}$ are also the minimum and maximum of all the images in the database. While the minimum PSNR value corresponds to the case of highest geometrical distortion due to inconsistent hand postures, the maximum PSNR value corresponds to the case of consistent hand postures with least geometrical distortion.

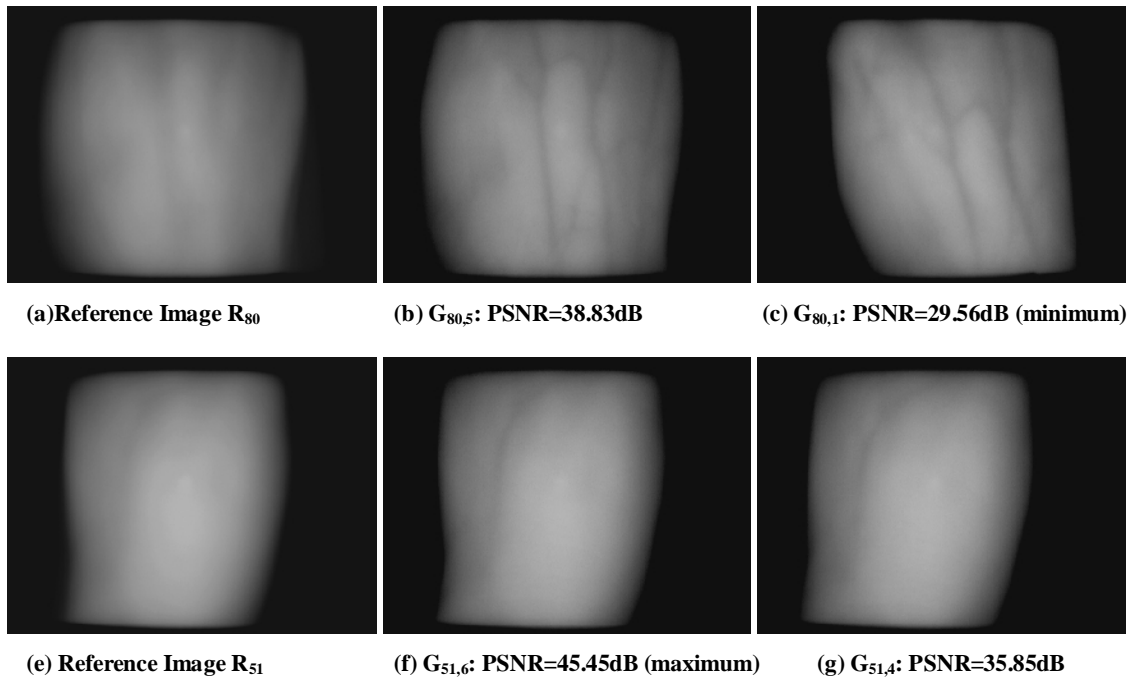


Figure 3-2 PSNR results

Chapter 3. Image Analysis and Pre-processing

A test was performed to evaluate the impact of the image consistency on the recognition rate. By using different PSNR values as a threshold to remove those images which are significantly dissimilar to their corresponding reference images, Table 3-1 tabulates the recognition results obtained by applying the nearest neighbour classification method to the features described using the partition local binary pattern (discussed in Chapter 5). From Table 3-1, the recognition is seen to increase as more and more images with the worst PSNR values are removed, and the best recognition rate is seen to occur when 73 images with the worst PSNR values are removed, which is almost 1% better than that without removing any images.

Table 3-1 Results after removing poor quality images

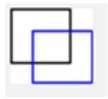
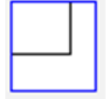
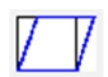
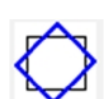
	Number of images removed	Number of images remaining	Recognition rate (%)
All	0	2040	98.33
PSNR<30 dB	1	2039	98.43
PSNR<31 dB	17	2023	98.81
PSNR<32 dB	73	1967	99.03
PSNR<33 dB	212	1828	98.91

3.2.2. Geometrical Correction

Image geometrical correction could be put into plane correction and space correction depending on the problems of images. The former is to correct 2D variations based on affine transformation, which include shift, scaling, shearing, rotation etc. The latter is to do projection correction in 3D space. Examples and correction methods of affine image transformation are listed in Table 3-2.

Chapter 3. Image Analysis and Pre-processing

Table 3-2 Examples and correction methods of affine transformation

Types	Examples	Transformation matrix	Parameters
Shift		$\begin{bmatrix} 1 & 0 & 0 \\ 0 & 1 & 0 \\ t_x & t_y & 1 \end{bmatrix}$	t_x : shift in x axis t_y : shift in y axis
Scaling		$\begin{bmatrix} s_x & 0 & 0 \\ 0 & s_y & 0 \\ 0 & 0 & 1 \end{bmatrix}$	s_x : scaling of x axis s_y : scaling of y axis
Shearing		$\begin{bmatrix} 1 & sh_y & 0 \\ sh_x & 1 & 0 \\ 0 & 0 & 1 \end{bmatrix}$	sh_x : shearing factor of x sh_y : shearing factor of y
Rotation		$\begin{bmatrix} \cos(q) & \sin(q) & 0 \\ -\sin(q) & \cos(q) & 0 \\ 0 & 0 & 1 \end{bmatrix}$	q : rotation angle

Although the image acquisition device has a handle to position the hand, some distortions cannot be avoided. Incorrect handle grasping may lead to rotation, which can be corrected based on hand boundary detection method described in the paper [Cui, Wang and Li, 2010]. If handle is grasped correctly, only image shearing effects are observed, which are caused by unconstrained wrist. As images in the database are captured under correct handle grasping condition, geometrical distortion due to image shearing effects needs to be corrected in order to achieve good recognition results.

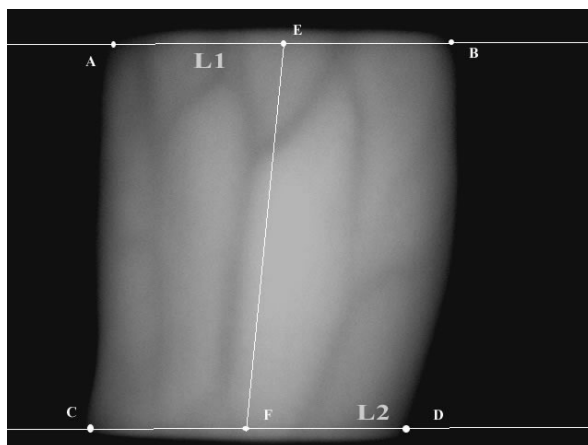
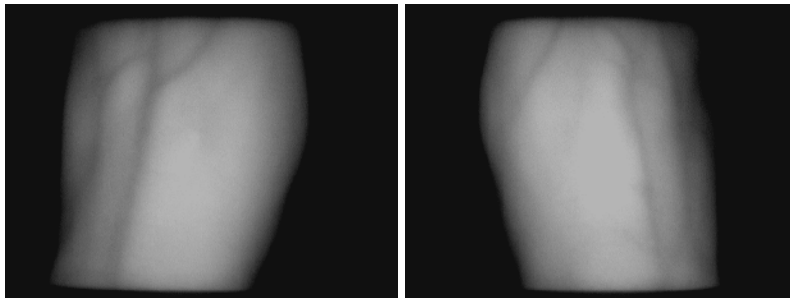
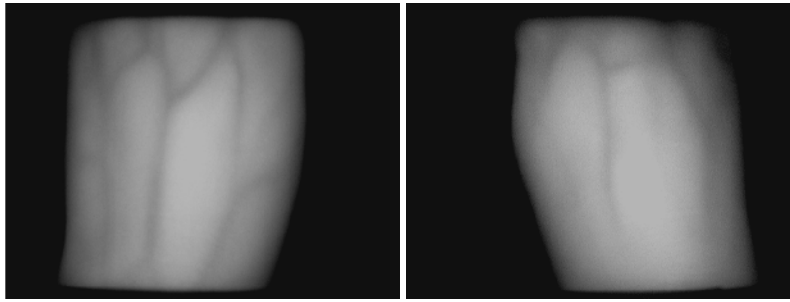


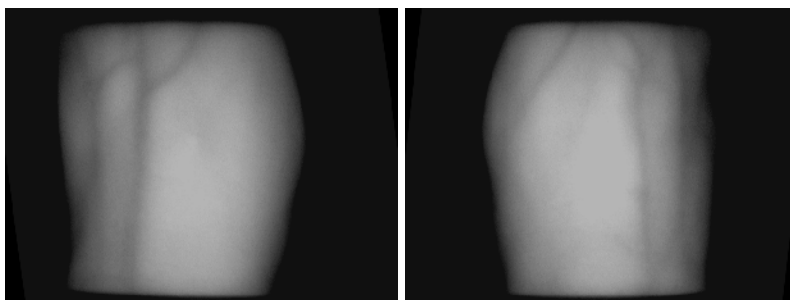
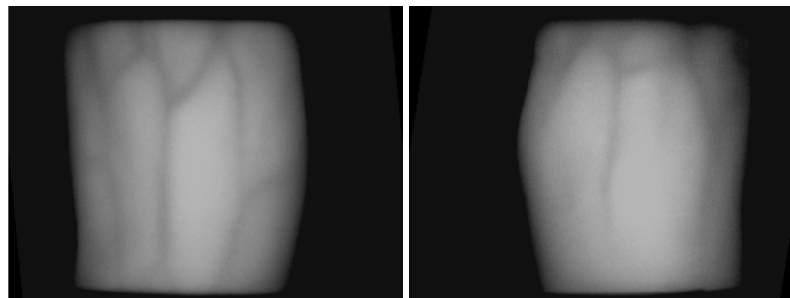
Figure 3-3 Shearing correction

As shown in Figure 3-3, to correct shearing, boundary points of hands (A, B, C, D) firstly are found along the two horizontal lines which are positioned at 50 pixels from the top and bottom of the acquired image denoted by L1 and L2. Then the middle points of AB and CD are calculated as E and F, and the shearing factor is determined based on the slope of line EF. Some example results are shown in Figure 3-4.

Chapter 3. Image Analysis and Pre-processing



(a) Before correction



(b) After correction

Figure 3-4 Results of shearing correction

Chapter 3. Image Analysis and Pre-processing

After geometrical correction, the number of images with smaller PSNR values has been reduced and this is shown in Table 3-3, which indicates that the image consistency is improved after this process.

Table 3-3 Poor quality images before and after geometrical correction

	Number of images before correction	Number of images after correction
PSNR<30 dB	1	1
PSNR<31 dB	17	16
PSNR<32 dB	73	67
PSNR<33 dB	212	183

3.2.3. Region of Interest Extraction

Extraction of ROI (region of interest) containing hand-dorsa vein patterns has been discussed previously [Kumar and Prathyusha, 2009]. In this work, the centroid is used as the centre to extract the ROI. The centroid (x_0, y_0) of a vein image denoted by $G(x, y)$ can be calculated as

$$x_0 = \frac{\sum_{i,j} i \times g(i, j)}{\sum_{i,j} g(i, j)}; \quad y_0 = \frac{\sum_{i,j} j \times g(i, j)}{\sum_{i,j} g(i, j)} \quad (3-5)$$

where $g(i, j)$ denotes the grey value of the pixel (i, j) .

A square region of size $R \times R$ pixels with the centroid as the centre is extracted as the vein image to be processed. To confirm the size, ROI with R ranging from 300 to 420 pixels are extracted as shown in Figure 3-5.

Chapter 3. Image Analysis and Pre-processing

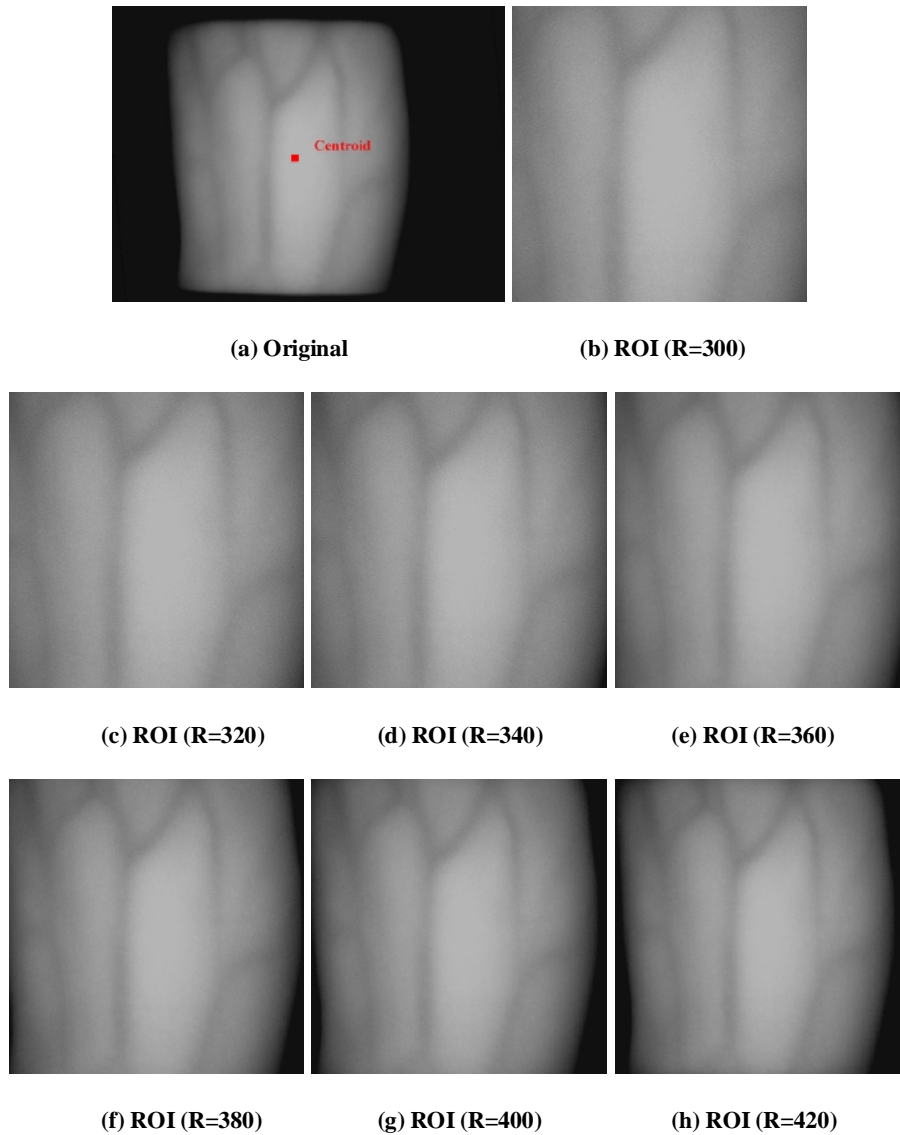


Figure 3-5 Result of ROI extraction

From Figure 3-5, when $R=380$ pixels, almost all the hand-dorsa vein information is included. The redundant background information with little hand information is introduced when $R=400$ pixels and $R=420$ pixels. More results are shown in Appendix A. To further confirm the size, a test was performed to evaluate the impact of the ROI size on the recognition rate. By using different ROI sizes, Table 3-4 tabulates the recognition results obtained by applying the nearest neighbour classification method to the features

Chapter 3. Image Analysis and Pre-processing

described using the partition local binary pattern (discussed in Chapter 5). From Table 3-4, the recognition is seen to increase as ROI size increases, and reaches the highest recognition rate of 98.33% when the ROI size equals 380 pixels and above. Therefore, 380×380 pixels are the ROI size adopted in this work.

Table 3-4 Comparison of results of different ROI sizes

ROI size (pixels)	300×300	320×320	340×340	360×360	380×380	400×400	420×420
Recognition rate (%)	97.55	97.65	97.84	98.14	98.33	98.33	98.33

After ROI extraction, the number of images with smaller PSNR values has been further reduced and this is shown in Table 3-5, which indicates a further improvement of the image consistency after this process.

Table 3-5 Poor quality images before and after ROI extraction

	Number of images before ROI extraction	Number of images after ROI extraction
PSNR<30 dB	1	0
PSNR<31 dB	16	4
PSNR<32 dB	67	15
PSNR<33 dB	183	48

3.3. Grey-level Pre-processing

3.3.1. Grey-level Normalisation

Since the illumination intensity may vary at different times, the grey scale distributions of vein images can be different. To reduce the differences, thereby simplifying the segmentation process, a method of grey-level normalisation based on the following equation is adopted:

Chapter 3. Image Analysis and Pre-processing

$$g = 255 \times \frac{f - f_{\min}}{f_{\max} - f_{\min}} \quad (3-6)$$

where f is the grey level value of the original image with f_{\min} and f_{\max} denoting its minimum and maximum grey level values; and g is the grey level value after normalisation which will occupy the maximum grey level range from 0 to 255. The contrast of image can be stretched by this process. An example result is shown in Figure 3-6.

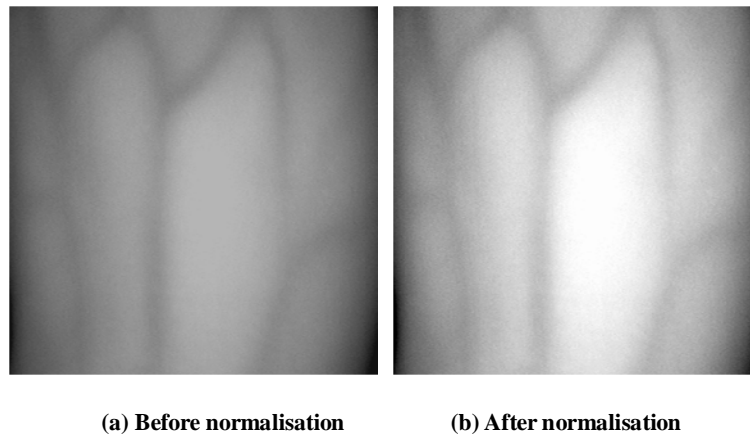


Figure 3-6 Result of grey level normalisation

3.3.2. Noise Measurement

There are various noise sources in a CCD camera, such as the dark current that flows through the CCD chip when no photons are entering the camera, dust inside the camera, and overheated or faulty CCD elements. In addition, the image may contain some background objects in the capture area. As hand-dorsa veins mainly locate along vertical direction, grey value variations of each row contain more vein information. Using the grey level profile along the middle row of a hand-dorsa vein image as a sample, the noise effect is illustrated in Figure 3-7. Instead of a smooth grey level profile, with low and high grey level values indicating vein and non-vein areas, there are significant local

Chapter 3. Image Analysis and Pre-processing

fluctuations throughout due to noise.

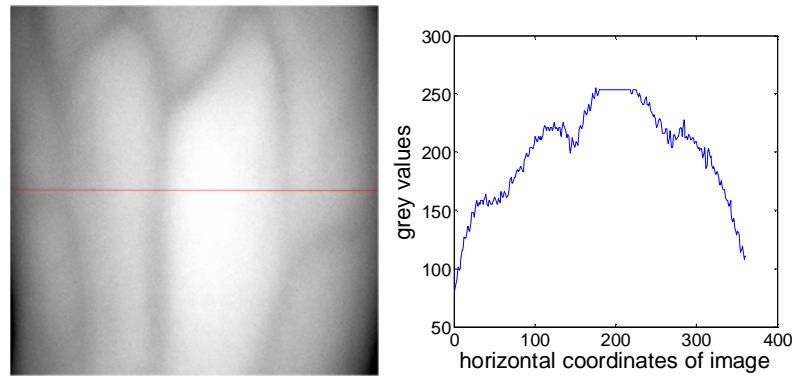


Figure 3-7 Grey level profile of middle row

In order to measure the extent of local fluctuations due to noise, a metric based on total variation (TV) is introduced with a bigger TV value implying more noise [Zhao, Wang and Wang, 2008]. For a digital image denoted by $G(x, y)$, TV is calculated as:

$$TV(G) = \sum_i \sum_j \left[\begin{array}{l} (g(i, j) - g(i-1, j))^2 \\ + (g(i, j) - g(i+1, j))^2 \\ + (g(i, j) - g(i, j-1))^2 \\ + (g(i, j) - g(i, j+1))^2 \end{array} \right]^{\frac{1}{2}} \quad (3-7)$$

where $g(i, j)$ denotes the grey value of the pixel (i, j) .

$g(i-1, j-1)$	$g(i, j-1)$	$g(i+1, j-1)$
$g(i-1, j)$	$g(i, j)$	$g(i+1, j)$
$g(i-1, j+1)$	$g(i, j+1)$	$g(i+1, j+1)$

Figure 3-8 A diagram of TV value pixels

3.3.3. Noise Reduction by Filtering

Some commonly used filters will be investigated in this section.

A. Match filter [Chitode, 2008, North, 1963]

Match filter is designed according to the maximum signal-to-noise ratio (SNR) criterion.

Assuming that a real signal $x(t)$ is polluted by additive noise $n(t)$, an observed signal $y(t)$ can be given:

$$y(t) = x(t) + n(t) \quad (3-8)$$

To restore the real signal from this signal, a match filter can be obtained based on the maximum SNR principle:

$$H_{opt}(\omega) = \frac{X^*(\omega)}{P_n(\omega)} e^{-j\omega T_0} \quad (3-9)$$

where $X^*(\omega)$ is the conjugate frequency spectrum of $x(t)$, $P_n(\omega)$ is the power spectrum of noise, T_0 is a constant. If the noise is white noise, $H_{opt}(\omega)$ and its time domain representation $h_{opt}(t)$ can be simplified as:

$$H_{opt}(\omega) = X^*(\omega) e^{-j\omega T_0} \quad (3-10)$$

$$h_{opt}(t) = x(T_0 - t) \quad (3-11)$$

For the NIR images, dark current noise could be approximated as white noise approximately. So that the match filter will be a mirror signal of the original one. As mostly hand-dorsa veins are longitudinal and of width about 10 to 15 pixels, a 1 dimension match filter applied to rows is designed as shown in Figure 3-9.

Chapter 3. Image Analysis and Pre-processing

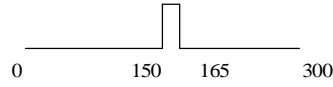


Figure 3-9 Time domain representation of match filter

Each line of a hand-dorsa vein image could be seen as a real signal polluted with noise. All the lines of image are processed with a match filter designed above to enhance vein information and reduce noise.

B. Wiener filter [Vaseghi, 2008, Wiener, 1949]

Wiener filter is designed based on the minimum mean-square error principle. For an image signal denoted by $F(x, y)$, a result $G(x, y)$ after Wiener filtering can be obtained by:

$$g(i, j) = m + \frac{S^2 - v^2}{S^2} (f(i, j) - m) \quad (3-12)$$

where $g(i, j)$, $f(i, j)$ are the pixel values of the original image and filtered image, m and S are the mean and standard deviation of $L \times L$ neighbourhood, and v is the standard deviation of the noise signal. In this work, as the noise is not given, v will be set as the average of all the local estimated standard deviations.

C. Mean filter [Davies, 2004]

This method is to calculate the mean value of $M \times N$ neighbourhoods as the centre pixel value. For a digital image denoted by $F(x, y)$, the filtered image $G(x, y)$ can be processed by:

$$g(i, j) = \frac{1}{MN} \sum_{(i,j) \in S} f(i, j) \quad (3-13)$$

where $g(i, j)$, $f(i, j)$ are the pixel values of the original image and after filtering image.

Chapter 3. Image Analysis and Pre-processing

S is the $M \times N$ neighbourhoods.

D. Median filter [Arce, 2005]

This method is to calculate the median value of $M \times N$ neighbourhoods as the centre pixel value. For a digital image denoted by $F(x, y)$, the filtered image $G(x, y)$ can be processed by:

$$g(i, j) = W\left(\frac{MN}{2}\right) \quad (3-14)$$

$$W = \underset{(i,j) \in S}{\text{Sort}}[f(i, j)] \quad (3-15)$$

where $g(i, j)$, $f(i, j)$ are the pixel values of the original image and filtered image. S is the $M \times N$ neighbourhood. W is a vector contains all the pixel values belonging to S after being sorted.

E. Gaussian filter [Haddad, 1991]

A Gaussian filter modifies the input image by using a Gaussian function, which can be expressed as:

$$g(x, y) = \frac{1}{2ps^2} e^{-\frac{x^2+y^2}{2s^2}} \quad (3-16)$$

where s denotes the standard deviation of the Gaussian distribution. A Gaussian mask template can be given by:

$$h(i, j) = \frac{h_g(i, j)}{\sum_i \sum_j h_g(i, j)} \quad (3-17)$$

$$h_g(i, j) = e^{-\frac{i^2+j^2}{2s^2}} \quad (3-18)$$

Different Gaussian kernel functions can be given by changing the template size $L \times L$

and the standard deviation S .

F. Improved Gaussian filter

Although Gaussian filter can reduce random noise effectively, boundary information is polluted. To solve this problem, weights are added to the mask templates [Liu, Shen and Zheng, 2000]. The weights are given by:

$$\begin{aligned}
 h_w &= W_L \times W_c' \\
 W_L &= e^{-(i^2+j^2)/L} \\
 W_c' &= e^{W_c^2/D} \\
 W_c &= f(i, j) - f(i + \Delta i, j + \Delta j)
 \end{aligned} \tag{3-19}$$

where L is the size of Gaussian mask template. D is determined by experiments.

3.3.4. Experimental Results of Filtering

For Wiener filter, mean filter and median filter, the neighbourhood window size is set to 15×15 , and for Gaussian filter and improved Gaussian filter, the Gaussian mask template size is set to 15×15 pixels, as the width of hand-dorsa vein is about 10 to 15 pixels. If L were too small, noise would not be reduced, while if L were too big vein information would be lost. For Gaussian filter, σ is set to 0.5 based on the TV values obtained from images processed by Gaussian filtering with σ ranging from 0.1 to 1. For improved Gaussian filter, D is set to 0.1 based on the TV values obtained from images processed by improved Gaussian filtering with D ranging from 0.1 to 1. To compare the effectiveness of filters discussed above, the images before and after filtering are shown in Figure 3-10.

Chapter 3. Image Analysis and Pre-processing

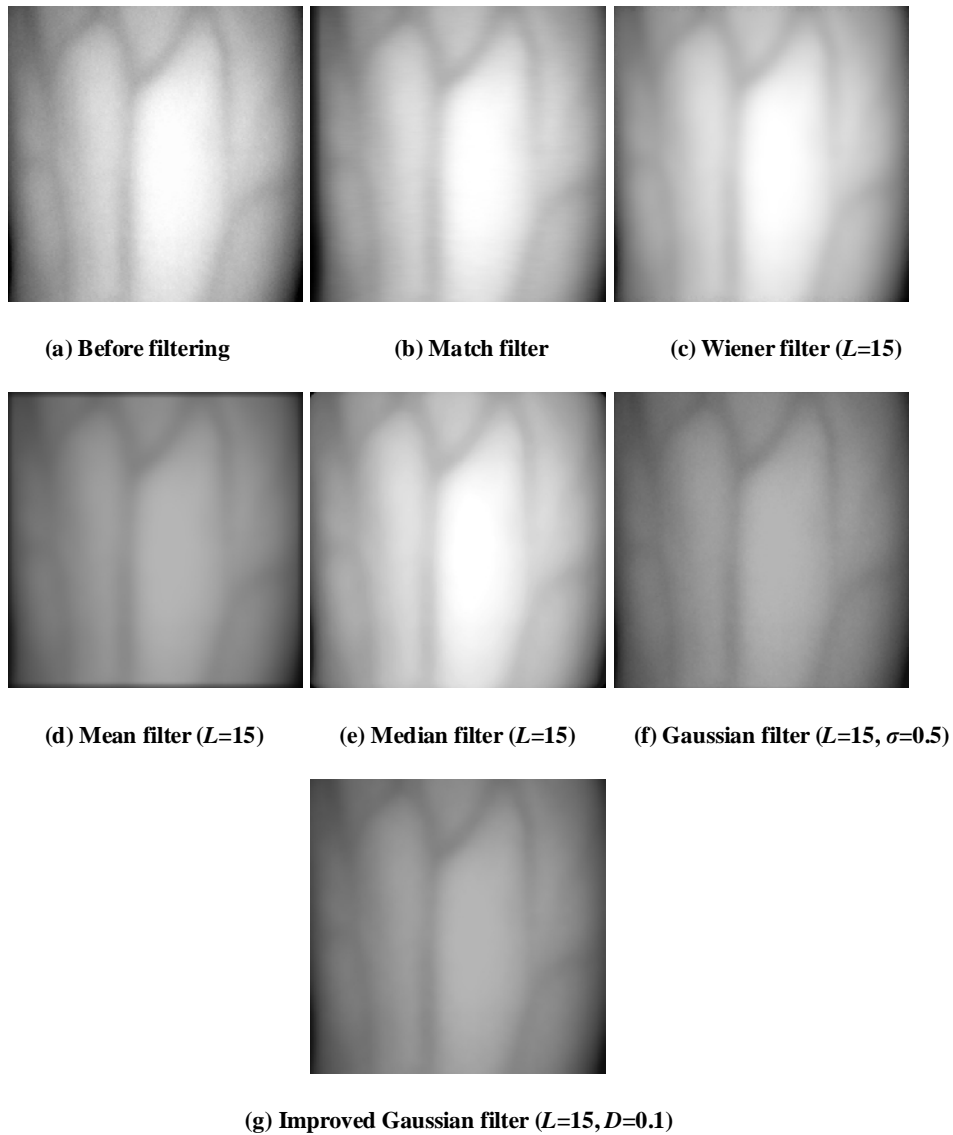


Figure 3-10 Results of filtering

To illustrate the improvement made on the hand-dorsa vein images shown in Figure 3-10 after noise reduction by filtering, the grey value profile of the middle rows are shown in Figure 3-11. It can be seen that all the filtered images have lower local fluctuations compared with that before filtering and the performance of Gaussian filter is seen to be the worst with its output being less smooth than others.

Chapter 3. Image Analysis and Pre-processing

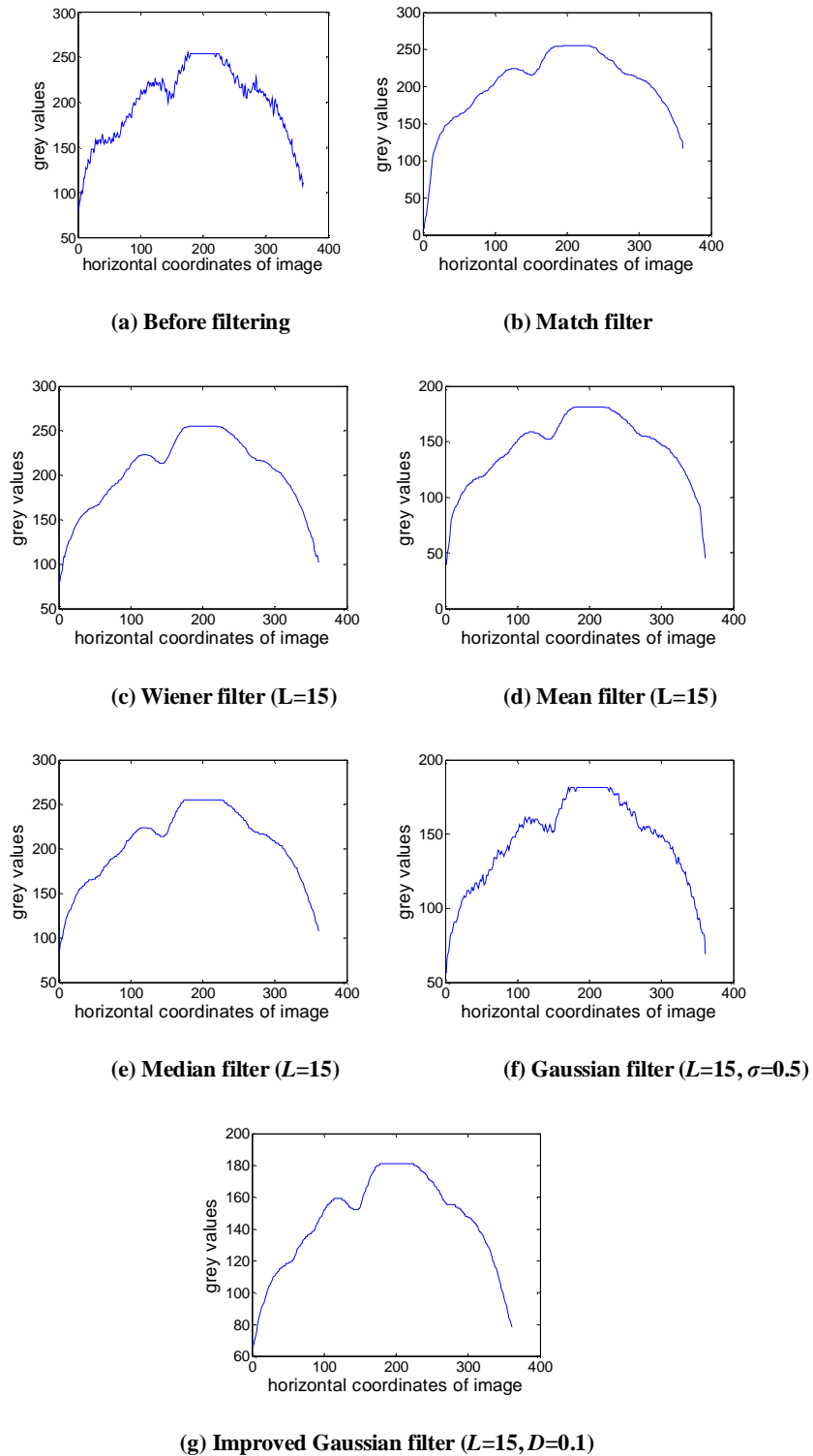


Figure 3-11 Grey level profiles of middle rows from original and filtered images

Chapter 3. Image Analysis and Pre-processing

To further analyse the results, TV values of the original and filtered images are calculated by equation (3-7) and listed in Table 3-6. From the results, improved Gaussian filter [Liu, Wu, Pan *et al*, 2007] is seen to perform better than others with lowest TV value.

Table 3-6 TV values of original and filtered images

	Original	Match filter	Wiener filter	Mean Filter	Median Filter	Gaussian filter	Improved Gaussian filter
TV	3869.5	1442.2	1020.1	1192.5	988.7	2649.2	872.5

3.4. Image Enhancement

Vein images should be enhanced to maximise contrast and structure visibility before segmentation. Histogram equalisation (HE) is a common method for it.

This method usually increases the global contrast of an image, especially when the usable data of the image is represented by close contrast values. Through this adjustment, the intensities can be better distributed in the histogram. This allows for areas of lower local contrast to gain a higher contrast. Histogram equalisation accomplishes this by effectively spreading out the most frequent intensity values.

The transformation, $T(a)$, to enable the grey level values in the output image to be uniformly distributed in [0,1] is given by

$$s = T(a) = \sum_{i=0}^a p_i(z) \quad (i = 0, 1, \dots, 255) \quad (3-20)$$

where s is the grey level value of the output image, a is the grey level value of the input image, and $p_i(z)$ is the probability density function (PDF) of the input image. All the grey levels would appear in the output image, and the probability density is

Chapter 3. Image Analysis and Pre-processing

$$p_s(s) = \begin{cases} 1, & 0 \leq s \leq 1 \\ 0, & \text{others} \end{cases} \quad (3-21)$$

The method is useful for images with backgrounds and foregrounds that are both bright or both dark. A disadvantage of the method is that it is indiscriminate. It may increase the contrast of background noise, while decreasing the usable signal. Hence an improved HE algorithm called Contrast Limited Adaptive Histogram Equalisation (CLAHE) is adopted to provide the required image enhancement [Pizer, Amburn, Austin *et al*, 1987].

The CLAHE algorithm partitions the images into contextual regions ($L \times L$) and applies histogram equalisation to each one. This evens out the distribution of used grey level values and thus makes hidden features in the image more visible. The full grey spectrum is used to express the image. It could be presented as:

$$h_L(a) = a h_w(a) + (1-a) h_G(a) \quad (3-22)$$

where $h_L(a)$ is the normalised histogram adopted for sub-region;

$h_w(a)$ is the normalised histogram inside window;

$h_G(a)$ is the normalised histogram outside window;

$0 \leq a \leq 1$ is a local weight factor.

The results of HE and CLAHE are shown in Figure 3-12.

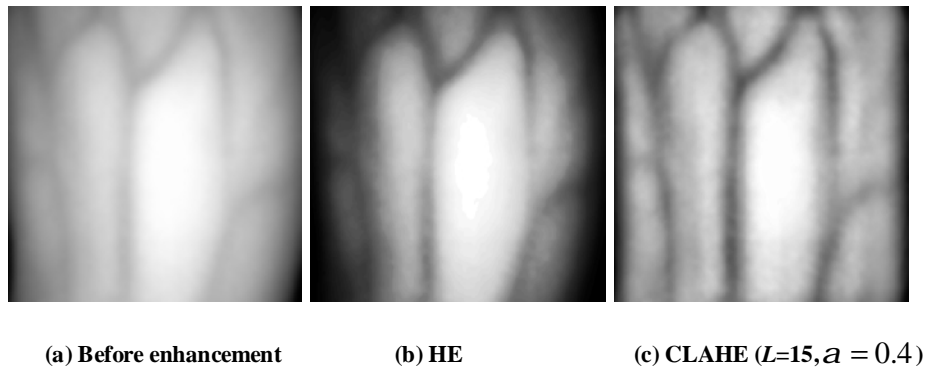


Figure 3-12 Results of HE and CLAHE

From Figure 3-12, sharp edges are seen to be maintained after CLAHE, whereas some vein information is seen to be lost after HE.

3.5. Summary

In this chapter, database image consistency is assessed based on the grey level deviation of each hand-dorsa vein image with respect to its group average. Using a measurement metric derived from PSNR, the deviation is shown to vary between 29.56 dB to 45.45 dB for the database, with low PSNR values indicating high deviations. Introduction of image shearing correction and ROI extraction has shown to decrease the number of low PSNR images significantly. Furthermore, the optimum size of ROI is shown to be 380×380 pixels.

Image noise in terms of local fluctuations on the grey level profile has also been investigated with a quantitative noise assessment introduced based on TV values. The performance of some commonly used filters have been investigated for noise reduction and improved Gaussian filter has been found to have the best performance.

Other image pre-processing techniques investigated in this chapter include grey level normalisation and image enhancement based on CLAHE. While the former is performed

Chapter 3. Image Analysis and Pre-processing

after ROI extraction and before noise reduction, the latter is performed at the last stage of the pre-processing.

Chapter 4. SEGMENTATION OF VEIN IMAGES

4.1. Introduction

In image processing, segmentation refers to the process of partitioning a digital image into multiple segments based on image content. For vein images, it means partitioning image into vein part and non-vein part. Considering the processing time, almost all the researchers adopt threshold-based algorithms [Ding, Zhuang and Wang, 2005, Otsu, 1979, Zhao, Wang and Wang, 2008] to segment vein images with some using boundary methods [Wang, Guo, Zhuang *et al*, 2006].

Some papers had proved that good segmentation effect cannot be achieved by single threshold segmentation methods. Such methods include fixed threshold, total mean and total Otsu as well as multi-thresholds segmentation methods which include local mean and local Otsu [Otsu, 1979]. Ding *et al.* proposed a threshold image method [Ding, Zhuang and Wang, 2005]. Wang *et al.* implemented the Niblack method to vein image and compared its effect with the boundary-characteristic-based method, from which a conclusion can be made that the gradient-based method offers a better performance for vein images [Wang, Guo, Zhuang *et al*, 2006]. In the paper of Zhao, a small improvement was made to the Niblack method and gained better results [Zhao, Wang and Wang, 2008]. Wang *et al.* proposed a segmentation method based on gradient enhancement [Wang and Wang, 2009].

In the following sections, some image segmentation methods, including threshold methods, boundary methods and a fusion of both, are investigated to compare their

effects. After segmentation, images are post-processed with morphological filtering and thinning.

4.2. Segmentation Algorithms

4.2.1. Threshold Methods

The simplest method of image segmentation is called the threshold method. This method is based on a clip-level (or a threshold value) to produce a binary image from a grey-scale image.

The key of this method is to select the threshold value (or values when multiple-levels are selected). Several popular methods are used in vein image processing including fixed threshold, Otsu's method (maximum variance) [Otsu, 1979], Threshold Image [Ding, Zhuang and Wang, 2005] and Niblack [Niblack, 1986]. Although different threshold values are selected in these methods, all of them are based on

$$g(x, y) = \begin{cases} 255, & f(x, y) > T \\ 0, & f(x, y) \leq T \end{cases} \quad (4-1)$$

where g denotes the output image, f denotes the input image, and T is the threshold value. Some popular threshold algorithms are presented in the following.

A. Maximum variance (Otsu's method)

This method is named after Nobuyuki Otsu [Otsu, 1979]. The algorithm assumes that the image to be thresholded contains two classes of pixels (e.g. foreground and background) and calculates the optimum threshold separating those two classes so that their combined spread (intra-class variance) is minimal.

Let the pixels of a given image be represented in L grey levels. The number of

Chapter 4. Segmentation of Vein Image

pixels at level i is denoted by n_i and the total number of pixels is given by:

$$N = \sum_{i=1}^L n_i \quad (4-2)$$

In order to simplify the discussion, the grey-level histogram is normalised and regarded as a probability distribution:

$$p_i = \frac{n_i}{N}, \quad p_i \geq 0, \quad \sum_{i=1}^L p_i = 1 \quad (4-3)$$

If the pixels are divided into two classes denoted by a and b by a threshold at level t , then the probabilities of class occurrence and the class mean levels, respectively, are given by:

$$\begin{aligned} w(a) &= \sum_{i=1}^t p_i = w(t) \\ w(b) &= \sum_{i=t+1}^L p_i = 1 - w(t) \end{aligned} \quad (4-4)$$

$$\begin{aligned} m(a) &= \sum_{i=1}^t \frac{i \cdot p_i}{w(a)} = \frac{m(t)}{w(t)} \\ m(b) &= \sum_{i=t+1}^L \frac{i \cdot p_i}{w(b)} = \frac{m - m(t)}{1 - w(t)} \end{aligned} \quad (4-5)$$

where, $w(t)$ and $m(t)$ are the zeroth- and the first-order cumulative moments of the histogram, respectively, and m is the total mean level of the original image.

The class variances are given by:

$$\begin{aligned} s(a)^2 &= \sum_{i=1}^t \frac{[i - m(a)]^2 \cdot p_i}{w(a)} \\ s(b)^2 &= \sum_{i=t+1}^L \frac{[i - m(b)]^2 \cdot p_i}{w(b)} \end{aligned} \quad (4-6)$$

Chapter 4. Segmentation of Vein Image

In order to evaluate the "goodness" of the threshold (at level t), the following discriminant criterion measures (or measures of class separability) are used in the discriminant analysis:

$$l = \frac{S_B^2}{S_W^2}, \quad h = \frac{S_B^2}{S_T^2} = \frac{l}{l+1} \quad (4-7)$$

where,

$$S_W^2 = w_0 S_0^2 + w_1 S_1^2 \quad (4-8)$$

$$S_B^2 = w_0 (m_0 - m_T)^2 + w_1 (m_1 - m_T)^2 = w_0 w_1 (m_1 - m_0)^2 \quad (4-9)$$

$$S_T^2 = \sum_{i=1}^L (i - m_i)^2 p_i \quad (4-10)$$

are the within-class variance, the between-class variance, and the total variance of levels, respectively. Since h is the simplest measure with respect to t , it is used as the criterion measure to evaluate the separability of the threshold at level t . The threshold is considered as optimum when h is maximised.

A sample of Otsu results is shown in Figure 4-1, where (a) shows the enhanced image before segmentation, (b) shows the image histogram with the threshold value of 159 computed by Otsu method, and (c) shows the binary image after thresholding.

Chapter 4. Segmentation of Vein Image

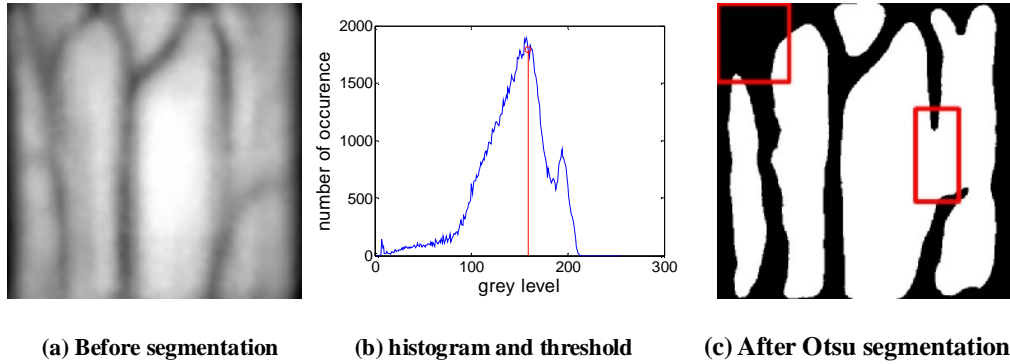


Figure 4-1 Result of Otsu's method

Due to the use of a fixed threshold, it often results in under segmentation in some parts of the image and over segmentation in other parts of the image. This is clearly seen in Figure 4-1(c), where under segmentation occurs at the top left of the segmented image with the background in that area shown as a part of the vein feature due to the threshold value being too high for that part of the image, and over segmentation occurs in the middle right part of the image with missing vein due to the threshold value being too low for that part of the image.

B. Threshold image

This method uses a threshold image $T(x, y)$ with the size same as the original image $f(x, y)$, and segments the original image by using the threshold image [Ding, Zhuang and Wang, 2005]. Given $L \times L$ neighbouring points around every pixel (x, y) , the threshold image $T(x, y)$ is given by the mean of grey level values in $L \times L$ neighbourhood around (x, y) . The segmentation follows the equation given by

$$g(x, y) = \begin{cases} 255 & f(x, y) > T(x, y) \\ 0 & f(x, y) \leq T(x, y) \end{cases} \quad (4-11)$$

As the vein is about 10 to 15 pixels wide, L is set to 15 in this work. If L were too

Chapter 4. Segmentation of Vein Image

small, more background areas would be considered as vein area, while if L were too big vein branches would be missed. The threshold image and segmentation results are shown in Figure 4-2.

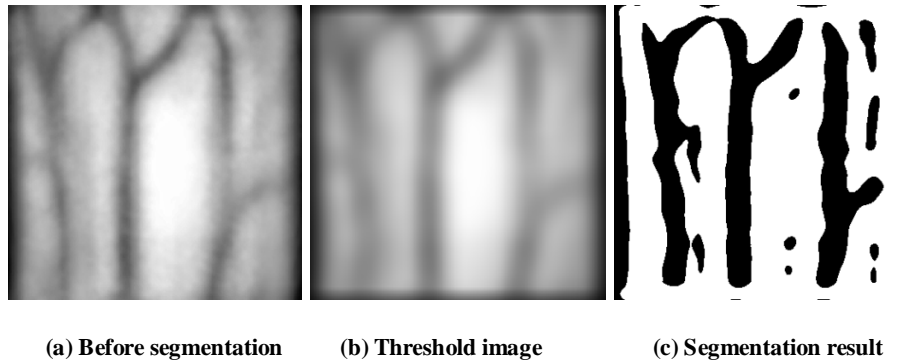


Figure 4-2 Result of threshold image method

This method is quick but the threshold is the local mean, which cannot divide the vein image and dark background effectively. Moreover, the image borders can cause significant segmentation errors.

C. Niblack and improved Niblack

Niblack's method is simple and effective as a local dynamic threshold segmentation method [Niblack, 1986]. It calculates the mean, $m(x, y)$, and variance, $s(x, y)$, of every pixel in a neighbourhood of $L \times L$ pixels to determine the threshold image $T(x, y)$ using equation (4-12).

$$T(x, y) = m(x, y) + k \times s(x, y) \quad (4-12)$$

where k is the correction coefficient determined by experiments. In the paper of Zhao [Zhao, Wang and Wang, 2008], a change was made in the calculation of variance $s(x, y)$ by using:

$$s(x, y) = \sqrt{\frac{1}{r^2} \sum_{i=x-L/2}^{x+L/2} \sum_{j=y-L/2}^{y+L/2} (f(i, j) - m(x, y))^2} \quad (4-13)$$

This method considers the variation of illumination in the vein image and could estimate a better threshold. However, this method is not good enough for the vein image with low contrast.

As the vein is about 10 to 15 pixels wide, L is set to 15 in this work. If L were too small, thinner vein area would be obtained and some vein area might be missed, while if L were too big vein branches would be missed. k is set to 0.2 in this work. If k were too small, more background areas would be considered as vein area, while if k were too big vein area would be missed. Results from the Niblack and improved Niblack methods are shown in Figure 4-3.

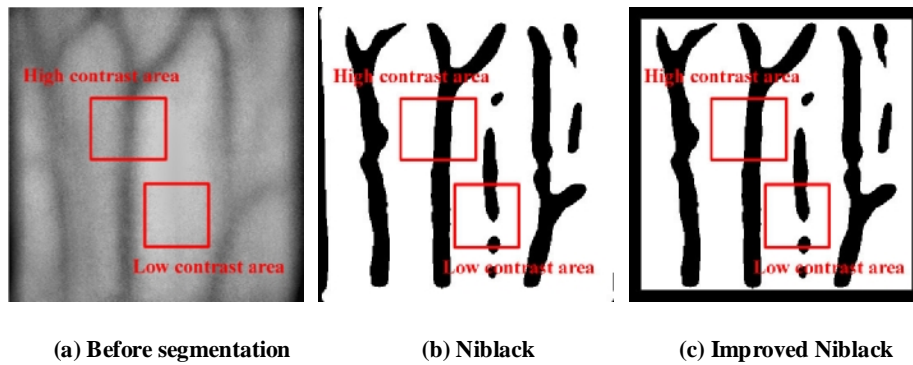


Figure 4-3 Result of Niblack methods

From Figure 4-3(b) and (c), vein area can be segmented correctly in the high contrast areas, but segmentation errors occur in the low contrast areas.

4.2.2. Boundary Methods

With vein patterns shown as narrow branching lines in the image acquired, methods based on boundary characteristics could be appropriate [Wang, Guo, Zhuang *et al*, 2006].

Chapter 4. Segmentation of Vein Image

One such method first labels every pixel as plus, minus or zero based on the first-order gradient calculated by using the Sobel's operator and the second-order gradient by using the Laplacian operator to form a 3-level image $s(x, y)$:

$$s(x, y) = \begin{cases} 0 & \nabla f < T \\ +1 & \nabla f \geq T, \nabla^2 f \geq 0 \\ -1 & \nabla f \geq T, \nabla^2 f \leq 0 \end{cases} \quad (4-14)$$

The resulting image $s(x, y)$ is then scanned horizontally and vertically to find pixels forming the following patterns

$$(\mathbf{K})(-1, +1)(0 \text{ or } +1)(+1, -1)(\mathbf{K}) \quad (4-15)$$

Finally, the centre pixel of the pattern found is assigned a binary value of 1, with others assigned 0. Although this method shows the potential of gradient-based methods to provide good vein pattern segmentation, it is not easy to use because this method requires very high contrast vein images; otherwise, the vein image after segmentation has rough edges as shown in Figure 4-4.

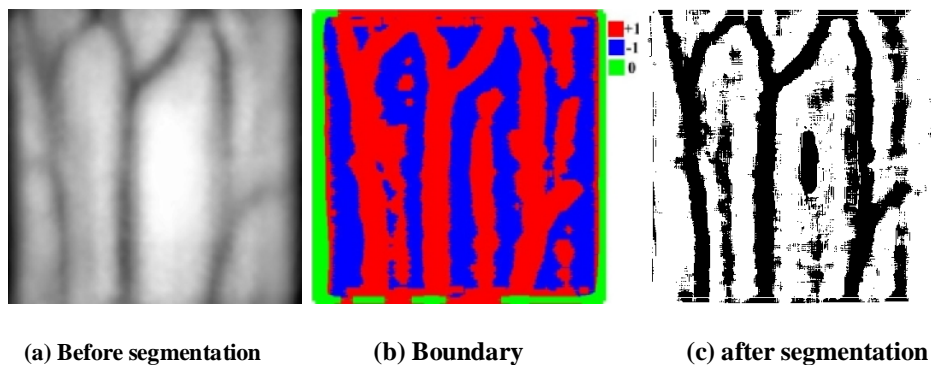


Figure 4-4 Result of boundary method

4.2.3. Gradient Based Image Segmentation

With simplicity offered by the threshold based methods and effectiveness offered by gradient based methods, a method to include the gradient information in the thresholding

Chapter 4. Segmentation of Vein Image

equation was proposed for segmentation [Wang and Wang, 2009].

For equation (4-12), it can be rewritten as

$$T(x, y) = m(x, y) \times \left[1 + k \times \frac{s(x, y)}{m(x, y)} \right] \quad (4-16)$$

By introducing local dynamic range standard deviation (R), a modification is proposed by J. Sauvola [Sauvola and PietikaKinen, 2000] to give:

$$T(x, y) = m(x, y) \times \left[1 + k \times \left(1 - \frac{s(x, y)}{R} \right) \right] \quad (4-17)$$

where $T(x, y)$ is the threshold image in pixel (x, y) , $m(x, y)$ is the mean grey value of neighbourhood $L \times L$ window, $s(x, y)$ is the local standard deviation, R is the maximum grey level standard deviation, which is usually set to $R=128$. From equation (4-17), the right part in the square bracket can be considered as the weight of mean grey value $m(x, y)$. Using gradient to determine the weight, which is, replacing the standard deviation with gradient gives:

$$T(x, y) = m(x, y) \times \left[1 + k(x, y) \times \left(1 - \frac{g(x, y)}{G} \right) \right] \quad (4-18)$$

where $g(x, y)$ is the gradient value of pixel (x, y) . G is the global maximum gradient that is usually set to 255. Furthermore, $k(x, y)$ is the adaptive coefficient that is defined by:

$$k(x, y) = a + b \frac{G(x, y)}{G} \quad (4-19)$$

where $G(x, y)$ is the maximum gradient value in the neighbourhood window of $L \times L$ pixels. a and b are two adaptive coefficients determined by experiments.

Chapter 4. Segmentation of Vein Image

The square bracket term in equation (4-18) can be written as the weight of the mean grey value:

$$W(x, y) = 1 + k(x, y) \times \left(1 - \frac{g(x, y)}{G}\right) \quad (4-20)$$

For this method, first, gradient $g(x, y)$ replaces standard deviation $s(x, y)$, as it offers a better performance in detecting the edges of vessels, and it can also be a measurement of local contrast. Second, $k(x, y)$ can be adaptive according to local contrast. When the local contrast is low, the standard deviation is low, if k does not change in equation (4-16), the weight of the mean grey value is low, the threshold becomes low and some vein areas might be missed. For this method, when the vein image and background have low contrast, the local gradient value $G(x, y)$ is correspondingly low, so in equation (4-19) $k(x, y)$ will adaptively decrease to avoid over-segmentation. A linear model is built to represent $k(x, y)$ for simple implementation and fast computation. Although the linear model is not the best approximation of $k(x, y)$, the experiments indicate that appropriate parameters can get the desired segmentation results.

For the gradients to be calculated, it can be selected based on image characteristics. In the implementation, a two-dimensional gradients based on the following equation was used.

$$g(x, y) = \sqrt{g_x(x, y)^2 + g_y(x, y)^2} \quad (4-21)$$

In selection of the window sizes N and L as well as the two adaptive coefficients a and b , N should be set to the width of a vessel region because it is used for the mean

Chapter 4. Segmentation of Vein Image

value calculation, and L should be no bigger than N because it is used for the gradient calculation and for detecting edges. Appropriate values for α and β can be determined through experiments, and preferable segmentation effects were found with $\alpha = 0.01$, $\beta = 0.02$. If α were too small, more background areas would be considered as vein area, while if α were too big some vein area would be missed. Smaller β makes some boundary information missed while bigger β might make some vein area missed. In this work, N and L are set to 15, as the vein is about 10 to 15 pixels wide. If N and L were too small, some vein area would be missed, while if L were too big more background areas would be considered as vein area. The result of this method is shown in Figure 4-5.

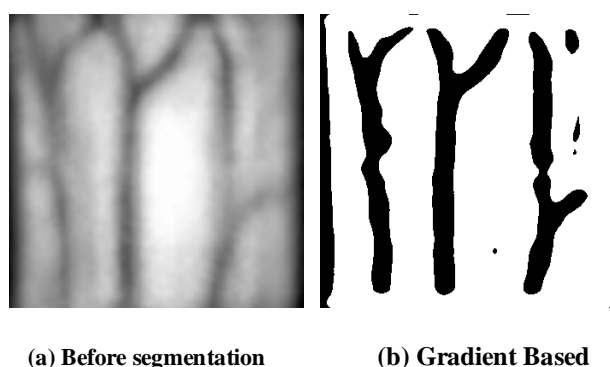


Figure 4-5 Result of gradient based method

Compared with the segmentation results produced by other methods shown in Figures 4-2 to 4-5, the gradient based method is seen to be more effective for its less segmentation errors. More evidence can be found in Appendix B.

4.3. Post-processing

After segmentation, new noises, such as spots on the background area, holes and burrs on the vein area, are brought into the images, as shown in Figure 4-6. Some post-processing operations are needed to reduce them.

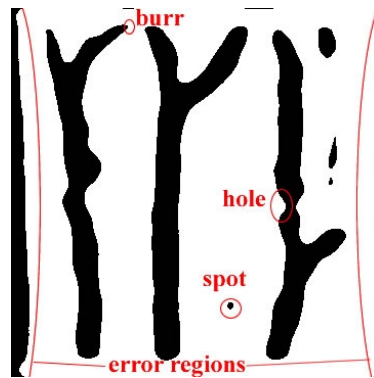


Figure 4-6 Examples of spot, hole and burr

4.3.1. Morphological Filtering

Opening and closing are the basic operations of morphological noise removal. Opening, which is operated by erosion followed by dilation, removes small objects from the foreground, while closing, which is operated by dilation followed by erosion, removes small holes in the foreground [Serra, 1983].

To remove the holes and small spots caused by segmentation, vein images are processed by closing, followed by opening. As extra vein patterns are created near the left and right boundaries of ROI, they are removed by changing all the black pixels connected to the left and right boundaries to white. An example result is shown in Figure 4-7.

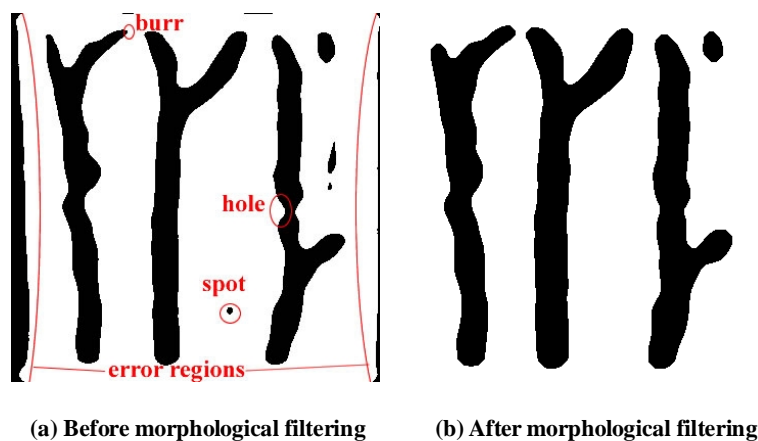


Figure 4-7 Results of morphological filtering

4.3.2. Thinning

From the requirements of some structure feature extraction, such as cross points and branches, vein image need to be thinned.

Thinning is a morphological operation that is mainly used for skeletonisation. It is commonly used to tidy up the output of edge detectors by reducing all lines to single pixel thickness. The result of thinning is shown in Figure 4-8.

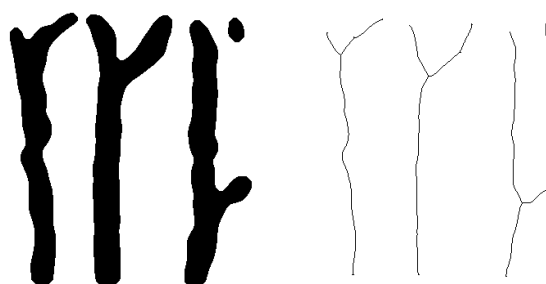


Figure 4-8 Result of thinning

4.4. Summary

In this chapter, some commonly used segmentation methods including Otsu, Threshold image, Niblack, and Boundary are investigated for hand-dorsa vein images.

As Otsu is a method using a fixed threshold, it often results in under segmentation in some parts of the image and over segmentation in other parts of the image. Adaptive threshold methods perform better than using a fixed threshold. The threshold image method is quick but the threshold is the local mean, which cannot divide the vein image and dark background effectively. Niblack and improved Niblack have a good performance in high contrast areas. However, they are not good enough for the low contrast areas.

The boundary method shows the potential of gradient-based methods to provide

Chapter 4. Segmentation of Vein Image

good vein pattern segmentation, it is not easy to use because this method requires very high contrast vein images; otherwise, the vein image after segmentation has rough edges. The gradient based segmentation algorithm introduces gradient information to threshold methods, and it is seen to be more effective for its less segmentation errors. Some post-processing methods, including morphological filtering and thinning, are necessary for extraction of some structure features in vein patterns.

Chapter 5. FEATURE EXTRACTION AND PATTERN RECOGNITION

5.1. Introduction

Feature extraction and pattern recognition are the fundamental parts of an identification system. Feature extraction refers to simplifying the number of variables required to describe a large set of data accurately, and pattern recognition refers to a process of classifying feature patterns.

If a feature space could be used to make different objects in an image to distribute compactly as different feature clusters in separated regions, it will simplify the classifier design. Whereas, it will be hard to improve the accuracy of a classifier if all the features are mixed together. Hence, selection of suitable features is important for pattern recognition.

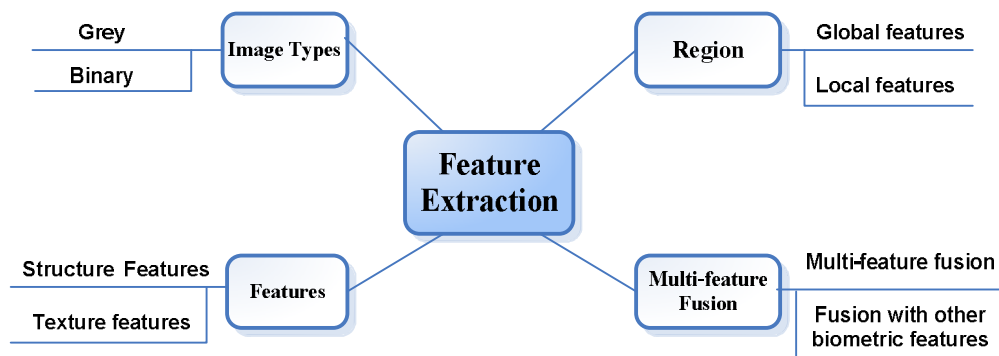


Figure 5-1 Overview of feature extraction

Main ideas of feature extraction are shown in Figure 5-1. They can be divided into different groups based on various categories, such as grey and binary based on image

Chapter 5. Feature Extraction and Pattern Recognition

types, global and local based on region, structure and texture based on feature representation.

To estimate the effectiveness of feature and classifiers, False Acceptance Rate (*FAR*) and recognition rate (*RR*) are commonly used [Jain, Flynn and Ross, 2008].

In one-to-one match mode, the *FAR* is defined as the percentage of identification instances in which false acceptance occurs. This can be expressed as a probability:

$$FAR = \frac{NFA}{NVA} \quad (5-1)$$

where *NFA* is number of false acceptance, and *NVA* is number of verification attempts.

In one-to-many match mode, *RR* is defined as the percentage of identification instance in which correct recognition occurs. This can be expressed as a probability:

$$RR = \frac{NCR}{NIA} \quad (5-2)$$

where *NCR* is number of correct recognition, and *NIA* is number of identification attempts.

For vein pattern recognition, Shahin *et al.* presented a fast spatial correlation algorithm with the *FAR* reported to be 0.02% on a dataset with 500 samples [Shahin, Badawi and Kamel, 2006]; Zhou *et al.* presented multi-resolution filtering and recognition using a correlation coefficient with *FAR* of 2.6% on a database with 265 samples [Zhou, Lin and Jia, 2006]; Cui *et al.* adopted the wavelet moments as features to yield *FAR* of 6% on 50 samples [Cui, Song, Chen *et al.*, 2009]; Liu *et al.* used Hu's invariant moments and a Support Vector Machine (SVM) classifier with *RR* reaching 95.5% on a database with 500 samples [Liu, Liu, Gong *et al.*, 2009], Liu *et al.* proposed

extraction of texture information from the detail images derived from two-level wavelet packet decomposition and obtained a *RR* of 99.07% using K Nearest Neighbourhoods (KNN) and SVM on a database with 1080 samples [Liu, Wang, Li *et al*, 2009].

In the following sections, some feature extraction algorithms will be presented with a new method proposed.

5.2. Classification Methods

5.2.1. Distance Measurements

With classification performed based on distance between feature clusters, there are various distance metrics available, and the Euclidian distance is a common choice because of its simplicity. Since some features to be used are represented using histograms, some metrics for measurement of the distance between two histograms are given in the following.

1) Histogram intersection

$$D(X, Y) = \sum_i \min(X_i, Y_i) \quad (5-3)$$

2) Log-likelihood statistics

$$D(X, Y) = -\sum_i X_i \log Y_i \quad (5-4)$$

3) Chi square distance

$$D^2(X, Y) = \sum_i \frac{(X_i - Y_i)^2}{X_i + Y_i} \quad (5-5)$$

where, $D(X, Y)$ represents the distance between histograms X and Y , with X_i and Y_i denoting their i th bin respectively.

5.2.2. Classifiers

Classification can be thought of as two separate problems - binary classification and multiclass classification. In binary classification, a better-understood task, only two classes are involved, whereas in multiclass classification three or more classes should be distinguished. Presented in the following are some popular classifiers.

A. Nearest Neighbour (NN) [Gutin, Yeo and Zverovich, 2002]

The Nearest Neighbour rule is a commonly used classifier. An input sample is classified by calculating the distance to the training cases, and the minimum of the results then determines the classification of the sample.

Assuming there are c pattern classes denoted by $w_i, i=1,2,\mathbf{K},c$, and each pattern class contains N_i training samples denoted by $v_i^k, i=1,2,\mathbf{K},c; k=1,2,\mathbf{K},N_i$, the discriminant function is:

$$g_i(v) = \min_k \|v - v_i^k\| \quad (5-6)$$

The decision rule is:

$$g_j(v) = \min_k \{g_i(v)\} \Rightarrow v \in w_j \quad (5-7)$$

It means that the input sample is classified to the pattern class based on the nearest distance to one of its member patterns.

B. Mean distance (MD) [Fisher, Perkins, Walker *et al*, 2003]

NN needs to calculate the distances between the input sample and all the training samples, which requires a lot of memory space and large computation. MD uses the average sample of each pattern class as the standard sample and it just needs to compare the

Chapter 5. Feature Extraction and Pattern Recognition

distance between the input sample and the standard samples of all pattern classes. It reduces the computation and is less sensitive to the bad training samples in each pattern classes.

Assuming there are c pattern classes denoted by $w_i, i = 1, 2, \mathbf{K}, c$ and each pattern class contains N_i training samples denoted by $v_i^k, i = 1, 2, \mathbf{K}, c; k = 1, 2, \mathbf{K}, N_i$, the standard samples are calculated by:

$$m_j = \frac{1}{N_j} \sum_{l=1}^{N_j} v_l \quad (5-8)$$

The decision rule is:

$$d(v, m_j) = \min_i(v, m_i) \Rightarrow v \in W_j \quad (5-9)$$

where $d(x, m_j)$ is the Euclidean distance given by

$$d^2(v, m_j) = (v - m_j)^T (v - m_j) \quad (5-10)$$

C. K-Nearest Neighbourhoods (KNN) [Bremner, Demaine, Erickson *et al*, 2005]

The KNN classifier extends NN by taking the k nearest points and assigning the sign of the majority. For an input sample, the distances between it and training points will be calculated, followed by finding the k nearest points. It will be classified to the pattern class that has majority in the k nearest points. It is common to select k small and odd to break ties, such as 1, 3, and 5. When $k = 1$ KNN becomes NN.

D. Support Vector Machine (SVM)

A support vector machine constructs a hyperplane or set of hyperplanes in a high-dimensional (unlimited) space, which can be used for classification.

Chapter 5. Feature Extraction and Pattern Recognition

Whereas the original problem may be stated in a finite dimensional space, it often happens that the sets to discriminate are not linearly separable in that space. For this reason, it was proposed that the original finite-dimensional space be mapped into a much higher-dimensional space, thereby making the separation easier in that space. To keep the computational load reasonable, the mappings used by SVM schemes are designed to ensure that dot products may be computed easily in terms of the variables in the original space, by defining them in terms of a kernel function selected to suit the problem [Press, Teukolsky, Vetterling *et al*, 2007].

Given a training data D , which contains n points:

$$D = \{(v_i, u_i) \mid v_i \in R^p, \quad u_i \in \{-1, 1\}\}_{i=1}^n \quad (5-11)$$

where, v_i is a p -dimensional real vector, u_i is either 1 or -1 , indicating the class to which the point v_i belongs. The maximum-margin hyperplane that divides the points having $u_i = 1$ from those having $u_i = -1$ would be the separating hyperplane. Any hyperplane can be written as the set of points \mathbf{x} satisfying:

$$\mathbf{w} \cdot \mathbf{v} - b = 0 \quad (5-12)$$

where, \cdot denotes the dot product and \mathbf{w} is the normal vector to the hyperplane. The offset of the hyperplane from the origin along the normal vector \mathbf{w} is determined by the parameter $\frac{b}{\|\mathbf{w}\|}$.

Assume the training data are linearly separable, two hyperplanes can be found in a way that they separate the data and there are no points between them, and then try to maximise their distance. The region between them is called "the margin". These

Chapter 5. Feature Extraction and Pattern Recognition

hyperplanes can be expressed by the equations:

$$w \cdot v - b = 1, \quad u_i = +1 \quad (5-13)$$

$$w \cdot v - b = -1, \quad u_i = -1 \quad (5-14)$$

The distance between them is $\frac{b}{\|w\|}$, so that to maximise this distance is to minimise

$\|w\|$. As we also have to prevent data points from falling into the margin, the following constraint is introduced:

$$w \cdot v_i - b \geq 1, \quad v_i \in \text{Class1} \quad (5-15)$$

$$w \cdot v_i - b \leq -1, \quad v_i \in \text{Class2} \quad (5-16)$$

This can be rewritten as:

$$u_i(w \cdot v_i - b) \geq 1, \quad \forall 1 \leq i \leq n \quad (5-17)$$

Then the of optimisation problem of finding $\min \|w\|$ is equivalent to find $\frac{1}{2} \|w\|^2$ that subjects to (5-17).

By introducing Lagrange multipliers a , the previous constrained problem can be expressed as:

$$\min_{w,b} \max_a \left\{ \frac{1}{2} \|w\|^2 - \sum_{i=1}^n a_i [u_i (w \cdot v_i - b) - 1] \right\} \quad (5-18)$$

This problem can now be solved by Quadratic Programming (QP) techniques and the solution can be expressed as a linear combination of the training vectors

$$w = \sum_{i=1}^n a_i u_i v_i \quad (5-19)$$

where v_i corresponding to $a_i > 0$ are defined as the support vectors v_s , which lie on the margin and satisfy $u_i(w \cdot v_i - b) = 1$. So that the support vectors also satisfy

$$u_i \left(\sum_{m \in S} a_m u_m v_m \cdot v_s - b \right) = 1, \quad S = \{i | a_i > 0\} \quad (5-20)$$

Multiplying by y_i and then using $y_i^2 = 1$ from (5-11) and (5-12):

$$b = u_s - \sum_{m \in S} a_m u_m v_m \cdot v_s \quad (5-21)$$

Instead of using an arbitrary support vector x_s , it is better to take an average over all of the support vectors in S :

$$b = \frac{1}{N_S} \sum_{s \in S} [u_s - \sum_{m \in S} a_m u_m v_m \cdot v_s] \quad (5-22)$$

Now the variables w and b are obtained from (5-19) and (5-22), hence the separating hyperplane's optimal orientation is defined and so do the Support Vector Machine.

Multiclass SVM aims to assign labels to instances by using support vector machines, where the labels are drawn from a finite set of several elements.

The dominant approach for doing so is to reduce the single multiclass problem into multiple binary classification problems [Duan and Keerthi, 2005]. Common methods for such reduction include [Duan and Keerthi, 2005, Hsu and Lin, 2002]:

- (i) One-versus-all: Classification of new instances for the one-versus-all case is done by a winner-takes-all strategy, in which the classifier with the highest output function assigns the class.
- (ii) One-versus-one: For the one-versus-one approach, classification is done by a max-wins voting strategy, in which every classifier assigns the instance to

one of the two classes, then the vote for the assigned class is increased by one vote, and finally the class with the most votes determines the instance classification.

5.3. Recognition Based on Structure Features

Presented in this section are some recognition methods investigated in this project, which are based on structure features.

5.3.1. Integral Features

After segmentation, the 2-D integral curves of vein pattern structure are calculated based on the accumulated values of each image row or column, and the correlation between the image acquired and the database is used as judgement of identification. As hand-dorsa vein mainly locate along vertical direction, sum of each image column are calculated as features.

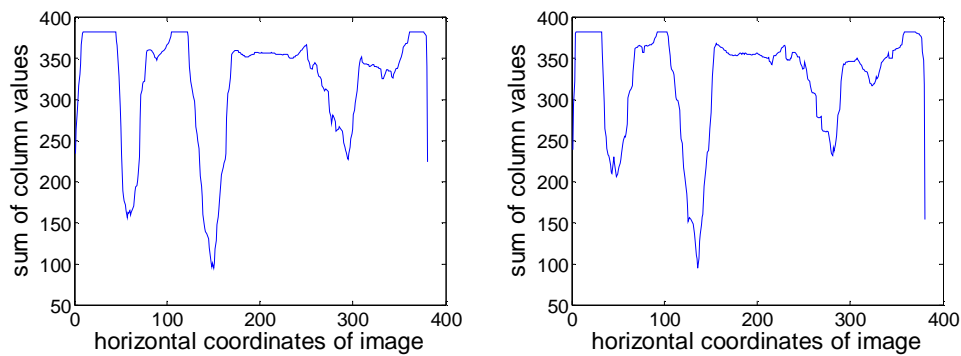


Figure 5-2 Integral curves of two images for the same hand

Figure 5-2 shows the integral curves generated from two images of the same hand, where they are seen to possess very similar shapes with small local differences.

5.3.2. Moment Methods

In statistics, moments are used to characterise the distribution of a variable. If an image is treated as a probability density distribution, the moment of it is a certain particular weighted average (moment) of the image pixels' intensities, which can be used to represent the distribution of grey level values.

A. Hu's invariant moments [Flusser, 2000, Flusser and Suk, 2006, Hu, 1962, Lee, Lee and Park, 2009]

For an $m \times n$ image $f(x, y)$, the moment of order $p + q$ is defined as

$$M_{pq} = \sum_{i=1}^m \sum_{j=1}^n i^p j^q f(i, j) \quad (5-23)$$

It is normalised as:

$$h_{pq} = \frac{M_{pq}}{M_{00}} \quad (5-24)$$

Hu's invariant moments are calculated as follows:

$$M_1 = h_{20} + h_{02} \quad (5-25)$$

$$M_2 = (h_{20} - h_{02})^2 + 4h_{11}^2 \quad (5-26)$$

$$M_3 = (h_{30} - 3h_{12})^2 + (3h_{21} - h_{03})^2 \quad (5-27)$$

$$M_4 = (h_{30} + h_{12})^2 + (h_{21} + h_{03})^2 \quad (5-28)$$

$$M_5 = (h_{30} - 3h_{12})(h_{30} + h_{12}) \left[(h_{30} + h_{12})^2 - 3(h_{21} + h_{03})^2 \right] \\ + (3h_{21} - h_{03})(h_{21} + h_{03}) \left[3(h_{30} + h_{12})^2 - (h_{21} + h_{03})^2 \right] \quad (5-29)$$

$$M_6 = (h_{20} - h_{02}) \left[(h_{30} + h_{12})^2 - (h_{21} + h_{03})^2 \right] + 4h_{11} (h_{30} + h_{12})^2 (h_{21} + h_{03}) \quad (5-30)$$

Chapter 5. Feature Extraction and Pattern Recognition

$$M_7 = (3h_{12} - h_{03})(h_{30} + h_{12}) \left[(h_{30} + h_{12})^2 - 3(h_{21} + h_{03})^2 \right] \\ + (h_{30} - 3h_{12})(h_{21} + h_{03}) \left[3(h_{30} + h_{12})^2 - (h_{21} + h_{03})^2 \right] \quad (5-31)$$

These seven moments are invariant to image shift, scale and rotation.

B. Zernike invariant moments [Belkasim, Ahmadi and Shridhar, 1996, Haddadnia, Ahmadi and Faез, 2003, Teh and Chin, 1998]

As it is moment invariant in polar coordinate space, it is rotation invariant. The Zernike orthogonal polynomial is defined as:

$$V_{nm}(r, \theta) = R_{nm}(r)e^{jm\theta}, \quad m, n \in Z, m \neq 0, n \geq 0 \quad (5-32)$$

where ρ is radius and θ is angle. The radial polynomial is defined as:

$$R_{nm}(r) = \begin{cases} \sum_{s=0}^{\lfloor \frac{n-|m|}{2} \rfloor} \frac{(-1)^s [(n-s)!] r^{n-2s}}{s! (\frac{n+|m|}{2} - s)! (\frac{n-|m|}{2} - s)!} & \text{for } n-|m| \text{ even} \\ 0 & \text{for } n-|m| \text{ odd} \end{cases} \quad (5-33)$$

An image $f(x, y)$ can be expanded as follows:

$$f(x, y) = \sum_{n=0}^{\infty} \sum_m A_{nm} V_{nm}(x, y) \quad (5-34)$$

The Zernike invariant moment of order n for angle m is calculated as:

$$A_{nm} = \frac{n+1}{p} \iint f(x, y) V_{nm}^*(x, y) dx dy \quad (5-35)$$

In a discrete form,

$$A_{nm} = \frac{n+1}{p} \sum \sum f(x, y) V_{nm}^*(x, y) \quad (5-36)$$

Because of the application of orthogonal basis functions, Zernike moments have less redundant information, smaller correlation of features and stronger resistance to noise, compared with Hu's moments.

5.3.3. Keypoint Methods

Endpoints, cross points and the relationships of them have been extracted from the skeleton vein image to present the vein patterns [Wang, Leedham and Choa, 2008]. This method is simple and rapid, but it is not robust, with extracted key features prone to errors due to distortion and noise. To solve these problems, a key points method based on scale-invariant feature transform (SIFT) is presented here [Wang, Fan, Liao *et al*, 2012].

A. Keypoints extraction using SIFT

The scale-invariant feature transform (SIFT) was proposed by Lowe [Lowe, 1999, Lowe, 2004], and it is widely used in computer vision to match images of an object or scene acquired from different viewpoints. Features extracted from the images based on SIFT are not only robust against image scaling, rotation and noise but also invariant to illumination changes. In addition, these features are highly distinctive which means that they are easy to match exactly to the features belonging to the same class in a large database. Based on the method presented in [15], the following four steps are used to extract a set of keypoints from the binary images.

The first step is to detect extremes in all scales and all image positions. For a given image denoted by $I(x, y)$, the scale space of it denoted by $L(x, y, S)$ is produced by convolution with a Gaussian function denoted by $G(x, y, S)$:

$$L(x, y, S) = G(x, y, S) \otimes I(x, y) \quad (5-37)$$

where \otimes denotes convolutional process. The difference-of-Gaussian (DOG) space is given by:

$$D(x, y, s) = L(x, y, ks) - L(x, y, s) \quad (5-38)$$

where k is a constant factor in the scale space and $k=21/s$, with s denoting the intervals in each octave in the scale space. Keypoints (feature points) are identified as the local maximum or minimum of the DoG images across scales. In the implementation, using four octaves, with $s=3$, and $\sigma=1.6$, extreme of the DoG images are detected by comparing each pixel with its 26 neighbours in a $3 \times 3 \times 3$ region at current and adjacent scales. The second step is to remove unreliable keypoints. While a threshold is used to reject keypoints detected in the low contrast areas those are likely to be caused by noise, edge curvatures are used to reject unstable keypoints detected along relatively straight lines. Furthermore, an additional operation is introduced to remove the keypoints occurring in the non-vein region indicated by binary one in the segmented image. The results of keypoints before and after removing are shown in Figure 5-3.

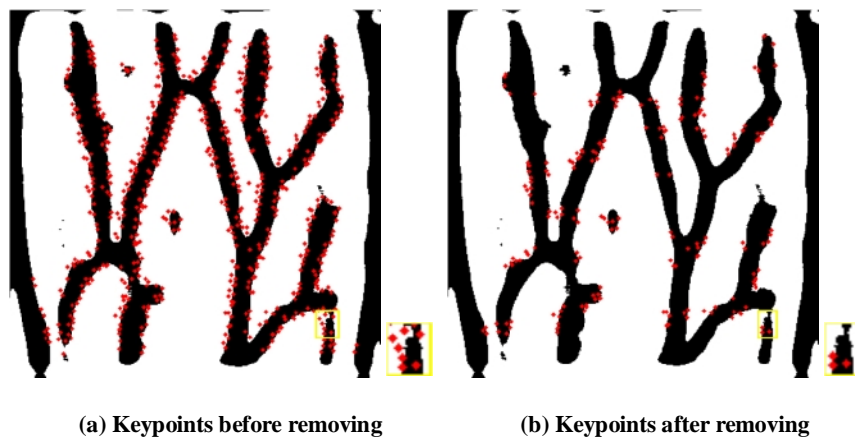


Figure 5-3 Keypoints before and after removing

Chapter 5. Feature Extraction and Pattern Recognition

The third step is to identify the dominant orientation of each keypoint based on the local image characteristics. For each pixel in a region of 32×32 pixels around each keypoint, the gradient magnitude, $m(x, y)$, and orientation, $q(x, y)$, are computed using

$$m(x, y) = \sqrt{(L(x+1, y) - L(x-1, y))^2 + (L(x, y+1) - L(x, y-1))^2} \quad (5-39)$$

$$q(x, y) = \tan^{-1}((L(x, y+1) - L(x, y-1)) / (L(x+1, y) - L(x-1, y))) \quad (5-40)$$

The computed values are then used to form a gradient magnitude weighted orientation histogram of 36 bins with the peak taken as the keypoint orientation.

The fourth step is to construct a local image descriptor for each keypoint. The area around each keypoint is rotated by an angle given by the dominant orientation, and divided into 8×8 regions with each region covering 4×4 pixels. The image gradient magnitudes and orientations are computed to form an 8×8 histograms with 16 orientations per histogram, and the resulting histograms are concatenated to yield the keypoint descriptor as a SIFT feature vector with 1,024 dimensions. Although the dimensionality of the keypoint descriptor used is high, it has been found to provide a better performance than those using lower-dimensional descriptors in this work.

B. Matching and fusion

Recognition of a hand vein is based on the result of matching keypoints extracted from the image to be recognized with keypoints pre-extracted from the training images. In this work, the vector angles in the SIFT feature space between each keypoint in the test image and those in the database are determined by using

$$q_{m,n} = \cos^{-1}(des_{(test,m)} \bullet des_{(train,n)}) \quad (5-41)$$

where $des_{(test,m)}$ and $des_{(train,n)}$ denote the descriptor of the keypoint with index m in the

test image and the descriptor of the keypoint with index n in the database, respectively. For a given keypoint in the test image, if the ratio of the smallest angle to the second smallest angle is less than 0.9, it is considered as a match.

Matched keypoints may contain incorrect matches as shown in Figure 5-4(a). As two or more keypoints extracted from a training image may be matched to the same keypoint in the test image simultaneously, an additional step is introduced to select the matched pairs with the minimum Euclidean distance between their feature vectors in the SIFT space as the correct match pairs. Figure 5-4(b) shows the results of introducing match selection to Figure 5-4(a).

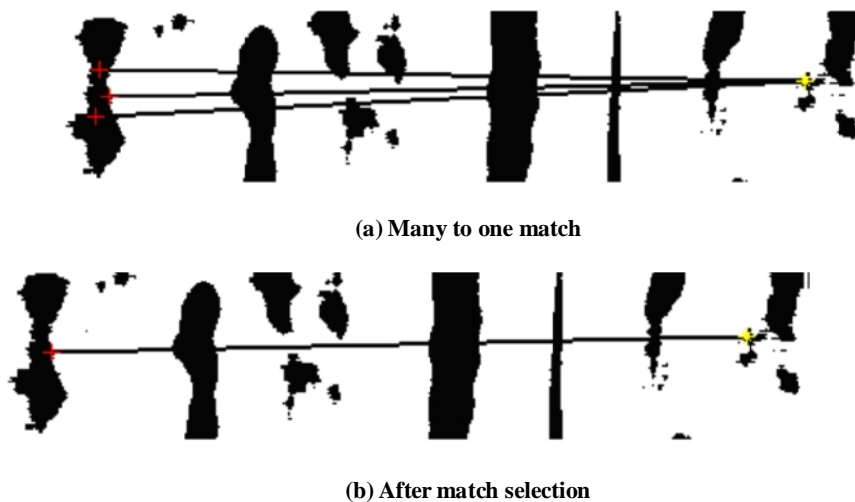


Figure 5-4 Results of match selection

Since the training database can contain multiple hand vein images of each hand, a possibility is therefore there to merge keypoints sets from more than one training image of each hand for hand vein recognition. The fused keypoints sets produced by the multiple keypoints sets extracted from the training images can be used to improve the final classification accuracy. Not only the fused keypoints sets can be used to derive the most discriminatory information from multiple feature sets involved in fusion, but also it

Chapter 5. Feature Extraction and Pattern Recognition

can be used to eliminate the redundant information resulting from the correlation between distinct feature sets, (which can also make the subsequent decision in real time possible) [Yang, Yang, Zhang *et al*, 2003]. In other words, keypoints sets fusion is capable of deriving and providing the most effective and least-dimensional feature vectors sets that benefit the final decision. In the fusion method proposed, the multiple keypoints sets from the same class are combined into one set of feature vectors and then the matching strategy is implemented for keypoints selection.

Let A , B and C be three feature vectors defined on hand vein training pattern space Ω . For an arbitrary sample $x \in \Omega$, let the combined feature of ζ be defined by:

$$d = \begin{pmatrix} a \\ b \end{pmatrix} \quad (5-42)$$

where $a \in A$, and $b \in B$. If feature vector a and b are 1,024 dimensions, then the combined feature vectors form a 2,048 dimensional combined feature space. Since the combined feature vectors are high dimensional, they contain much redundant information and some conflicting information which are unfavourable for recognition. Using the matching strategy described above, matching correlation of a , b with γ ($\gamma \in C$) can be derived. Assuming that γ is matched with b , vector b is removed from the combined vectors d and the final fused feature sets is $d' = (a)$.

Let M be the number of vein images per hand in the training database. The fused keypoint set merges overlapping keypoints among M keypoint sets from the same hand and removes keypoints overlapping with other keypoints of other hands. For a single keypoint of combined keypoints set, once a matched keypoint has been found in

keypoints sets of other hands, it will be deleted. Finally, the fused keypoint set T_i is given by:

$$T_i = \bigcup_{j=1}^M des_i^j - \left(\bigcup_{j=1}^M des_i^j \right) \cap \bigcap_{k \neq i, j=1}^M des_k^j \quad (5-43)$$

where the first term denotes the combined feature vectors sets in M keypoint sets of the hand with index i , the second term denotes the removal of those feature vectors sets which are matched with the vectors contained in M keypoint sets of other hands denoted by k in the training database.

In general, the fusion is a process of reprocessing the combined keypoint set. After keypoints selection, the favourable discriminatory information of hand dorsal vein is remained and at the same time the unfavourable redundant information is eliminated.

5.3.4. Experimental Results

To investigate the recognition performance based on structure features, the database was divided into two sets A and B. Set A has N_A images of every hand, and Set B has the rest. Set A is used for training, and Set B is used for testing.

Here, the size of training set N_A is set to 5, which contains the 1st, 3rd, 5th, 7th, 9th images of each hand in the database, and the rest are used for testing. Images are scaled to 256×256 and divided into 64 rectangular sub-images. Integral histogram, Hu's invariant moments and Zernike invariant moments are extracted from each sub-image and then are connected to form a feature vector.

A. Integral feature

For integral histogram, accumulation of column, row and both of them were tested. For

Chapter 5. Feature Extraction and Pattern Recognition

each input hand-dorsa vein image, its integral histogram is correlated with the integral histograms of all the images in the training set, and the maximum correlation value with a particular training image among all the correlation results produced is taken as a correct match. Table 5-1 summarises all the recognition results obtained.

Table 5-1 Recognition rate (%) of integral histogram

Integral histogram	RR (%)
Column	95.39
Row	49.61
Column and row	88.63

It can be seen from the table that the recognition rate produced by using the integral histogram of columns is nearly double of that produced by the integral histogram of rows. This is due to the column based integral histogram capturing the vein structure information that is mainly oriented in the vertical direction of the image. Furthermore, recognition performance decreases by adding the vein structure information derived from the integral histogram of rows to the vein structure information derived from the integral histogram of columns.

B. Moment methods

For the structure features based on moments, $M_1 \sim M_7$ of the Hu's invariant moments and for A_{00} , A_{11} , A_{20} , A_{22} , A_{31} , A_{33} , A_{40} , A_{42} and A_{44} of the Zernike moments were tested using the NN classifier to investigate their recognition performance. The results are shown in Table 5-2 and Table 5-3.

Chapter 5. Feature Extraction and Pattern Recognition

Table 5-2 Recognition rate (%) of Hu's invariant moments

Hu's moments	RR (%)
M_1	95.20
M_1, M_2	84.71
M_1, M_2, M_3	87.84
M_1, M_2, M_3, M_4	87.75
M_1, M_2, M_3, M_4, M_5	85.88
$M_1, M_2, M_3, M_4, M_5, M_6$	86.27
$M_1, M_2, M_3, M_4, M_5, M_6, M_7$	86.27

Table 5-3 Recognition rate (%) of Zernike invariant moments

Zernike moments	RR (%)
A_{00}	95.39
A_{00}, A_{11}	87.54
A_{00}, A_{11}, A_{20}	88.73
$A_{00}, A_{11}, A_{20}, A_{22}$	90.98
$A_{00}, A_{11}, A_{20}, A_{22}, A_{31}$	90.58
$A_{00}, A_{11}, A_{20}, A_{22}, A_{31}, A_{33}$	91.57
$A_{00}, A_{11}, A_{20}, A_{22}, A_{31}, A_{33}, A_{40}$	91.67
$A_{00}, A_{11}, A_{20}, A_{22}, A_{31}, A_{33}, A_{40}, A_{42}$	90.88
$A_{00}, A_{11}, A_{20}, A_{22}, A_{31}, A_{33}, A_{40}, A_{42}, A_{44}$	91.18

From the two tables, it is observed that increasing the number of moment orders does not increase the recognition performance in both Hu's and Zernike. With the coarse structure information described by low order moments and the fine structure information described by high order moments, adding structure features represented by higher order moments will result in recognition performance affected by noise and distortion due to too much detail information being included in the feature vector. Furthermore, there is little difference in the recognition performance by using the lowest order of moment in either method.

C. Key points methods

Based on four sets of keypoints extracted from the training images of each hand ($M=5$), three different feature sets, namely, single keypoint set, all keypoint set, and fused keypoint set, are tested to demonstrate the performance of the proposed feature fusion

method. The results of the recognition performance are shown in Table 5-4.

Table 5-4 Result of recognition performance

Matching strategy	Keypoint set	RR(%)
Vector angles	Single keypoint set	78.04
	All keypoint sets	94.91
	Fused keypoint set	97.15
Vector angles +Euclidean distance	Single keypoint set	78.73
	All keypoint sets	95.98
	Fused keypoint set	98.14

It is seen from Table 5-4 that the matching strategy which combines the vector angles strategy and Euclidean distance strategy provides a higher correct recognition rate than the matching strategy based on only vector angles, with a recognition improvement around 1%, for each type of keypoint set. The best classification accuracy is seen to be provided by the fused keypoint set, followed by the all keypoint set, with the lowest from the single keypoint set. This could be explained by the fact that the single keypoints set contains probably too little features, and the all keypoint set probably too many features. A more appropriate set of feature vectors is seen to be provided by the proposed fusion method as evidence by the highest correct recognition rate reaching almost 98%.

5.4. Recognition Based on Texture Features

5.4.1. Local Binary Patterns

Local binary pattern (LBP) is a powerful means of texture description [Ahonen, Pietikainen, Hadid *et al*, 2004, Ojala, Pietikäinen and Mäenpää, 2002]. It is an efficient rotation-invariant texture classification technique. An illustration of the basic LBP operator is shown in Figure 5-5. For each pixel in an image, its value is compared with all the neighbouring pixel values. The result of each comparison is coded as binary 0 if the centre pixel value is smaller and binary 1 otherwise. The binary bits are then grouped in

the clockwise direction starting from the top left pixel, and the arranged binary string is converted to a decimal number as the final LBP result for the centre pixel

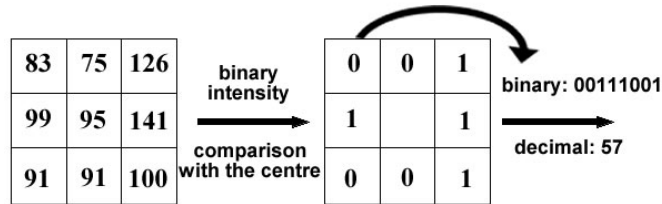


Figure 5-5 Example of basic LBP operator

Ojala *et al.* extended the operator to use neighbourhoods of different sizes [Ahonen, Pietikainen, Hadid *et al.*, 2004, Ojala, Pietikäinen and Mäenpää, 2002]. Using circular neighbourhoods and bilinearly interpolating the pixel values allows any radius and number of pixels in the neighbourhoods to be used. Let $LBP_{P,R}$ denote the LBP operation based on P sampling points on a circle of radius of R , some examples of the circular neighbourhoods are shown in Figure 5-6.

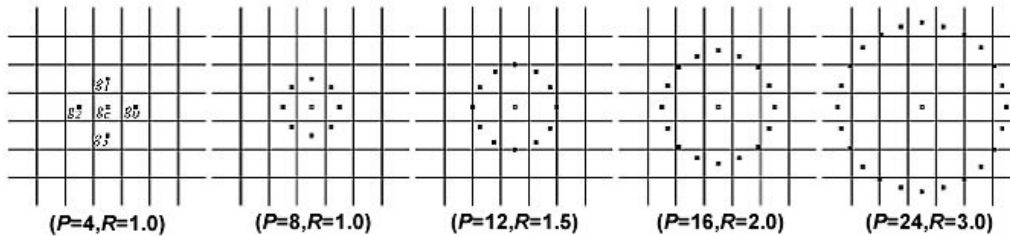


Figure 5-6 Circular neighbourhoods for LBP operator

To remove the effect of image rotation resulting in different binary patterns to be generated, each LBP is rotated to a position that acts as the common reference for all rotated versions of the binary patterns, and this involves the use of the rotation invariant LBP operator denoted by $LBP_{P,R}^{ri}$ and defined as:

$$LBP_{P,R}^{ri} = \min \{ROR(LBP_{P,R}, i) | i = 0, 1, 2, \dots, P-1\} \quad (5-44)$$

where $ROR(x,i)$ performs a circular bitwise right shift i times on the P -bit binary number denoted by x .

Another extension to the original method is called uniform patterns [Ahonen, Pietikainen, Hadid *et al*, 2004, Ojala, Pietikäinen and Mäenpää, 2002]. A local binary pattern is called uniform if it contains at most two bitwise transitions from 0 to 1, or vice versa when the binary string is circularly shifted. For example, 00000000, 00001111 and 10000011 are uniform patterns with zero, one and two bitwise transitions from 0 to 1 separately. Let $LBP_{p,R}^{u2}$ denote the operation used to generate LBP uniform patterns, Figure 5-7 shows the 36 rotation invariant patterns produced by the $LBP_{8,R}^{ri}$ operator, of which the 9 patterns in the first row are uniform.

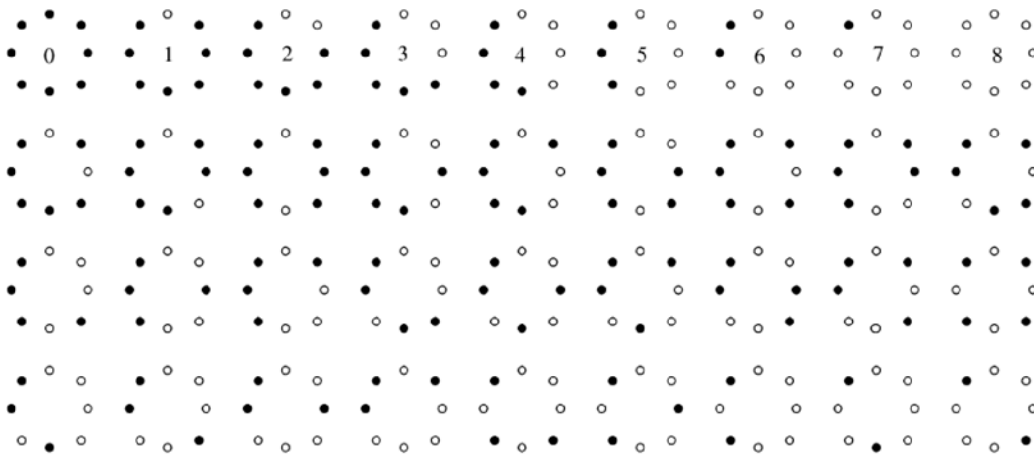


Figure 5-7 36 rotation invariant patterns produced by $LBP_{8,R}^{ri}$ operator

5.4.2. Partition Local Binary Patterns (PLBP)

To represent the vein pattern in more detail, it is proposed to divide the vein image into non-overlapping rectangular or circular regions [Wang, Li and Cui, 2010]. This is illustrated in Figure 5-8, where a hand-dorsa vein image is divided into 64 rectangular

regions and 16 circular regions respectively.

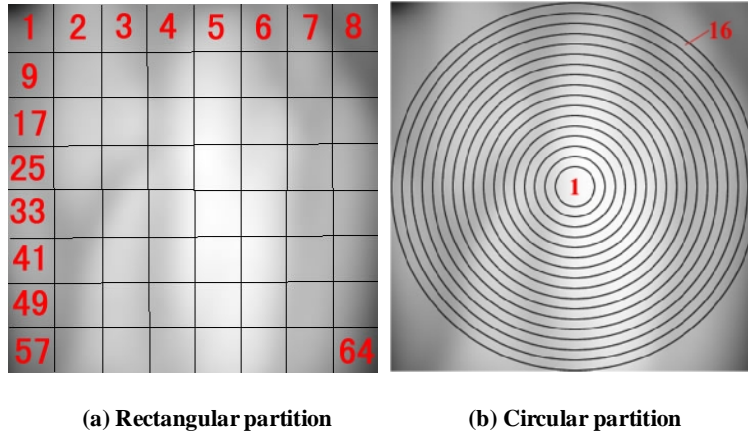


Figure 5-8 Sketches of image partitions

After partition into non-overlapping rectangular regions, based on rotation invariant uniform patterns computed using the $LBP_{8,2}^{riu2}$ operator, the texture contained in each sub-image is represented using a histogram by grouping possible LBP patterns produced into 10 texture categories based on 9 rotation invariant uniform patterns and one other pattern. Let the number of occurrence of a particular texture category in the i th sub-image be denoted by $h_{i,j}$, where $j=1$ to 10, then the feature histogram of the i th sub-image can be expressed as

$$H_i = [h_{i,1} \quad h_{i,2} \quad \mathbf{L} \quad h_{i,10}] \quad (5-45)$$

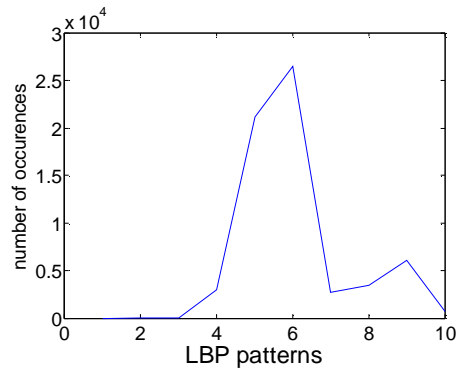
If the number of non-overlapping rectangular sub-images is denoted by N , then the texture feature in a hand-dorsa vein image can be represented by a vector V of $10N$ dimensions based on concatenation of N LBP feature histograms:

$$V = [H_1 \quad H_2 \quad \mathbf{L} \quad H_N] \quad (5-46)$$

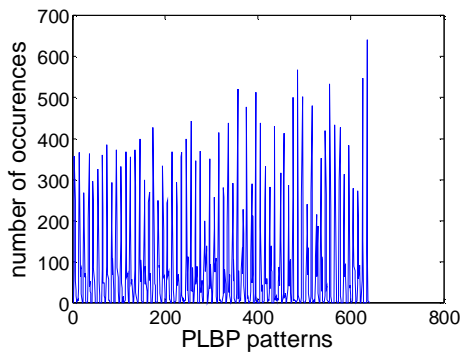
Figure 5-9 shows the feature histograms produced by applying the $LBP_{8,2}^{riu2}$ operator to the hand-dorsa vein image shown in Figure 5-8, where (a) is produced directly without

Chapter 5. Feature Extraction and Pattern Recognition

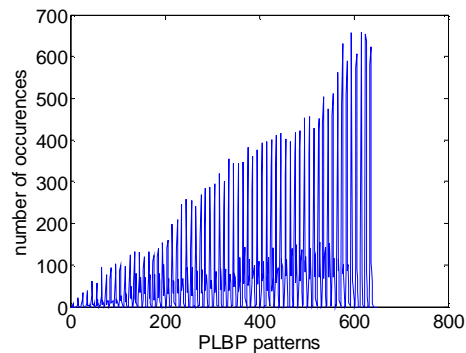
image partition and with image texture represented by 10-element feature vector, (b) is produced by partitioning the image into 64 rectangular sub-images and with image texture represented by a much longer feature vector of 640 elements, and (c) is produced by partitioning the image into 64 circular rings with the same feature vector length as (b).



(a) Original $LBP_{8,2}^{riu2}$ histogram



(b) Rectangular partition



(c) Circular partition

Figure 5-9 Feature histograms of 64 sub-images PLBP and original LBP

Since the number of non-overlapping sub-images is set to the integer power of 2, image scaling operation is required before image partition. From the experiments performed, both the image size and the number of sub-images have an impact on the recognition performance. With the rectangular partition based on the image size of 256x256 and the number of sub-images of 64 found to provide the best performance, this

forms the focus of the following sections.

5.4.3. Weighted Partition Local Binary Patterns (WPLBP)

To improve the rectangular PLBP (RPLBP), feature histograms of sub-images are studied in detail. From Figure 5-10 which shows the feature histogram of one sub-image (the first rectangular sub-image in Figure 5-8(a)), it is seen that the fifth and sixth binary patterns (corresponding to 00001111 and 00011111) have much higher occurrences than other binary patterns.

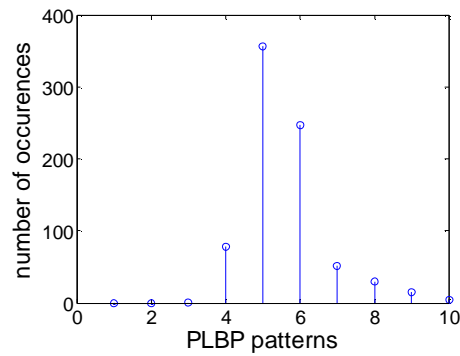


Figure 5-10 Feature histogram of sub-image 1

Further analysis of all the sub-image histograms reveals this as a common phenomenon with the occurrence of fifth and sixth binary patterns found to be more than others in each sub-image. The proportions of different patterns computed from all the images in the database are given in Table 5-5.

Chapter 5. Feature Extraction and Pattern Recognition

Table 5-5 Proportions of patterns

Patterns	Number of occurrences	Proportion (%)
1	7538	0.01
2	53171	0.05
3	116344	0.11
4	5796903	5.66
5	38485992	37.6
6	38305358	37.42
7	4751973	4.64
8	5366668	5.24
9	8316796	8.13
10	1158297	1.13

From Table 5-5, it is seen that the fifth and sixth patterns occur more than 75% together. To study the contributions of 10 patterns to the recognition result, recognition experiments were performed based on individual patterns using NN classifier with the Euclidian distance. The results are shown in Table 5-6, where patterns 1 and 5 are seen to offer the least and most useful texture information for recognition respectively.

Table 5-6 Recognition results based on individual patterns

Pattern	1	2	3	4	5	6	7	8	9	10
Recognition Rate (%)	2.06	10.98	26.67	93.24	96.47	96.08	93.82	90.59	85.98	42.84

Based on the relative importance of each pattern observed from Table 5-6, feature weighting is proposed to yield weighted PLBP (WPLBP) to improve hand-dorsa vein pattern recognition [Wang, Li, Shark *et al*, 2011]. For the k th binary pattern, if r_k is the recognition rate, then the weighting of it, denoted by w_k , is proposed to be:

$$w_k = \frac{r_k}{\sum_{i=1}^{10} r_i} \quad (5-47)$$

Applying (5-47) to (5-46) yields the resulting WPLBP as follows:

$$V_w = [H_1W \quad H_2W \quad \mathbf{L} \quad H_NW] \quad (5-48)$$

where

$$W = \begin{bmatrix} w_1 & 0 & \mathbf{L} & 0 \\ 0 & w_2 & \mathbf{L} & 0 \\ & & \mathbf{O} & \\ 0 & 0 & \mathbf{L} & w_{10} \end{bmatrix} \quad (5-49)$$

5.4.4. Experimental Results

In the following experiments carried out to evaluate the training size requirement as well as the recognition performance based PLBP and WPLBP, NN classifier was used with Euclidian distance.

A. Training size based experiments

These experiments are designed to find the suitable training data size. For each size of the training data set with the number of images used increasing from 1 to 9 ($N_A=1, 2 \dots 9$), 10 tests were performed with the training samples selected randomly in each test. Each image was scaled down to 256×256 pixels and divided into 64 rectangular sub-images. While Table 5-7 to Table 5-15 provide all the results obtained for 9 different sizes of the training data set, the best, worst and average performances over 10 tests for each size of the training data set are given in Table 5-16.

Chapter 5. Feature Extraction and Pattern Recognition

Table 5-7 Result of training sets experiments ($N_A=1$)

Training samples	1	2	3	4	5
Recognition rate (RR) (%)	80.1198	82.3529	87.2549	88.6166	89.2702
Training samples	6	7	8	9	10
RR (%)	89.1612	88.8344	88.5621	88.671	87.7996

Table 5-8 Result of training sets experiments ($N_A=2$)

Training samples	1, 2	1, 3	1, 4	1, 9	3, 4
RR (%)	89.3382	93.1373	94.5466	95.5882	93.3824
Training samples	3, 7	5, 6	5, 7	5, 8	7, 8
RR (%)	95.8333	93.1985	94.6078	94.2402	0.921569

Table 5-9 Result of training sets experiments ($N_A=3$)

Training samples	1, 2, 3	1, 2, 8	1, 5, 8	1, 7, 8	2, 8, 9
RR (%)	93.6975	97.3389	97.1989	96.2185	97.409
Training samples	3, 5, 8	5, 6, 7	5, 8, 9	6, 7, 8	7, 8, 9
RR (%)	96.9188	95.3081	95.3081	94.5378	93.7675

Table 5-10 Result of training sets experiments ($N_A=4$)

Training samples	1,2,3,4	1,2,5,6	1,2,6,9	1,2,8,9	1,5,8,9
RR (%)	96.8137	97.2222	98.8562	98.366	97.549
Training samples	2,5,7,9	2,5,8,9	2,6,7,9	1,2,6,10	7,8,9,10
RR (%)	97.9575	97.8758	98.4477	98.7745	93.5458

Table 5-11 Result of training sets experiments ($N_A=5$)

Training samples	1,3,5,7,9	1,2,5,6,7	1,2,5,7,9	1,2,6,7,9	1,2,6,7,8
RR (%)	98.3333	98.7255	98.7255	99.4118	98.5294
Training samples	3,4,6,7,9	2,3,6,7,9	4,5,6,7,9	1,2,5,9,10	6,7,8,9,10
RR (%)	97.2549	98.3333	96.0784	98.4314	94.0196

Table 5-12 Result of training sets experiments ($N_A=6$)

Training samples	1,2,3,4,5,6	1,2,5,6,7	3,4,5,7,8,10	3,4,5,6,7,10	2,3,4,6,7,10
RR (%)	97.9167	99.2647	97.549	97.3039	98.5294
Training samples	1,3,4,6,8,10	1,3,4,6,7,10	1,3,4,5,8,10	3,4,7,8,9,10	5,6,7,8,9,10
RR (%)	98.5294	99.0196	98.5294	97.0588	94.8529

Chapter 5. Feature Extraction and Pattern Recognition

Table 5-13 Result of training sets experiments ($N_A=7$)

Training samples	1,2,3,4,5,6,10	1,2,3,5,6,7,9	1,2,3,4,6,7,10	1,2,3,4,8,9,10	1,2,4,6,7,9,10
RR (%)	99.183	99.183	100	98.8562	100
Training samples	1,3,4,5,6,7,10	2,3,4,5,6,9,10	2,3,4,6,7,9,10	3,4,5,6,7,9,10	4,5,6,7,8,9,10
RR (%)	98.8562	97.3856	98.2026	96.732	94.4444

Table 5-14 Result of training sets experiments ($N_A=8$)

Training samples	1,2,3,4,5,6,9,10	1,2,3,4,6,7,9,10	1,2,3,4,6,8,9,10	1,2,3,4,7,8,9,10	1,2,4,5,6,8,9,10
RR (%)	98.7745	100	99.2647	99.0196	99.5098
Training samples	1,2,5,6,7,8,9,10	2,3,4,5,6,7,8,10	2,3,5,6,7,8,9,10	2,4,5,6,7,8,9,10	3,4,5,6,7,8,9,10
RR (%)	99.0196	97.0588	96.5686	96.5686	95.3431

Table 5-15 Result of training sets experiments ($N_A=9$)

Training samples	1,2,3,4,5 6,7,8,9	1,2,3,4,5 6,7,8,10	1,2,3,4,5 6,7,9,10	1,2,3,4,5 6,8,9,10	1,2,3,4,5 7,8,9,10
RR (%)	99.5098	100	100	98.5294	99.0196
Training samples	1,2,3,4,6 7,8,9,10	1,2,3,5,6 7,8,9,10	1,2,4,5,6 7,8,9,10	1,3,4,5,6 7,8,9,10	2,3,4,5,6 7,8,9,10
RR (%)	100	98.5294	100	96.5686	94.6078

Table 5-16 Recognition rate (%) of using different number of training images

Training Images N_A	Test images	Recognition rate (%)		
		Max	Min	Average
1	1836	89.27	80.12	87.06
2	1632	95.83	89.34	93.60
3	1428	97.41	93.70	95.77
4	1224	98.86	93.55	97.54
5	1020	99.41	94.02	97.78
6	816	99.26	94.85	97.86
7	612	100	94.44	98.28
8	408	100	95.34	98.11
9	204	100	94.61	98.68

Obviously, as the number of training images increases, the number of images available for test is decreased, and the recognition performance is improved with more

Chapter 5. Feature Extraction and Pattern Recognition

time required for computation. Considering recognition result and balance of training set and test set, $N_A=5$ is adopted in this work.

B. PLBP

The number of images used for training is 5, and they are selected as the 1st, 3rd, 5th, 7th and 9th images of the 10 images of each hand in the database. For the experiments related to rectangular PLBP (RPLBP), the size of each image is scaled down to $M \times M$ pixels with $M = 2^6, 2^7, 2^8$, and the number of sub-images used is set to $N = 2^2, 2^3, \mathbf{L}, 2^8$. Based on different combinations of M and N , the recognition rates produced are shown in Table 5-17. As the operation performed by using $LBP_{8,2}^{riu2}$ cannot be carried out if sub-image is smaller than 5×5 , there are no results for $M=64$, and $N=128, 256$.

For circular PLBP (CPLBP), the maximum number of sub-images is smaller than that in the rectangular partition method. Results of recognition experiments with $M = 2^6, 2^7, 2^8$ and $N = 2^2, 2^3, \mathbf{L}, 2^6$ are shown in Table 5-18. When $M=64, N=64$, image cannot be divided for circular mode, so that no result was obtained.

Table 5-17 Recognition rate (%) of RPLBP with different M and N

$N \backslash M$	RR (%)	64	128	256
4		84.41	82.16	85.69
8		94.41	93.04	94.61
16		96.18	96.86	96.71
32		96.96	97.65	97.83
64		96.76	97.84	98.33
128		-	97.25	97.75
256		-	97.16	97.25

Table 5-18 Recognition rate (%) of CPLBP with different M and N

$N \backslash M$ RR (%)	64	128	256
4	79.31	78.24	85.98
8	84.80	81.27	86.96
16	83.33	82.94	87.94
32	80.59	80.98	86.57
64	-	77.75	82.94

It can be seen from the results, RPLBP performs better than CPLBP and the highest recognition rate occurs at $M=256$ pixels for both RPLBP and CPLBP. Furthermore, there is a trend of dependency between the number of sub-images and the recognition rate produced. For a given image size, as the number of sub-images increases with the area of each sub-image decreases, the recognition rate is seen to increase with it. However, when the number of sub-image is sufficiently large resulting in a small area for each sub-image, the recognition rate begins to fall. While the former could be explained by insufficient local texture information inherent for discriminating between two different hand-dorsa vein images due to large sub-images, and the latter could be explained by a bigger influence of the local texture noise in hand-dorsa vein pattern recognition due to small sub-images, resulting in an increase in misclassification. From the experimental results the most suitable number of sub-images is observed to be 64 for RPLBP and 16 for CPBLP when $M=256$.

C. WPLBP

With the number of images used for training set to 5 and the training images selected as the 1st, 3rd, 5th, 7th and 9th images of the 10 images of each hand in the database, the recognition performance of WPLBP was investigated. Using $M=256$ and $N=64$, the weights of WPBLP are set by equation (5-47) and Table 5-6 to give

Chapter 5. Feature Extraction and Pattern Recognition

$$\begin{aligned} w_1=0.0032, w_2=0.0172, w_3=0.0418, w_4=0.1460, w_5=0.1510; \\ w_6=0.1504, w_7=0.1469, w_8=0.1418, w_9=0.1346, w_{10}=0.0671 \end{aligned} \quad (5-50)$$

The recognition rate achieved by using WPLBP is compare with the highest recognition rate achieved by using RPLBP in Table 5-19.

Table 5-19 Comparison of WPLBP and RPLBP

Method	RR (%)
RPLBP	98.33
WPBLP	98.43

From Table 5-19, recognition based on WPLBP is seen to make a slight improvement in the performance compared with that achieved based on RPLBP. This slight improvement could be explained by the slight weight adjustment, as if all the weights are set to 0.1, then WPLBP is same as RPLBP.

5.5. Recognition based on multi-feature fusion

From the previous section, RPLBP is shown to offer a good basis of texture feature to provide a high recognition rate that is around 98%. Additionally, WPBLP is shown to increase the recognition rate slightly by controlling the contribution of each texture category based on their relative importance. These have let to further work presented in this sub-section to introduce additional control of RPLBP via multi-feature fusion in order to achieve even higher recognition rate.

5.5.1. PLBP and Vein Structure

One possibility to control the contribution of RPLBP is to utilise the vein structure pattern. Since image segmentation yields a binary image with vein areas and non-vein areas represented by 0s and 1s respectively (see section 4.2), it could be used as a mask to

Chapter 5. Feature Extraction and Pattern Recognition

allow only those PLBP in the vein areas to be used in the classification process. Before using the binary image as the mask, it should be processed by morphological closing and opening operations to ensure full coverage of the vein areas and their boundary regions without causing any loss of discriminative texture information. As the vein width is about 10 to 15 pixels, a mask with a size of 15×15 pixels and a shape similar to diamond is designed for the morphological closing and opening operations, which is shown in the following:

$$M_{15 \times 15} = \begin{bmatrix} 0 & 0 & 0 & 0 & 1 & 1 & 1 & 1 & 1 & 1 & 1 & 0 & 0 & 0 & 0 \\ 0 & 0 & 0 & 1 & 1 & 1 & 1 & 1 & 1 & 1 & 1 & 1 & 0 & 0 & 0 \\ 0 & 0 & 1 & 1 & 1 & 1 & 1 & 1 & 1 & 1 & 1 & 1 & 1 & 0 & 0 \\ 0 & 1 & 1 & 1 & 1 & 1 & 1 & 1 & 1 & 1 & 1 & 1 & 1 & 1 & 0 \\ 1 & 1 & 1 & 1 & 1 & 1 & 1 & 1 & 1 & 1 & 1 & 1 & 1 & 1 & 1 \\ 1 & 1 & 1 & 1 & 1 & 1 & 1 & 1 & 1 & 1 & 1 & 1 & 1 & 1 & 1 \\ 1 & 1 & 1 & 1 & 1 & 1 & 1 & 1 & 1 & 1 & 1 & 1 & 1 & 1 & 1 \\ 1 & 1 & 1 & 1 & 1 & 1 & 1 & 1 & 1 & 1 & 1 & 1 & 1 & 1 & 1 \\ 1 & 1 & 1 & 1 & 1 & 1 & 1 & 1 & 1 & 1 & 1 & 1 & 1 & 1 & 1 \\ 1 & 1 & 1 & 1 & 1 & 1 & 1 & 1 & 1 & 1 & 1 & 1 & 1 & 1 & 1 \\ 0 & 1 & 1 & 1 & 1 & 1 & 1 & 1 & 1 & 1 & 1 & 1 & 1 & 1 & 0 \\ 0 & 0 & 1 & 1 & 1 & 1 & 1 & 1 & 1 & 1 & 1 & 1 & 1 & 0 & 0 \\ 0 & 0 & 0 & 1 & 1 & 1 & 1 & 1 & 1 & 1 & 1 & 1 & 0 & 0 & 0 \\ 0 & 0 & 0 & 0 & 1 & 1 & 1 & 1 & 1 & 1 & 1 & 1 & 0 & 0 & 0 \end{bmatrix} \quad (5-51)$$

The results of closing and opening with mask $M_{15 \times 15}$, followed by mask processing with the grey ROI image are shown in Figure 5-11.

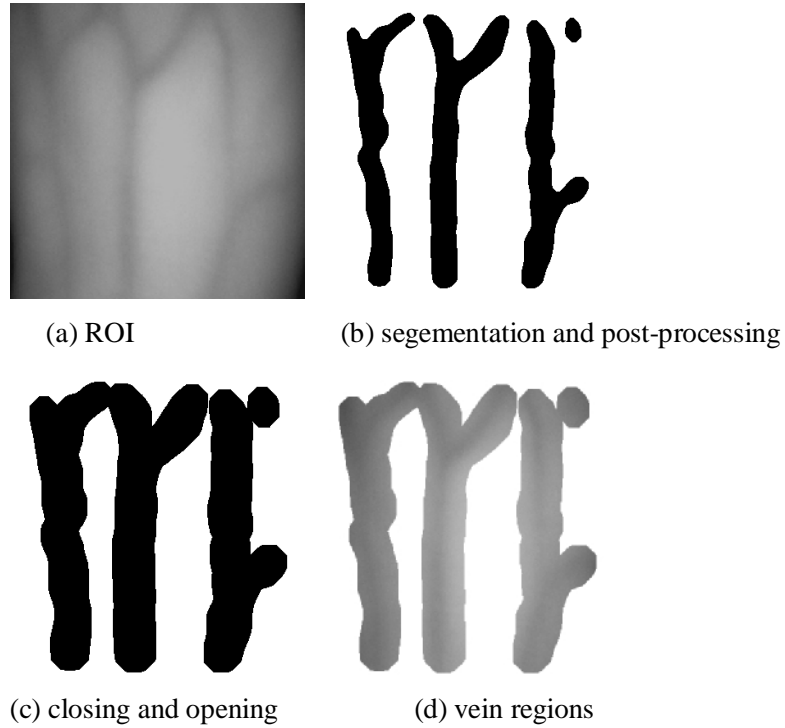


Figure 5-11 Results of vein regions extraction

Then RPLBP feature is extracted based on the image partitioned into 64 sub-images to form the fusion PLBP (FPLBP), which contains only texture features from the vein and nearby region and excludes texture features in the non-vein region.

In order to assess the impact made by FPLBP on image classification, the inter-class and intra-class distances are used. With the database containing 204 hand classes and 10 images for each hand class, if the feature vector of the n th image of the m th hand is represented as $V_{mn} (m = 1, 2, \dots, 204; n = 1, 2, \dots, 10)$, then the intra-class distance $IntraD$ and inter-class distance $InterD$ are defined as:

$$IntraD_{mn} = \|V_{mn} - C_m\| \quad (5-52)$$

$$InterD_{mn}(k) = \|V_{mn} - C_k\| \quad (k \neq m) \quad (5-53)$$

where, C_m denotes the average feature vector of the m th hand class:

$$C_m = \frac{1}{10} \sum_{n=1}^{10} V_{mn} \tag{5-54}$$

Figure 5-12 to Figure 5-15 shows the results of intra- and inter-class distances obtained for RPLBP and FPLBP, where the distributions are shown based on the distance interval set to 100.

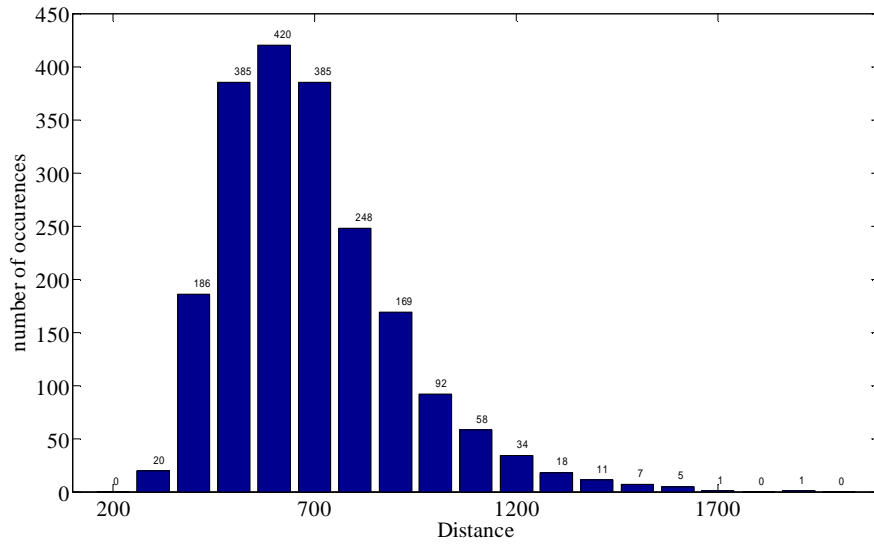


Figure 5-12 Intra-class distance of RPLBP

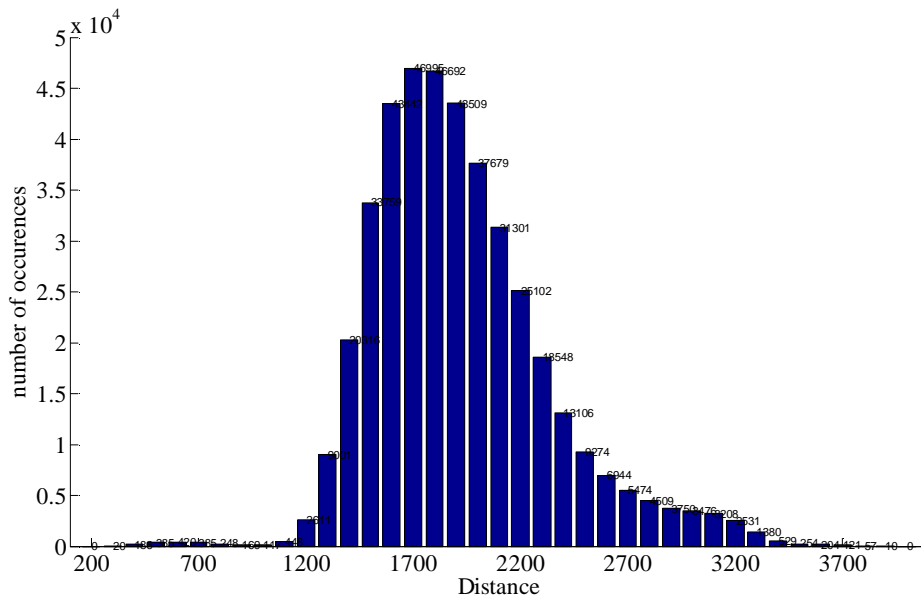


Figure 5-13 Inter-class distance of RPLBP

Chapter 5. Feature Extraction and Pattern Recognition

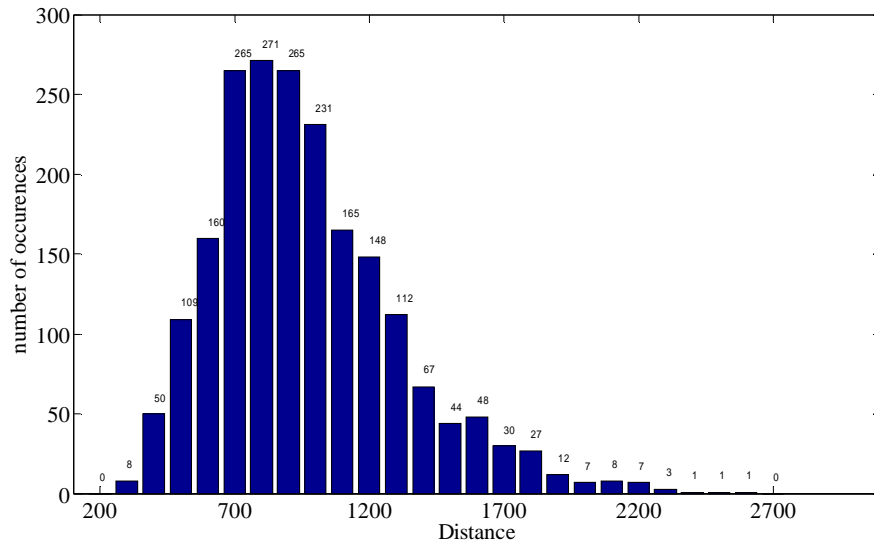


Figure 5-14 Intra-class distance of Fusion PLBP

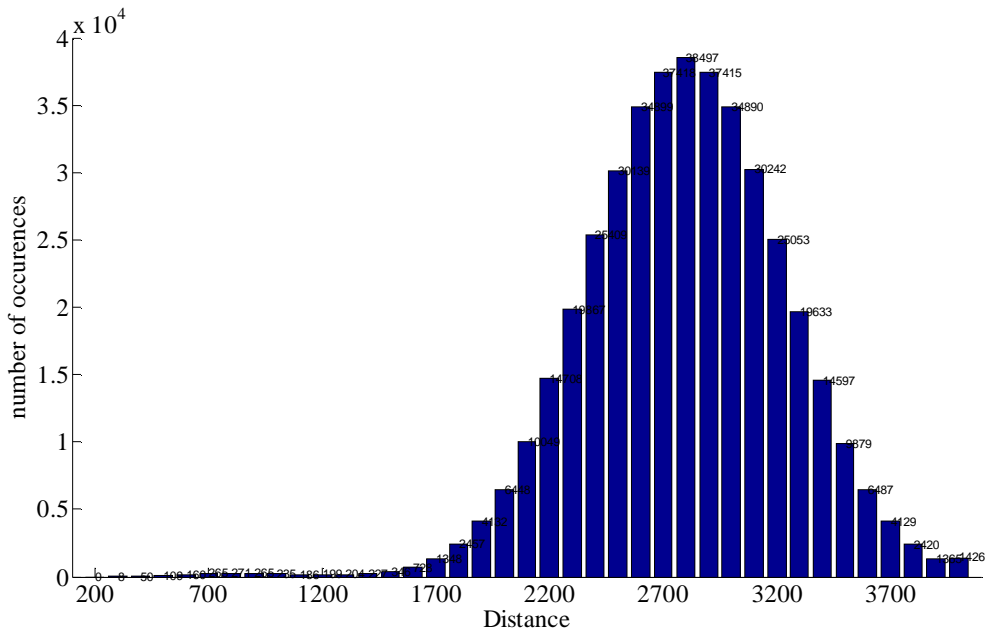


Figure 5-15 Inter-class distance of Fusion PLBP

Based on the intra-class distribution histograms shown in Figure 5-12 and Figure 5-14, RPLBP is seen to be better by providing more compact feature clusters, as evidenced by not only have a peak at smaller distance value but also narrower spread.

Chapter 5. Feature Extraction and Pattern Recognition

However, based on the inter-class distribution histograms shown in Figure 5-13 and Figure 5-15, WPLBP is seen to be better by providing larger distances between feature clusters, as evidenced by its peak and its spread at larger distance values.

In order to give a more quantitative measure of the intra-class and inter-class distributions, the distance ratio between them is used and can be expressed as:

$$R = \frac{InterD_{sta}}{IntraD_{sta}} \quad (5-55)$$

where $IntraD_{sta}$ and $InterD_{sta}$ are given by

$$D = \sum x_i \cdot p_i \quad (5-56)$$

and where x_i is the mid value of the i th distance interval, and p_i is the normalised distribution probability of the i th interval. Applying equations (5-55) and (5-56) to the distribution histograms shown in Figure 5-12 to Figure 5-15, the results are shown in Table 5-20.

Table 5-20 The ratio of inter-class distance to intra-class distance

	$IntraD_{sta}$	$InterD_{sta}$	Ratio of Inter/intra
RPLBP	687.4510	1919.6	2.7923
FPLBP	965.1961	2790.3	2.8909

From Table 5-20, although FPLBP is seen to increase the intra-class distance, it does increase significantly the inter-class distance, thereby producing a slightly larger ratio. With this larger ratio, the separability of vein pattern classes is improved. Using the experiment set-up same as that to achieve the highest recognition rate based on RPLBP described in section 5.4.4, the results shown in Table 5-21 confirm a better recognition performance of FPLBP compared with RPLBP.

Table 5-21 Comparison of FPLBP and RPLBP

Method	RR (%)
RPBLP	98.33
FPBLP	98.53

It is noteworthy to mention another approach attempted to increase the inter-class distance by introducing an error correction coding scheme (based on Bose-Chaudhvir-Hocquenghem coding and convolutional coding) to the RPLBP feature vectors to improve the recognition performance [Wang, Li, Shark *et al*, 2011].

5.5.2. Multi-scale Partition Local Binary Patterns (MPLBP)

Another possibility to enhance RPLBP is to combine texture features at different scales with suitable weights. There are two possible approaches to decompose an image into multiple scales with one in spatial domain and the other one in wavelet domain. While the wavelet domain approach has been attempted and is more computation intensive [Wang, Yan and Li, 2011], this section focuses on the spatial domain approach.

According to the results shown in Table 5-17, for different image sizes ($M=64, 128,$ and 256 which corresponding to three different scales in the spatial domain), the highest recognition rates are achieved with the numbers of sub-images N set to 32, 64 and 64 respectively, and the corresponding RPLBP feature vectors used are selected to form the multi-scale PLBP (MPLBP). Let $V_{64}, V_{128},$ and V_{256} denote the feature vectors of selected RPLBPs ($M=64, N=32; M=128, N=64; M=256, N=64$), as well as $w_1, w_2,$ and w_3 the corresponding weights for feature fusion. Then the MPBLP could be expressed by:

$$V_M = [w_1 V_{64} \quad w_2 V_{128} \quad w_3 V_{256}] \quad (5-57)$$

The simplest combination method is to set $w_1 = w_2 = w_3 = 1/3$, which means the

three selected RPLBPs have equal contribution in the classification process. However, this setting is unlikely to be optimum, and a suitable weight could be determined based on their relative recognition performance. According to Table 5-17, the recognition rates based on these RPLBPs are $r_1 = 96.96, r_2 = 97.84, r_3 = 98.33$, and substituting these values in the following equation

$$w_i = \frac{r_i}{r_1 + r_2 + r_3} \quad (i = 1, 2, 3) \tag{5-58}$$

gives $w_1 = 0.3308, w_2 = 0.3338$, and $w_3 = 0.3354$.

5.5.3. Experimental Results

A. MPLBP

Using the experiment set-up same as that to achieve the highest recognition rate based on RPLBP described in section 5.4.4, Table 5-22 compares the recognition results achieved by using MPLBP based on two different sets of weighting values with that achieved previously by RPLBP and FPBLP.

Table 5-22 Recognition rate (%) of improved PLBP

Method		RR (%)
MPLBP	$w_1=0.3308, w_2=0.3338, w_3=0.3354$	98.83
	$w_1=w_2=w_3=0.3333$	98.43
FPLBP		98.53
RPLBP		98.33

From Table 5-22, while MPLBP based on equal weight setting is seen to give a worse recognition performance than that of FPLBP, MPLBP can outperform FPLBP with a recognition rate reaching nearly 99% by using weights based on the relative importance of RPLBP texture feature in each image scale.

B. Classifier based experiments

With MPLBP found to offer the highest recognition rate, the experiment based on MPLBP was carried out to evaluate the impacts of four different classifiers (NN, KNN, MD and SVM) based two different distance metrics (Euclidean and Chi) on the recognition performance. The number of images used for training is set to 5 again, and they are selected as the 1st, 3rd, 5th, 7th and 9th images of the 10 images of each hand in the database. For KNN, the experiments were performed based on three different settings of the nearest points, and for SVM classifier the experiments were performed using the radial basis function with the kernel parameter $g=8.0$ and the penalty parameter for error $c=0.03125$, and the parameter settings are obtained through the cross validation process based on the training set [Chang and Lin, 2011]. The results are listed in Table 5-23.

Table 5-23 Recognition rate (%) of different classifiers (MPLBP)

Classifier		Distance	RR (%)
NN		2-norm	98.83
		Chi	97.94
KNN	$k=3$	2-norm	97.75
		Chi	97.94
	$k=5$	2-norm	96.27
		Chi	97.06
	$k=7$	2-norm	94.80
		Chi	95.00
MD		2-norm	95.20
		Chi	97.84
SVM ($c=0.03125, g=8.0$)		-	96.86

From the recognition results listed in Table 5-23, recommendations could be made on the use of the Chi square distance for classification based on KNN and MD classifiers, and the Euclidean distance for classification based on NN. The recognition performance of KNN is seen to increase as the number of the nearest points used for classification

Chapter 5. Feature Extraction and Pattern Recognition

decreases. The highest recognition rate of 98.83% is achieved by using the NN classifier based on Euclidean distance.

A recognition rate of more than 94% could be achieved no matter what classifier or distance is adopted, which reflects the distinctiveness among majority of the hand classes in the database. However, the database does contain some similar hand vein images causing misclassification. Two examples are shown in Figure 5-16 with the first mismatched pair corresponding to two right hand vein images from person No.6 and person No.74, and the second mismatched pair corresponding to two right hand vein images from person No.34 and person No.18. Possible improvement will be covered in the last chapter.

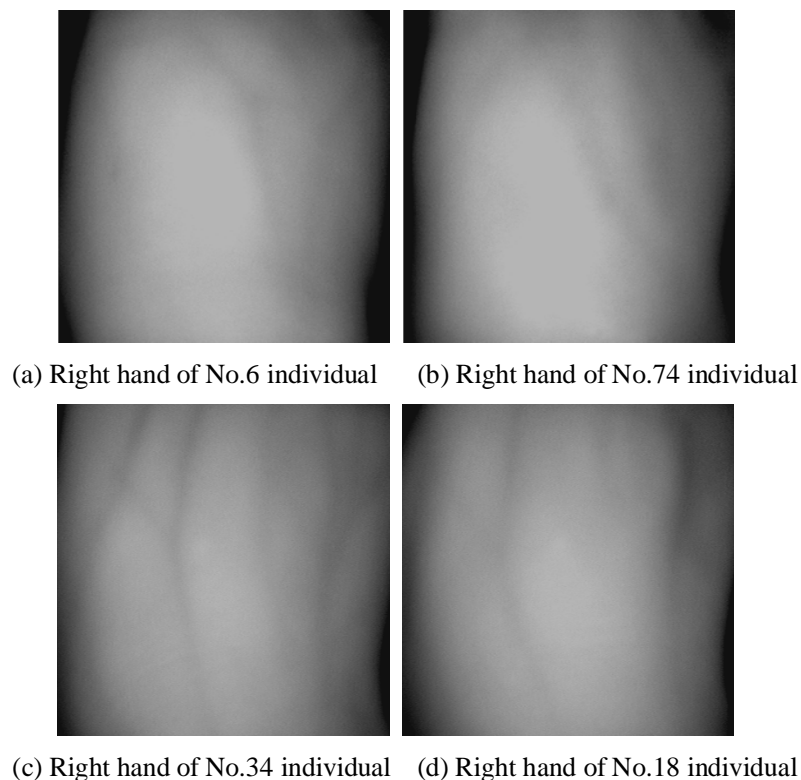


Figure 5-16 Distortion samples

5.6. Summary

In this chapter, some popular structure features are investigated. Furthermore, a novel feature PLBP for vein pattern extracted from grey-level images is proposed, and some improved PLBP methods are discussed.

For structure features, experiments of integral histogram, invariant moment methods and keypoints method are carried out. The recognition rate produced by using the integral histogram of columns is nearly double of that produced by the integral histogram of rows, and recognition performance decreases by adding the vein structure information derived from the integral histogram of rows to the vein structure information derived from the integral histogram of columns. For both Hu's and Zernike invariant moment methods, it is observed that increasing the number of moment orders does not increase the recognition performance. The recognition rates based on SIFT sets show that the matching strategy which combines the vector angles strategy and Euclidean distance strategy provides a higher correct recognition rate than the matching strategy based on only vector angles. The best classification accuracy is seen to be provided by the fused keypoint set, followed by the all keypoint set, with the lowest from the single keypoint set.

A novel texture feature PLBP is proposed based on LBP. It can be seen from the results, RPLBP performs better than CPLBP and the highest recognition rate occurs at $M=256$ pixels for both RPLBP and CPLBP. The most suitable number of sub-images is observed to be 64 for RPLBP and 16 for CPBLP when $M=256$ pixels. An improved PLBP feature WPLBP is seen to make a slight improvement in the performance compared with that achieved based on RPLBP.

Chapter 5. Feature Extraction and Pattern Recognition

Two multi-feature fusion methods are proposed and tested on the database, while MPLBP based on equal weight setting is seen to give a worse recognition performance than that of FPLBP, MPLBP can outperform FPLBP with a recognition rate reaching nearly 99% by using weights based on the relative importance of RPLBP texture feature in each image scale.

Furthermore, based on selected MPLBP, Euclidean and Chi square distances, NN, KNN, SD and SVM classifiers are investigated. Results show that recommendations could be made on the use of the Chi square distance for classification based on KNN and MD classifiers, and the Euclidean distance for classification based on NN. The recognition performance of KNN is seen to increase as the number of the nearest points used for classification decreases. The highest recognition rate of 98.83% is achieved by using the NN classifier based on Euclidean distance.

Chapter 6. SOFTWARE INTEGRATION WITH USER INTERFACE

6.1. Introduction

Based on the research described in the previous chapters, a hand-dorsa vein identification system with a simple user interface was built. This enables vein images to be captured under user control by using the NIR based acquisition device introduced in chapter 2, and the person to be recognised from the acquired hand-dorsa image by using some selected image processing algorithms based on the discussions in chapters 3 to 5, programmed in Visual C++ 6.0.

In this chapter, the overall system design is introduced, and then the implementation and the functions of the software are discussed.

6.2. Overall System Design

For an identification system, identification and registration are the two basic functions. The workflow of the system is shown in Figure 6-1. A hand-dorsa vein image is obtained by the capture device. Then it is sent to software on the PC through a USB capture card. After pre-processing and feature extraction, a PLBP feature vector is obtained. For registration, it will be saved in the feature database with corresponding user information, such as name, gender and age. For identification, by comparing it with the registered features in database, a result can be obtained.

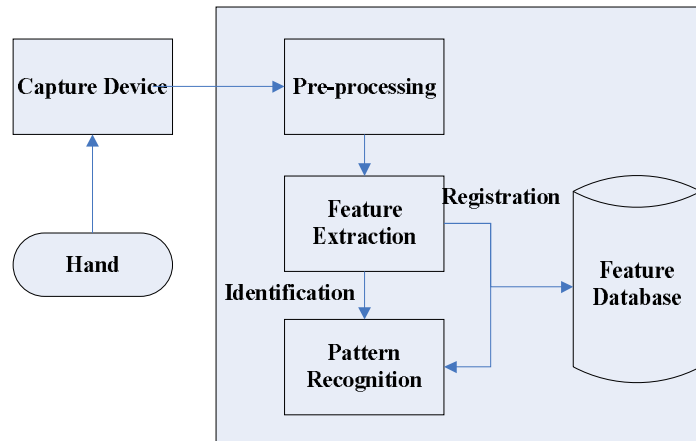


Figure 6-1 Workflow of vein identification system

Considering that some user information might have to be modified or deleted, these functions are added and integrated with registration to form an administrator mode. Identification mode will be the other mode for common users. A main interface is added to provide a switch between these two work modes.

6.3. Software Implementation

The hardware consists of two components: namely the NIR image acquisition device and a PC. The acquisition device is described detailed in chapter 2. The PC used in this work is HP Compaq DX7518 based on Intel(R) Core(TM)2 Quad CPU Q9400 running at 2.66GHz, with 3070MB RAM and operated using Windows XP Professional (5.1, Build 2600) Service Pack 3.

The software is developed with Visual C++ 6.0 based on the flowchart shown in Figure 6-2.

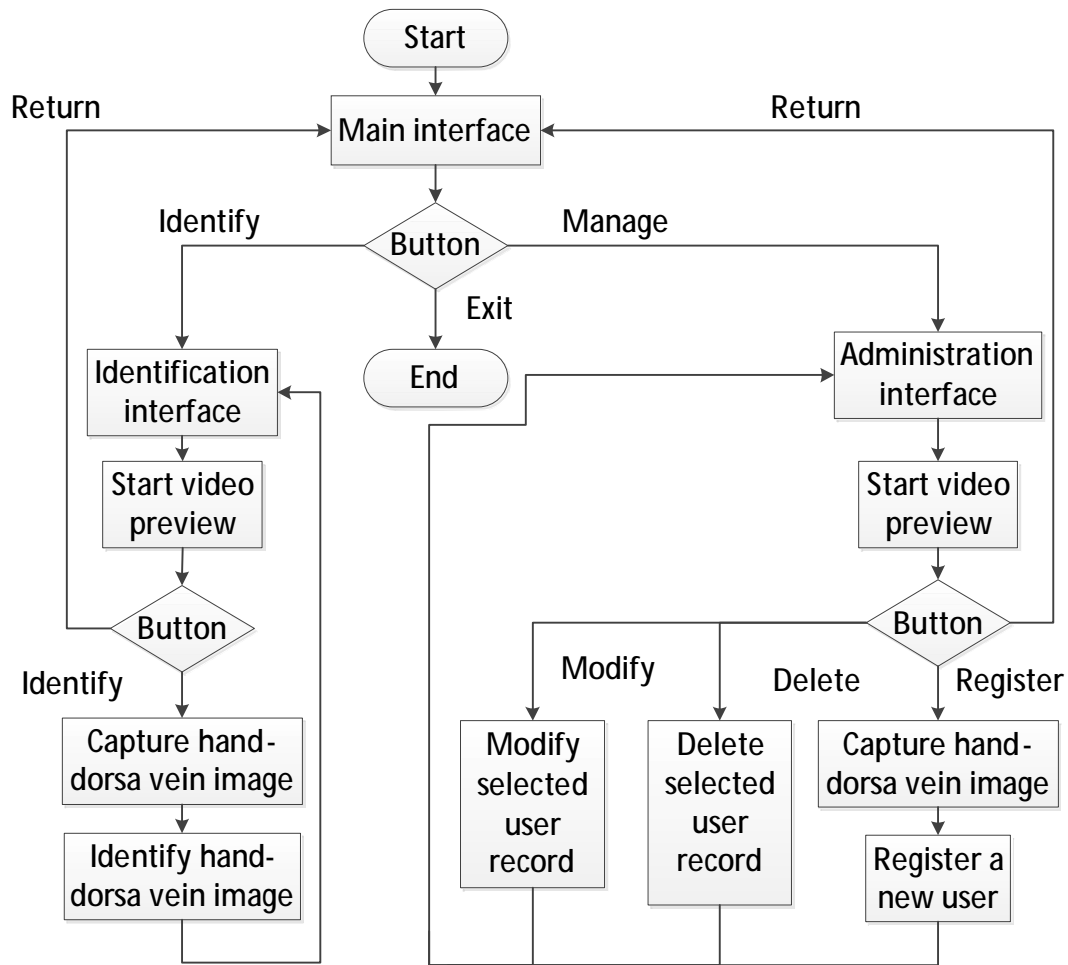


Figure 6-2 Flowchart of software

6.3.1. Hardware Interface

As discussed in section 2.2.2, a Mine 2860 USB capture card is adopted to connect the camera and PC. Moreover, it provides a SDK in Visual C++ 6.0, which is used in software to control the camera. A class CDevCtrl is designed based on SDK to control the camera through capture card. Some main functions are listed as follow:

A. Constructor

This function is used in the initialisations of the identification and administration interfaces, with the key parameters set in the following codes:

```
CDevCtrl::CDevCtrl()
{
    nCard = 0; // initialise capture card ID

    nTotalCard = 0; // initialise number of capture cards

    nWidth = 640; // width of image

    nHeight = 480; // height of image

    hWnd = NULL; // handle of video preview window

    OutputPin = 3; // source of input, 3 is for our device

    VideoStandard = PAL; // set video mode to PAL
}
```

B. Member functions

There are three member functions related to the control of the camera.

1) LONG CDevCtrl::InitCard(int nID, HWND hWnd, int nWidth, int nHeight)

This function is used to create a connection between capture card and a video preview window, where nID is the card ID, hWnd is the handle of video preview window, nWidth and nHeight denote image resolution.

2) LONG CDevCtrl::StartVideoPreview(int nID)

This function is used to start video preview for the capture card with an ID is nID.

3) LONG CDevCtrl::SaveBmpFile(int nID, char* strFileName)

This function is used to control the camera to capture an image through capture card

nID and save the image according to the file path and file name specified by strFileName.

C. Application codes

When the identification or administration interface is created, an object of class CDevCtrl is created as a member variable belonging to the class of identification or administration dialog by:

```
CDevCtrl nslot;
```

When nslot is created, some parameters of capture card are set by the constructor of CDevCtrl as discussed above. To start video preview, these codes are used:

```
nSlot.hWnd = m_aAnimate.m_hWnd; // get the handle of video preview window
```

```
nslot. InitCard(nID, hWnd, nWidth, nHeight);
```

```
nslot. StartVideoPreview(nID);
```

If image is needed to be captured, code as follows will be used:

```
nslot.SaveBmpFile(nID, strFileName);
```

6.3.2. Software Interface

According to the functions of the software, there are three interfaces including main interface, identification interface and administration interface.

1) Main interface



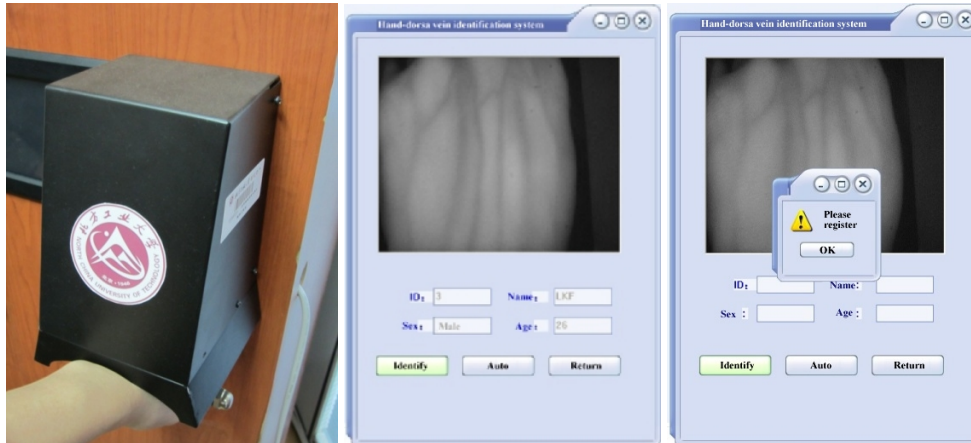
Figure 6-3 Main interface

Through the three buttons on the main interface, users could select the two modes of operations, namely, identification and administration, or system exit.

2) Identification interface

In this interface, users are required to press the identification button after the hand to be recognised is placed in a correct position by holding the handle that is fixed under the capture device box as shown in Figure 6-4(a). If the user has been registered in the database, the information, such as name, gender and age, will be displayed as shown in Figure 6-4(b). Otherwise, a dialog box with “Please register” will pop up as shown in Figure 6-4(c).

Chapter 6. Software Integration with User Interface



(a) Begin identification (b) Registered, response (c) Unregistered, response

Figure 6-4 Identification mode

3) Administration interface

This interface is divided into two parts. As shown in Figure 6-4, the left part of the screen provides the list of the registered users in the database, and the right part of the screen shows the hand-dorsa vein image and corresponding information of a new user or one selected from the list on the left. From the three buttons on the bottom right, the administrator could register a new user, modify or delete the information of the user selected from the list shown on the left.

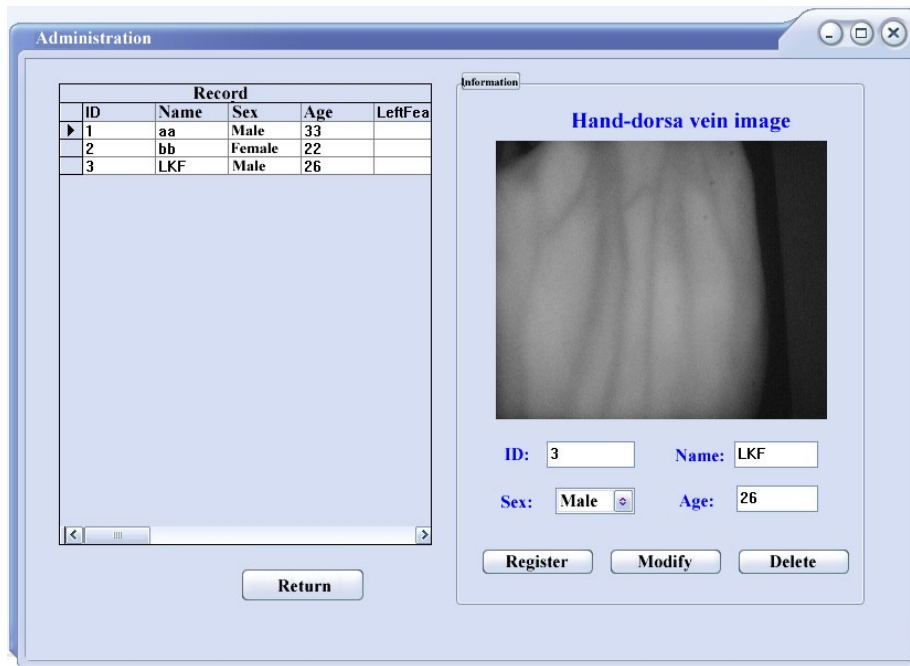


Figure 6-5 Administration interface

6.4. Summary

In this chapter, the workflow of hand-dorsa vein recognition system and the flow chart of software are described. The image capture device is connected to PC via a capture card and a class CDevCtrl is designed based on SDK to control the camera.

The software is developed with Visual C++ 6.0, which consists of the main interface to provide a selection of two operation modes, identification interface for hand-dorsa vein identification and administration interface for administer to register a new user, modify or delete the information of the registered user.

Chapter 7. CONCLUSIONS AND FUTURE WORK

7.1. Conclusions

Presented in this thesis are research and development of a complete biometric person identification system based on hand-dorsa vein images, from near-infrared imaging to pattern recognition.

The final hand vein image acquisition device developed features a simple imaging configuration to minimise hardware cost, which essentially consists of two LED arrays providing active NIR illumination and a relatively low-cost camera covering the central part of the dorsal hand. Furthermore, a handle is introduced to restrict hand posture, thereby simplifying image pre-processing without requiring sophisticated image alignment operations for recognition.

For comprehensive performance evaluation, a database of hand-dorsa vein images is created using the device implemented with capture software coded by Visual C++ 6.0. The database contains 2,040 images from 102 individuals in which 52 are female and 50 are male.

From the quantitative analysis of the images in the database, the image consistency of the database is considered to be good, as evidenced by the PSNR values greater than 32 dB based on the grey level deviation of each hand-dorsa vein image with respect to its group average. This justifies the use of simple image shearing correction for image

Chapter 7. Conclusions and Future Work

alignment, and the proposed geometrical pre-processing (image shearing correction and ROI extraction) yields further improvement in image consistency, as evidenced by a significant reduction in the number of images with low PSNR values (from 73 images to 15 images with PSNR lower than 32 dB).

From the quantitative analysis of image noise based on TV and performance evaluation of some commonly used filters, the improved Gaussian filter has been found to provide the best performance. For a typical hand-dorsa vein image, the improved Gaussian filter has been shown to give a smooth grey level profile with lowest local fluctuation and reduce the TV value by around 77%.

From the work conducted on image analysis and investigation on image pre-processing operations, the final image pre-processing system is proposed to consist of five stages, namely, image shearing correction, ROI extraction, grey level normalisation, improved Gaussian filter, and contrast limited adaptive histogram equalisation.

Comprehensive performance evaluation has been carried out for six different segmentation approaches based on a fixed threshold derived from the Otsu's method, adaptive thresholds using local mean and standard deviation (Threshold image, Niblack and improved Niblack), boundary characteristics, and adaptive threshold derived from the local mean and gradient information. From the evaluation, the gradient based segmentation approach is found to be particularly suitable for hand-dorsa vein images. Compared with other approaches, it yields the best vein patterns with least segmentation errors. This is due to the use of the gradient information to increase/decrease the threshold value derived from local mean to overcome the problems associated with under segmentation and over segmentation.

Chapter 7. Conclusions and Future Work

Two different feature types have been investigated in detail for hand-dorsa vein image recognition. One is based on structure features and the other is based on texture features. For structure features, a good recognition rate of at least 95% is shown to be achievable easily by using relative simple features derived from either the integral histogram of columns or lowest invariant moments. This could be attributed to thorough performance evaluation carried out to select the best approaches for the preceding stages. Furthermore, it is shown that the integral histogram of rows and higher moments are not important for hand-dorsa vein pattern recognition, as they not only produce lower recognition rates on their own, but also decrease the recognition rates if they are included in recognition together with the integral histogram of columns or lowest moments. Finally, among different structure features, the use of keypoints extracted based on SIFT is shown to be capable of providing the highest recognition rate up to around 98%, and this is achieved by the proposed fusion approach to combine multiple keypoint sets extracted from the training images and the matching strategy that combines the vector angles and Euclidean distance.

For texture features, several approaches based on LBP have been proposed for hand dorsa vein image recognition, which include CPLBP and RPLBP based on rotation invariant uniform binary patterns of non-overlapping rectangular and circular regions, WPLBP to introduce weights to RPLBP based on the relative importance of each binary patterns, FPLBP to control the contribution of RPLBP based on the vein structure information, and MPLBP to enhance RPLBP by combining texture features at different scales with suitable weights. From the comprehensive performance evaluation carried out, increasing recognition rates have been achieved by these proposed approaches based on

Chapter 7. Conclusions and Future Work

the NN classifier and Euclidean distance, with MPLBP found to produce the highest recognition performance at nearly 99%. The work includes investigation of different classifiers (NN, KNN, MD and SVM classifiers) and different distance measurement metrics (Euclidean distance and Chi square distance) for the case of MPLBP, and the NN classifier based on the Euclidean distance has been confirmed as the best.

Finally, the work has been concluded in a form of a complete biometric person identification system through hardware interface and software integration. A user interface has also been produced to enable not only identification of people but also administration of user information.

7.2. Original Contributions

The main original contributions from this study and development of the hand-dorsa vein identification system are summarised in the following sub-sections.

7.2.1. Image Acquisition and Database

A unique and low-cost NIR based hand-dorsa vein imaging system has been designed and implemented, which is capable of providing hand-dorsa vein images with sufficiently good quality and with relatively consistent hand postures. In particular, the image quality of the proposed image acquisition system is less affected by the surrounding visible light, compared with other similar imaging systems available. This is achieved through a more careful shape design of the covering box and a better handle position with respect to the covering box to ensure its lower open-end to be largely covered by the user hand during image acquisition. The author has worked as a member of the team in the development with responsibilities for manufacturing of the prototype device and development of the

image acquisition software.

A high quality database of hand-dorsa vein images has been created which is essential for algorithm performance evaluation and bench marking. This database is one of the largest in the world that is freely available to researchers working in the field of biometrics. The author has led the establishment of the database with a full spectrum of responsibilities, which included recruitment, management and organisation of work among team members, design of measurement protocol and procedure, supervision of image capture and quality of images captured.

7.2.2. Image Analysis and Pre-processing

A complete image pre-processing chain has been proposed, which consists of image shearing correction, ROI extraction, grey level normalisation, improved Gaussian filter, and contrast limited adaptive histogram equalisation. Each stage has been designed and developed through quantitative and qualitative performance evaluation against several other approaches. Particularly noteworthy work in this area includes the improvement of image consistency via relative simple geometrical pre-processing based on shearing correction and a centroid based ROI extraction method [Wang, Li, Cui *et al*, 2010]. No such computation efficient approach has been reported in literature and this is made possible by the design of the image capture device that has a handle to provide consistent hand-dorsa vein images with least geometrical variations.

A more complex geometrical pre-processing method based on hand boundary detection has also been investigated for correction of image rotation due to incorrect hand grasping [Cui, Wang and Li, 2010]. It has not been included in this report, because it is

not consistent with the images in the database.

7.2.3. Feature Extraction

For hand-dorsa vein image recognition based on structure features, a novel method is proposed based on keypoints extracted using SIFT with a fusion strategy to merge multiple sets of keypoints extracted from the training images and a matching strategy to remove many-to-one matches based on a combination of the vector angles and Euclidean distance. The proposed method has increased the recognition performance from around 95% to around 98%, compared with other structure features based on integral histograms and moments. This could be explained by the use of SIFT that enables classification to be less affected by imaging quality and variability, and the proposed fusion strategy that reduces information redundancies and improves the discrimination power [Wang, Fan, Liao *et al*, 2012].

For hand-dorsa vein image recognition based on texture features, the work has led to four approaches proposed based on LBP:

1) The PLBP feature is proposed based on LBP [Wang, Li and Cui, 2010] which enables a higher recognition rate compared with the traditional LBP approach by providing a more detailed representation of texture features based on non-overlapping regions.

2) Based on the relative importance of each texture (binary) pattern in their contribution to recognition, weights are introduced to form a WPLBP feature [Wang, Li, Shark *et al*, 2011], and found to result in a slight improvement in the recognition performance.

Chapter 7. Conclusions and Future Work

3) By utilising the vein structure pattern to control the contribution of RPLBP in recognition, a multi-feature fusion method (FPLBP) is proposed to increase the ratio of inter-class distance and intra-class distance, and this was found to further increase the recognition rate.

4) By combining texture features at different scales with suitable weights based on the relative importance of RPLBP texture feature in each image scale, MPLBP is proposed, and found to provide the highest recognition rate of nearly 99%. In this area of work, although a wavelet domain approach has also been investigated [Wang, Yan and Li, 2011], it has not been included in this report, because it is more computation intensive.

It is particularly noteworthy to point out that texture features based on LBP have not previously been applied to recognition of vein images, and the work reported in this thesis is considered to represent the most detailed investigation on the achievable recognition rates for LBP based classification of hand-dorsa vein images.

7.2.4. System Integration

A completed hand-dorsa vein pattern identification system has been implemented, including both hardware and software. Main interface, identification interface and administration interface provide functions for identification of people and administration of user information. All of these form an excellent basis for it to be developed into a successful commercial product.

7.3. Future Work

Further research work should be done in the following aspects:

- 1) The capture device could be improved. The handle and box could be improved

Chapter 7. Conclusions and Future Work

according to human engineering to make it more comfortable to use, and to reduce geometrical distortion of the vein images obtained. The factors influencing illumination, such as light intensity, distance and angle, should be investigated by further experiments to increase image contrast, thereby making hand-dorsa veins more visible in the images.

2) Although a database with 2040 images from 102 participants has been created, it is necessary to expand it, by including more hand vein images in order to facilitate more robust and accurate performance evaluation as well as different ethnic groups and different age groups to enable the study on the influence of race and age on recognition. It would also be interesting to include hand vein images acquired before and after consuming alcohol to study the influence of alcohol on recognition.

3) More efficient feature extraction and pattern recognition methods should be investigated to achieve higher recognition rate for the enlarged database. The work has shown the potential of multi-feature fusion features. Some more complicated classifiers, such as random tree and random forest might be more suitable.

Above all, hand-dorsa vein patterns have been shown to be an efficient and effective biometric feature for personal identification in this thesis. With a little more research, it should be possible to achieve 100% recognition rate.

REFERENCES

- Accute Optical Tecnology Co., L., *Bandpass Coating Filter*. http://www.accuteoptical.com/IR_Narrow_Banpass_Optical_Filter.shtml, 2012.
- Ahonen, T., Pietikainen, M., Hadid, A., and Maenpaa, T., *Face Recognition Based on the Appearance of Local Regions*. 17th International Conference on Pattern Recognition, 2004.
- Alper, G., *CCD vs. CMOS Image Sensors in Machine Vision Cameras*. <http://info.adimec.com/blogposts/bid/39656/CCD-vs-CMOS-Image-Sensors-in-Machine-Vision-Cameras>, 2011.
- Arce, G.R., *Nonlinear Signal Processing: A Statistical Approach*. 2005, New Jersey: Wiley.
- Badawi, A.M., *Hand Vein Biometric Verification Prototype: A Testing Performance and Patterns Similarity*. Proceedings of the 2006 International Conference on Image Processing, Computer Vision, and Pattern Recognition, 2006.
- BBC, *BBC Science:Human Body & Mind*. <http://www.bbc.co.uk/science/humanbody/>, 2012.
- Belkasim, S., Ahmadi, M., and Shridhar, M., *Efficient algorithm for the fast computation of zernike moments*. Journal of the Franklin Institute, 1996, 333(4), pp. 577-581.
- Biotech-Weblog, *Biometric Identification Using Subcutaneous Vein Patterns*. http://www.biotech-weblog.com/50226711/biometric_identification_using_subcutaneous_vein_patterns.php, 2005.
- Bremner, D., Demaine, E., Erickson, J., Iacono, J., Langerman, S., Morin, P., and Toussaint, G., *Output-sensitive algorithms for computing nearest-neighbor decision boundaries*. Discrete and Computational Geometry, 2005, 33(4), pp. 593-604.
- Brunelli, R. and Poggio, T., *Face Recognition: Features versus Templates*. IEEE Transaction on Pattern Analysis and Machine Intelligence, 1993, 15(10), pp. 1042-1052.
- Carmeliet, P., *Angiogenesis in life, disease and medicine*. Nature, 2005, 438, pp. 932-936.
- Carmeliet, P. and Jain, R.K., *Angiogenesis in cancer and other diseases*. Nature, 2000, 407, pp. 249-257.

- Carretero, O.A., *Vascular remodeling and the kallikrein-kinin system*. Journal of Clinacal Investigation, 2005, 115, pp. 588-591.
- Chang, C.-C. and Lin, C.-J., *LIBSVM: A library for support vector machines*. ACM Transactions on Intelligent Systems and Technology, 2011, 2(3).
- Chapran, J., *Biometric Writer Identification: Feature Analysis and Classification*. International Journal of Pattern Recognition & Artificial Intelligence, 2006, 20, pp. 483-503.
- Chen, W., Li, P., and Lu, G., *Study on Near infra-red Spectrum of Ischemic Cerebral Infarction*. Journal of Hubei College of Traditional Chinese Medicine, 2000, 3.
- Chitode, J.S., *Digital Communication*. 2008: Technical Publications.
- Choi, H.S., *Apparatus and method for identifying individuals through their subcutaneous vein patterns and integrated system using said apparatus and method*. BK, USPatent #6301375, United States, 2001.
- Clarke, R., *Human Identification in Information Systems: Management Challenges and Public Policy Issues Information*. Technology & People, 1994, 7, pp. 6-37.
- Cole, G.H.A. and Woolfson, M.M., *Planetary Science: The Science of Planets Around Stars (1st ed.)*. 2002: Institute of Physics Publishing.
- Conrad, M.C. and Green, H.D., *Hemodynamics of Large and Small Vessels in Peripheral Vascular Disease*. Circulation, 1964, 29, pp. 847-853.
- Cross, J.M. and Smith, C.L., *Thermographic imaging of the subcutaneous vascular network of the back of the hand for biometric identification*. Proceedings of IEEE 29th International Camahan Conference on Security Technology, 1995, pp. 20-35.
- Cui, J., Song, X., Chen, G., and Chen, D., *Feature Extraction and Matching of Vein Based on Geometrical Shape and Wavelet Moment*. Journal of Northeastern University(Natural Science), 2009, 30(9), pp. 1236-1240.
- Cui, J., Wang, Y., and Li, K., *DHV image registration using boundary optimisation*. 6th International Conference on Intelligent Computing (ICIC'10), 2010, pp. 499-506.
- D'Andrea, L.D., Del Gatto, A., Pedone, C., and Benedetti, E., *Peptide-based molecules in angiogenesis*. Chemical Biology & Drug Design, 2006, 67, pp. 115-126.
- Daugman, J., *The importance of being random: statistical principles of iris recognition*. Pattern Recognition and Image Analysis, 2003, 36(2), pp. 279-291.

- Daugman, J., *How iris recognition works*. IEEE Transactions on Circuits and Systems for Video Technology, 2004, 14 (1), pp. 21-30.
- Davies, E., *Machine Vision: Theory, Algorithms and Practicalities*. 2004: Academic Press.
- Delac, K. and Mislav, G., *A Survey of Biometric Recognition Methods*. 46th International Symposium Electronics in Marine, 2004, pp. 184-193.
- Ding, Y., Zhuang, D., and Wang, K., *A Study of Hand Vein Recognition Method*. Proceedings of the IEEE International Conference on Mechatronics & Automation, 2005, pp. 2106-2110.
- Dokoumetzidis, A. and Macheras, P., *A model for transport and dispersion in the circulatory system based on the vascular fractal tree*. Annals of Biomedical Engineering, 2003, 31, pp. 284-293.
- Duan, K. and Keerthi, S., *Which Is the Best Multiclass Svm Method? An Empirical Study*. Proceedings of the Sixth International Workshop on Multiple Classifier Systems, 2005, pp. 278-285.
- Eichmann, A., Yuan, L., Moyon, D., Lenoble, F., Pardanaud, L., and Breant, C., *Vascular development: from precursor cells to branched arterial and venous networks*. International Journal of Developmental Biology, 2005, 49, pp. 259-267.
- Faundez-Zanuy, M., *On-line signature recognition based on VQ-DTW*. Pattern Recognition and Image Analysis, 2007, 40(3), pp. 981-992.
- Fisher, R., Perkins, S., Walker, A., and Wolfart, E., *Classification*. <http://homepages.inf.ed.ac.uk/rbf/HIPR2/classify.htm>, 2003.
- Flusser, J., *On the Independence of Rotation Moment Invariants*. Pattern Recognition Letters, 2000, 33, pp. 1405-1410.
- Flusser, J. and Suk, T., *Rotation Moment Invariants for Recognition of Symmetric Objects*. IEEE Transactions on Image Processing, 2006, 15, pp. 3784-3790.
- Fujitsu, *Fujitsu Develops Technology for World's First Contactless Palm Vein Pattern Biometric Authentication System*. <http://www.fujitsu.com/global/news/pr/archives/month/2003/20030331-05.html>, 2003.
- Gabryśa, E., Rybaczuka, M., and Kędziab, A., *Fractal models of circulatory system. Symmetrical and asymmetrical approach comparison*. Chaos, Solitons & Fractals, 2005, 24(3), pp. 707-715.
- Galy, N., Charlot, B., and Courtois, B., *A Full Fingerprint Verification System for a Single-Line Sweep Sensor*. Ieee Sensors Journal, 2007, 7(7), pp. 1054-1065.

- Gamba, A., Ambrosi, D., Coniglio, A., deCandia, A., DiTalia, S., Giraud, E., Serini, G., Preziosi, L., and Bussolino, F., *Percolation, Morphogenesis, and Burgers Dynamics in Blood Vessels Formation*. Physical Review Letters, 2003, 90, pp. 118101-118101.
- Goldstein, A.J., Harmon, L.D., and Lesk, A.B., *Identification of human faces*. Proceedings of the Ieee, 1971, 59(5), pp. 748-760.
- Gray, H. and Standring, S., *Vascular Supply and Lymphatic Drainage*. Gray's Anatomy: the Anatomical Basis of Clinical Practice, 2008, pp. Figure 53.60
- Gutin, G., Yeo, A., and Zverovich, A., *Traveling salesman should not be greedy: domination analysis of greedy-type heuristics for the TSP*. Discrete Applied Mathematics, 2002, 117, pp. 81-86.
- Haddad, R.A., *A class of fast Gaussian binomial filters for speech and image processing*. IEEE Transactions on Signal Processing, 1991, 39(3), pp. 723-727.
- Haddadnia, J., Ahmadi, M., and Faez, K., *An efficient feature extraction method with pseudo-zernike moment in rbf neural network-based human face recognition system*. EURASIP Journal on Applied Signal Processing, 2003, pp. 890-901.
- He, Z., Tan, T., Sun, Z., and Qiu, X., *Boosting Ordinal Features for Accurate and Fast Iris Recognition*. Proceeding of the 26th IEEE Computer Society Conference on Computer Vision and Pattern Recognition, 2008, pp. 1-8.
- Hoeks, A.P.G. and deMay, J.G.R., *Vascular model and remodeling*. <http://www.onderzoekinformatie.nl/en/oi/nod/onderzoek/OND1288965/>, 2002.
- Hsu, C.W. and Lin, C.J., *A Comparison of Methods for Multiclass Support Vector Machines*. IEEE Transactions on Neural Networks, 2002, 13(2), pp. 415-425.
- Hu, M., *Visual Pattern Recognition by Moment Invariants*. IRE Transactions on Information Theory, 1962, IT-8, pp. 179-187.
- Huopio, S., *Biometric Identification*. In Seminar on Network Security: "Authorization and Access Control in Open Network Environment", 1998.
- Huynh-Thu, Q. and Ghanbari, M., *Scope of validity of PSNR in image/video quality assessment*. Electronics Letters, 2008, 44(13), pp. 800-801.
- Im, S.K., Park, H.M., Kim, Y.W., Han, S.C., Kim, S.W., and Kang, C.H., *A Biometric Identification System by Extracting Hand Vein Patterns*. Journal of the Korean Physical Society, 2000, 38(3), pp. 268-272.

- Ippolito, E., Peretti, G., Bellocchi, M., Farsetti, P., Tudisco, C., Caterini, R., and DeMartino, C., *Histology and ultrastructure of arteries, veins, and peripheral nerves during limb lengthening*. Clinical Orthopaedics and Related Research, 1994, pp. 54-62.
- ISO, *ISO/IEC19794-9 Biometric data interchange formats Part 9: Vascular image data*. 2011.
- ITU, *P.800.1 : Mean Opinion Score (MOS) terminology*. 2003.
- Jain, A.K., Bolle, R.M., and Pankati, S., *Biometrics: Personal Identification in Networked Society*. Dordrecht: Kluwer Academic Publishers, 1999a.
- Jain, A.K., Bolle, R.M., and Pankati, S., *Chapter 1 Introduction to Biometrics*. Biometrics - Personal Identification in Networked Society, Kluwer Academic Publishers Boston/Dordrecht/london, 1999b, pp. 1-41.
- Jain, A.K., Flynn, P.J., and Ross, A.A., *Handbook of Biometrics*. 2008: Springer.
- Jain, A.K., Hong, L., and Pankati, S., *Biometric Identification*. Communications of the ACM, 1999, 43(2), pp. 91-98.
- Jain, A.K. and Ross, A., *Introduction to Biometrics*. Handbook of Biometrics, 2008, pp. 1-22.
- Jain, L.C., Halici, U., Hayashi, I., Lee, S.B., and Tsutsui, S., *Chapter 1 Introduction to Fingerprint Recognition*. Intelligent Biometric Techniques in Fingerprint and Face Recognition, 1999, pp. 1-35.
- Johansson, G., *Visual perception of biological motion and a model for its analysis*. Perception and Psychophysics, 1973, 14, pp. 201-211.
- Johansson, G., *Visual motion perception*. Scientific American, 1975, pp. 76-88.
- Khairwa, A., Abhishek, K., Prakash, S., and Pratap, T., *A comprehensive study of various biometric identification techniques*. 2012 Third International Conference on Computing Communication & Networking Technologies (ICCCNT), 2012, pp. 1-6.
- Kirby, M. and Sirovich, L., *Application of the Karhunen-Loeve procedure for the characterization of human faces*. IEEE Transactions on Pattern Analysis and Machine Intelligence (PAMI), 1990, 12(1), pp. 103-108.
- Kumar, A. and Prathyusha, K.V., *Personal Authentication Using Hand Vein Triangulation and Knuckle Shape*. Ieee Transactions on Image Processing, 2009, 18(9), pp. 2127-2136.

- Lee, E.C., Lee, H.C., and Park, K.R., *Finger Vein Recognition Using Minutia-Based Alignment and Local Binary Pattern-Based Feature Extraction*. International Journal of Imaging Systems and Technology, 2009, 19(3), pp. 179-186.
- Lehmann, E. and Casella, G., *Theory of Point Estimation (2nd ed.)*. 1998, New York: Springer.
- Lin, C. and Fan, K., *Biometric verification using thermal images of palm-dorsa vein patterns*. IEEE Transactions on Circuits and Systems for Video Technology, 2004, 14(2), pp. 199-213.
- Lin, X., Zhuang, B., Su, X., Zhou, Y., and Bao, G., *Measurement and matching of human vein pattern characteristics*. Journal of Tsinghua University (Science & Technology), 2003, 43(2), pp. 164-167.
- Liu, Q., Wu, C., Pan, S., and Pan, X.L., *An Edge-Preserving Image Filter*. Microcomputer Information, 2007, 9.
- Liu, T., Wang, Y., Li, X., Jiang, J., and Zhou, S., *Biometric Recognition System Based on Hand Vein Pattern*. Acta Optica Sinica, 2009, 29(12), pp. 3339-3343.
- Liu, X., Liu, Z., Gong, P., and Zhou, P., *Study on the Recognition of Dorsal Hand Vein Pattern*. Journal of Natural Science of Hunan Normal University, 2009, 32(1), pp. 32-35.
- Liu, X., Shen, S., and Zheng, M., *Boundary reserved method on image denoising*. Application of Electronic Technique, 2000, 11, pp. 15-17.
- Lowe, D.G., *Object recognition from local scale-invariant features*. Proceedings of the Seventh IEEE International Conference on Computer Vision, 1999, 2, pp. 1150-1157.
- Lowe, D.G., *Distinctive Image Features from Scale-Invariant Keypoints*. International Journal of Computer Vision, 2004, 60(2), pp. 91-110.
- Mainguest, J.-F., *Biometrics-Vein, Vascular pattern* <http://fingerchip.pagesperso-orange.fr/biometrics/types/vein.htm#VeinID>, 2012.
- Mandelbrot, B.B., *The Fractal Geometry of Nature*. 1983, Henry Holt and Company.
- Marxen, M. and Henkelman, R.M., *Branching tree model with fractal vascular resistance explains fractal perfusion heterogeneity*. American Journal of Physiology Heart Circulatory Physiology, 2003, 284, pp. H1848-1857.
- McGeer, T., *Passive walking with knees*. IEEE International conference on Robotics and Automation, 1990, pp. 1640-1645.

- Michael, G., Connie, T., Hoe, L., and Jin, A., *Design and implementation of a contactless palm vein recognition system*. Proceedings of the 2010 Symposium on Information and Communication Technology, 2010, pp. 92-99.
- Niblack, W., *An Introduction to Image Processing*. Prentice-Hall, 1986, pp. 115-116.
- Ningbo-Website, *Safety Inspection of Softball World Championships Adopted High-tech*. <http://www.cnnb.com.cn/new-gb/xwzxzt/system/2006/09/02/005170842.shtml>, 2007.
- North, D.O., *An Analysis of the factors which determine signal/noise discrimination in pulsed-carrier systems*. Proceedings of the IEEE, 1963, 51(7), pp. 1016-1027.
- NSTC, *Biometrics History*. <http://www.biometrics.gov>, 2006a.
- NSTC, *Dynamic Signature*. <http://www.biometrics.gov>, 2006b.
- NSTC, *Face Recognition*. <http://www.biometrics.gov>, 2006c.
- NSTC, *Fingerprint Recognition*. <http://www.biometrics.gov>, 2006d.
- NSTC, *Iris Recognition*. <http://www.biometrics.gov>, 2006e.
- Ojala, T., Pietikäinen, M., and Mäenpää, T., *Multiresolution Gray-Scale and Rotation Invariant Texture Classification with Local Binary Patterns*. Ieee Transactions on Pattern Analysis and Machine Intelligence, 2002, 24(7).
- Otsu, N., *A threshold selection method from gray-level histograms*. IEEE Transaction on Systems, Man and Cybernetics, 1979, 9(9), pp. 62-66.
- Pascual, J.E.S., Uriarte-Antonio, J., Sanchez-Reillo, R., and Lorenz, M.G., *Capturing hand or wrist vein images for biometric authentication using low-cost devices*. Proceedings of the 2010 Sixth International Conference on Intelligent Information Hiding and Multimedia Signal Processing, 2010, pp. 318-322.
- PENTAX Precision Co., L., *Pentax for FA & Machine Vision Lenses*. 2012.
- Pizer, S.M., Amburn, E.P., Austin, J.D., R.Cromartie, Geselowitz, A., Greer, T., Romeny, B.H., Zimmerman, J.B., and Zuiderveld, K., *Adaptive Histogram Equalization and Its Variations*. Computer Vision, Graphics, and Image Processing, 1987, 39 pp. 355-368.
- Press, W.H., Teukolsky, S.A., Vetterling, W.T., and Flannery, B.P., *Section 16.5: Support Vector Machines*. Numerical Recipes: The Art of Scientific Computing (3rd ed.), 2007, New York: Cambridge University Press.

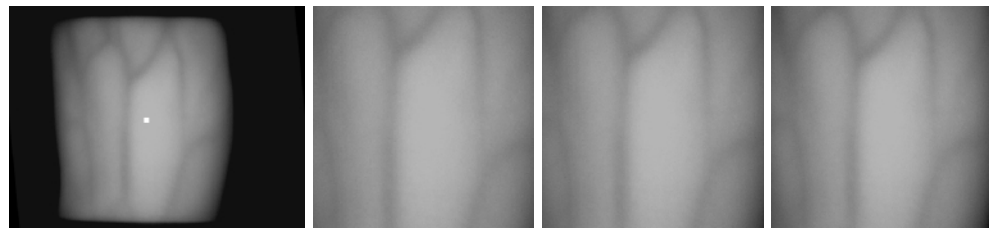
- Raghavendra, R., Imran, M., Rao, A., and Kumar, G.H., *Multimodal biometrics: Analysis of handvein & palmprint combination used for person verification*. International Conference on Emerging Trends in Engineering & Technology, 2010, pp. 526 - 530.
- Riggs, B.L., Khosla, S., and Melton, L.J.I., *The assembly of the adult skeleton during growth and maturation: implications for senile osteoporosis*. Journal of Clinical Investigation, 1999, 104, pp. 671-672.
- Risler, N.R., Cruzado, M.C., and Miatello, R.M., *Vascular remodeling in experimental hypertension*. Scientific World Journal, 2005, 5, pp. 959-971.
- Rubins, A., *Aging Process: Part X- The Skin, The Skeleton and The Brain*. <http://www.therubins.com/aging/proc10.htm>, 2012.
- Sanchez-Reillo, R., Fernandez-Saavedra, B., Liu-Jimenez, J., and Sanchez-Avila, C., *Vascular biometric systems and their security evaluation*. 41st Annual IEEE International Carnahan Conference on Security Technology, 2007, pp. 44-51.
- Sauvola, J. and PietikaKinen, M., *Adaptive document image binarization*. Pattern Recognition and Image Analysis, 2000, 33, pp. 225-236.
- Schreiner, W., Karch, R., Neumann, M., Neumann, F., Roedler, S.M., and Heinze, G., *Heterogeneous perfusion is a consequence of uniform shear stress in optimized arterial tree models*. Journal of Theoretical Biology, 2003, 220, pp. 285-301.
- Serra, J., *Image Analysis and Mathematical Morphology*. 1983: Academic Press.
- Shahin, M., Badawi, A., and Kamel, M., *Biometric Authentication Using Fast Correlation of Near Infrared Hand Vein Patterns*. International Journal of Biological and Life Sciences, 2006, 2(3), pp. 141-148.
- Shenzhen Mine Technology Co., L., *MINE VCap2860 (USB2.0 Video Capture Box)*. <http://www.mine.com.cn/asp-bin/EN/?page=5&class=110&id=134>, 2013.
- Shimizu, K., *Optical trans-body imaging: feasibility of non-invasion CT and functional imaging of living body*. Japanese Journal of Medicine Philosophica, 1992, 11, pp. 620-629.
- Shimizu, K. and Yamamoto, K., *Imaging of physiological functions by laser transillumination*. OSA TOPS on Advances Optical Imaging and Photom Migration, 1996, 2, pp. 348-352.
- Smith, W., *Modern Optical Engineering (4th ed.)*. 2007: McGraw-Hill Professional.

- Tanaka, T. and Kubo, N., *Biometric authentication by hand vein patterns*. Proc. SICE Annu. Conf., Yokohama, Japan, 2004, pp. 249-253.
- Teh, C.H. and Chin, R., *On image analysis by the methods of moments*. Ieee Transactions on Pattern Analysis and Machine Intelligence, 1998, 10(4), pp. 496-513.
- Vaseghi, S.V., *Advanced Digital Signal Processing and Noise Reduction (4th ed.)*. 2008: Wiley.
- Wang, K., Guo, Q., Zhuang, D., Li, Z., and Chu, H., *The Study of Hand Vein Image Processing Method*. Proceedings of the 6th World Congress on Intelligent Control and Automation, 2006, pp. 10197-10201.
- Wang, K., Zhang, Y., Yuan, Z., and Zhuang, D., *Hand vein recognition based on multi supplemental features of multi-classifier fusion decision*. Proc. IEEE Intl. Conf. Mechatronics Automation, Luoyang, China, 2006, pp. 1790-1795.
- Wang, L. and Leedham, G., *A thermal hand-vein pattern verification system*. Pattern Recognition and Image Analysis, 2005, 3687, pp. 58-65.
- Wang, L. and Leedham, G., *Near- and far-infrared imaging for vein pattern biometrics*. Proceedings of IEEE International Conference on Video Signal Based Surveillance, 2006, pp. 52-57.
- Wang, L., Leedham, G., and Choa, D.S.Y., *Minutiae feature analysis for infrared hand vein pattern biometrics*. Pattern Recognition, 2008, 41(3), pp. 920-929.
- Wang, Y., Fan, Y., Liao, W., Li, K., Shark, L., and Varley, M., *Hand Vein Recognition Based on Multiple Keypoints Sets*. International Conference on Biometrics (ICB 2012), 2012, pp. 367-371.
- Wang, Y., Li, K., and Cui, J., *Hand-dorsa Vein Recognition Based on Partition Local Binary Pattern*. 10th International Conference on Signal Processing (ICSP'10), 2010, pp. 1671-1674.
- Wang, Y., Li, K., Cui, J., Shark, L., and Varley, M., *Study of Hand-dorsa Vein Recognition*. 6th International Conference on Intelligent Computing (ICIC'10), 2010, pp. 490-498.
- Wang, Y., Li, K., Shark, L., and Varley, M., *Hand-dorsa Vein Recognition Based on Coded and Weighted Partition Local Binary Patterns*. International Conference on Hand-based Biometrics (ICHB2011), 2011, pp. 253-258.

- Wang, Y. and Wang, H., *Gradient Based Image Segmentation for Vein Pattern*. Fourth International Conference on Computer Sciences and Convergence Information Technology, 2009, pp. 1614-1618.
- Wang, Y., Yan, Q., and Li, K., *Hand vein recognition based on multi-scale LBP and wavelet*. Proceedings of 2011 International Conference on Wavelet Analysis and Pattern Recognition (ICWAPR 2011), 2011, pp. 214-218.
- Watec Co., L., *CCD Camera WAT-902B Operation Manual*. 2010.
- West, G.B., Brown, J.H., and Enquist, B.J., *A general model for the origin of allometric scaling laws in biology*. Science, 1997, 276, pp. 122-126.
- Wiener, N.N.Y.W., *Extrapolation, Interpolation, and Smoothing of Stationary Time Series*. 1949, New York: Wiley.
- X. Wu, E.G., Tang, Y., and Wang, K., *A novel biometric system based on hand vein*. Fifth International Conference on Frontier of Computer Science and Technology, 2010, pp. 522 -526.
- Yang, J., Shi, Y., and Yang, J., *Finger-vein recognition based on a bank of gabor filters*. Computer Vision - ACCV 2009, ser. Lecture Notes in Computer Science, 2010, 5994, pp. 374-383.
- Yang, J., Yang, J., Zhang, D., and Lu, J., *Feature Fusion: Parallel Strategy VS. Serial Strategy*. Pattern Recognition, 2003, 36, pp. 1369 - 1381.
- Zamir, M., *On fractal properties of arterial trees*. Journal of Theoretical Biology, 1999, 197, pp. 517-526.
- Zhang, D., *Automated Biometrics: Technology and Systems*. 2000, Norwell, Massachusetts, USA: Kluwer.
- Zhao, S., Wang, Y.D., and Wang, Y.H., *Biometric identification based on low-quality hand vein pattern images*. Proceedings of 2008 International Conference on Machine Learning and Cybernetics, 2008, 1(7), pp. 1172-1177.
- Zhou, B., Lin, X., and Jia, H., *Application of Multiresolutional Filter On Feature Extraction of Palm-Dorsa Vein Patterns*. Journal of Computer-Aided Design & Computer Graphics, 2006, 18(1), pp. 41-45.

Appendix A. RESULTS OF ROI EXTRACTION

This appendix gives the results of ROI extraction with R ranging from 300 to 420. 25 of all 102 individuals are listed, including left and right hand for each one.

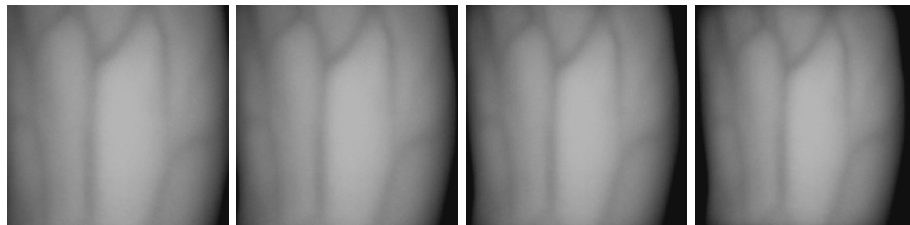


(a) Original

(b) $R=300$

(c) $R=320$

(d) $R=340$



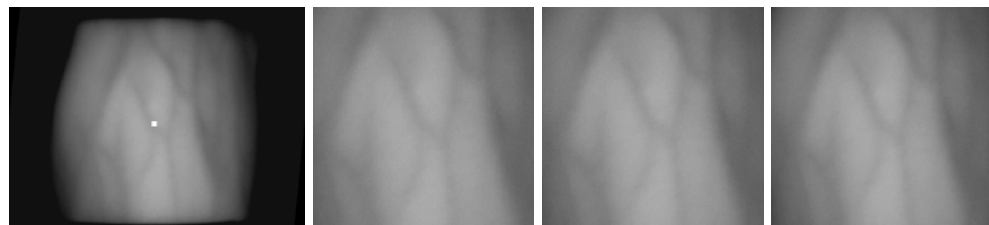
(e) $R=360$

(f) $R=380$

(g) $R=400$

(h) $R=420$

(1) Left hand of No.1 individual

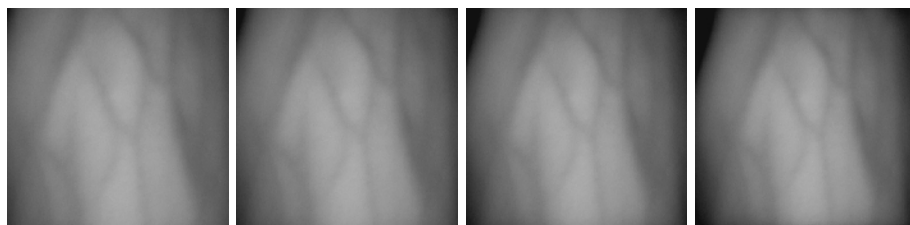


(a) Original

(b) $R=300$

(c) $R=320$

(d) $R=340$



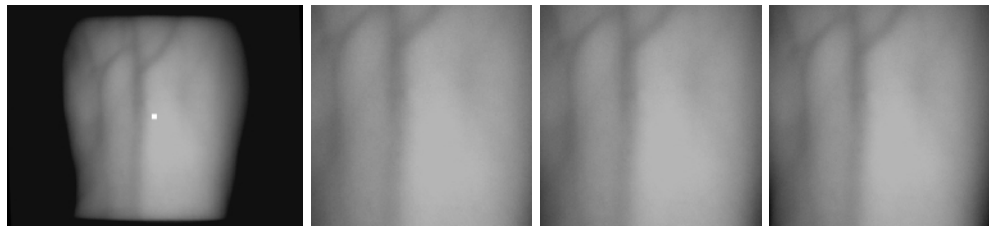
(e) $R=360$

(f) $R=380$

(g) $R=400$

(h) $R=420$

(2) Right hand of No.1 individual

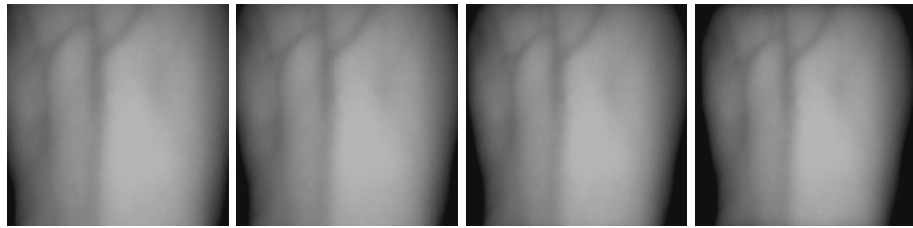


(a) Original

(b) R=300

(c) R=320

(d) R=340



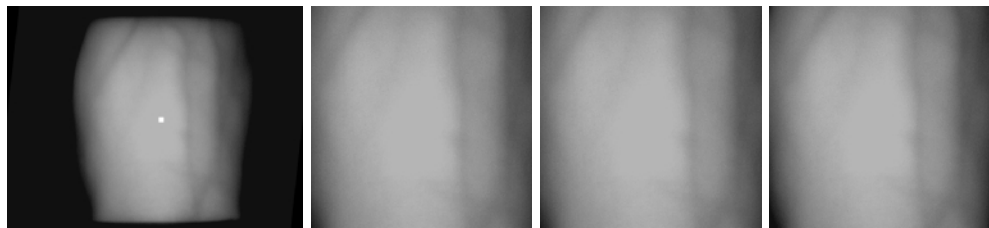
(e) R=360

(f) R=380

(g) R=400

(h) R=420

(3) Left hand of No.2 individual

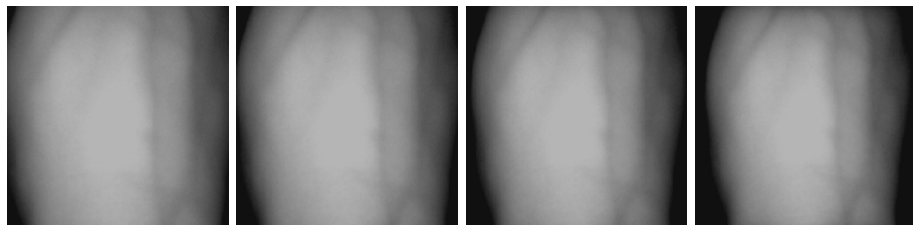


(a) Original

(b) R=300

(c) R=320

(d) R=340



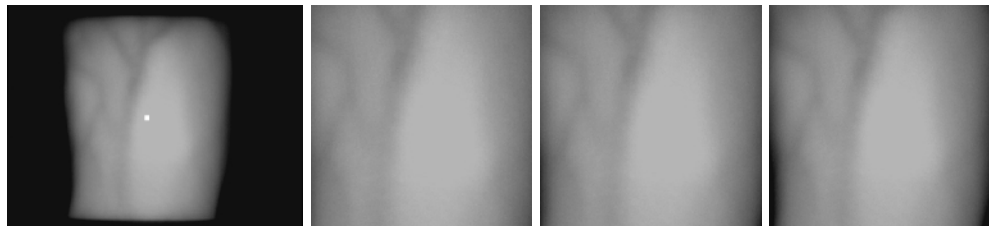
(e) R=360

(f) R=380

(g) R=400

(h) R=420

(4) Right hand of No.2 individual

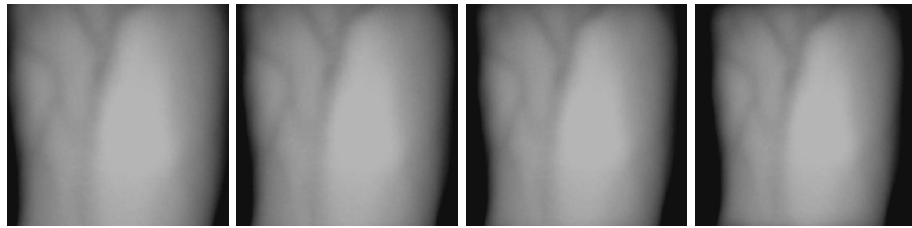


(a) Original

(b) R=300

(c) R=320

(d) R=340



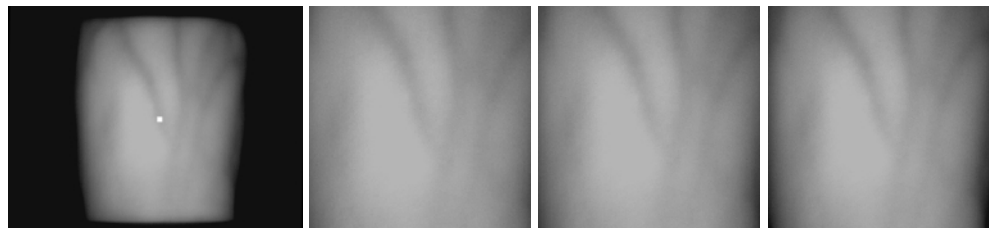
(e) R=360

(f) R=380

(g) R=400

(h) R=420

(5) Left hand of No.3 individual

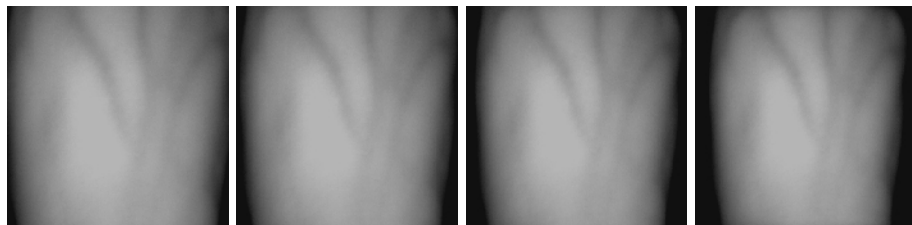


(a) Original

(b) R=300

(c) R=320

(d) R=340



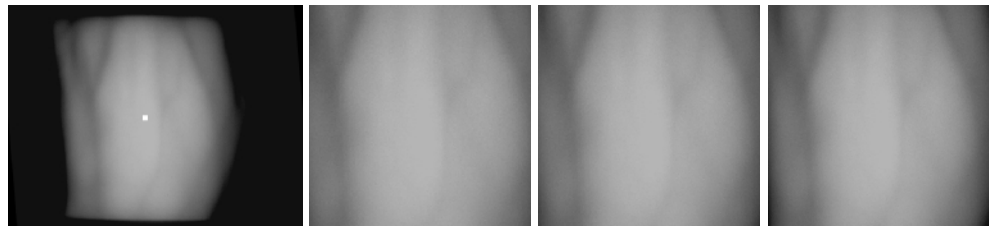
(e) R=360

(f) R=380

(g) R=400

(h) R=420

(6) Right hand of No.3 individual

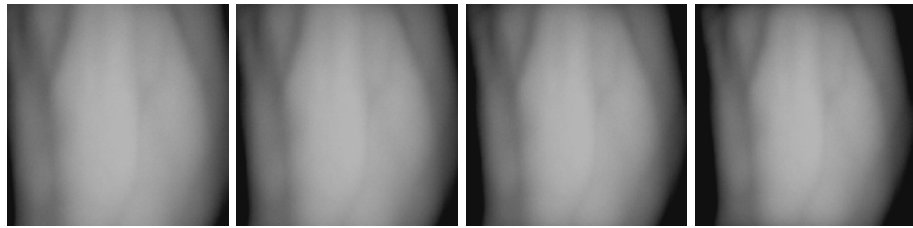


(a) Original

(b) R=300

(c) R=320

(d) R=340



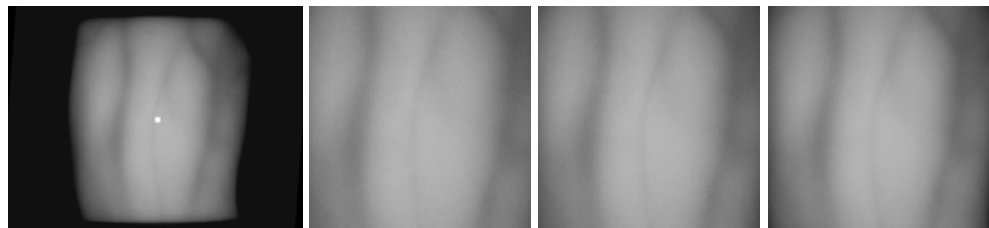
(e) R=360

(f) R=380

(g) R=400

(h) R=420

(7) Left hand of No.3 individual

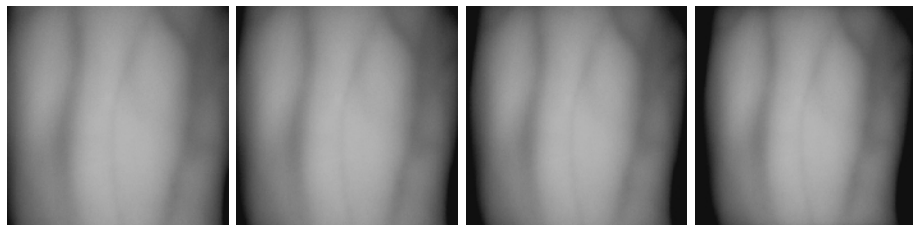


(a) Original

(b) R=300

(c) R=320

(d) R=340



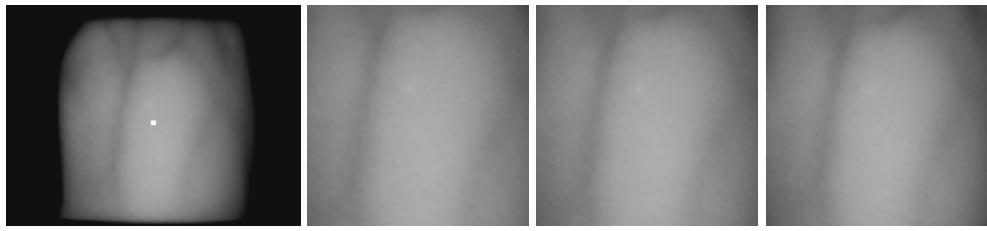
(e) R=360

(f) R=380

(g) R=400

(h) R=420

(8) Right hand of No.4 individual

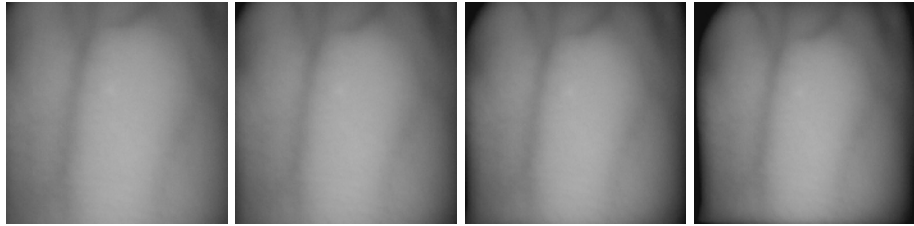


(a) Original

(b) R=300

(c) R=320

(d) R=340



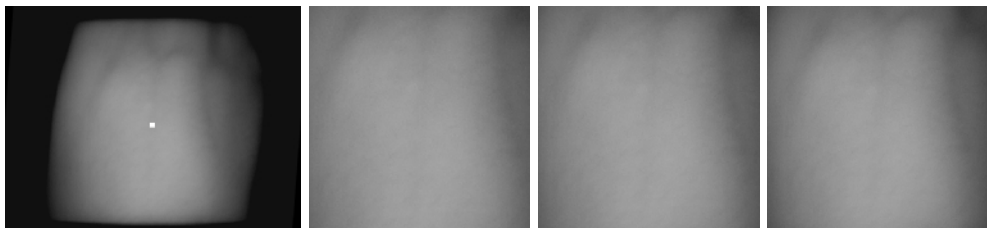
(e) R=360

(f) R=380

(g) R=400

(h) R=420

(7) Left hand of No.5 individual

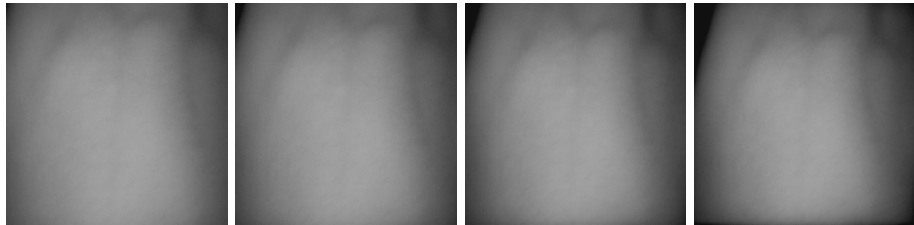


(a) Original

(b) R=300

(c) R=320

(d) R=340



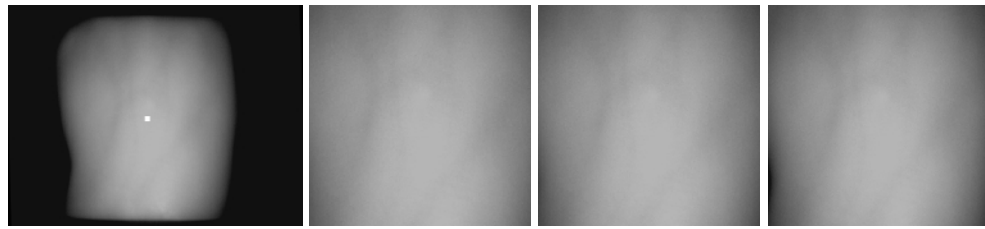
(e) R=360

(f) R=380

(g) R=400

(h) R=420

(10) Right hand of No.5 individual



(a) Original

(b) R=300

(c) R=320

(d) R=340



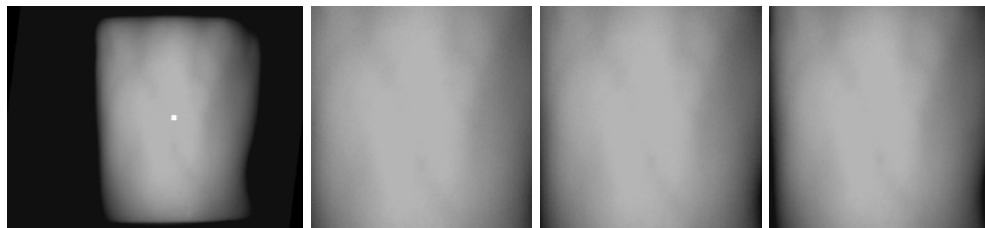
(e) R=360

(f) R=380

(g) R=400

(h) R=420

(11) Left hand of No.6 individual

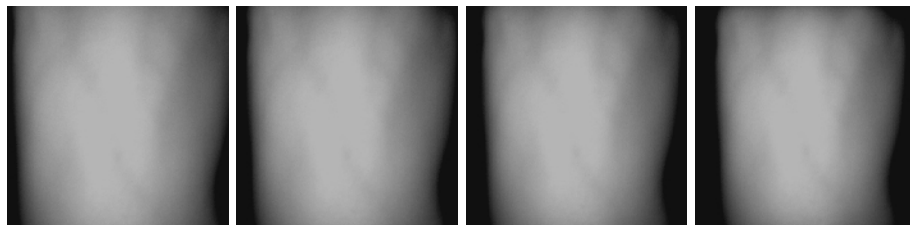


(a) Original

(b) R=300

(c) R=320

(d) R=340



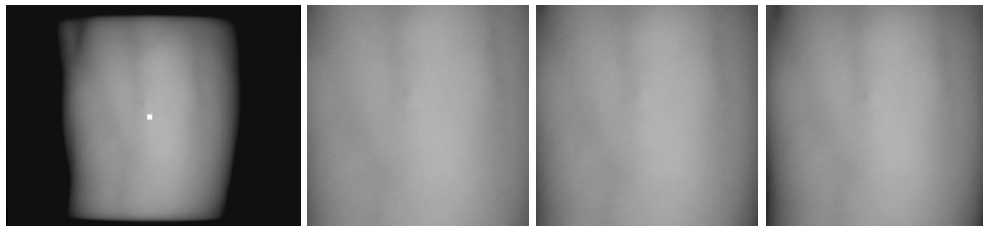
(e) R=360

(f) R=380

(g) R=400

(h) R=420

(12) Right hand of No.6 individual

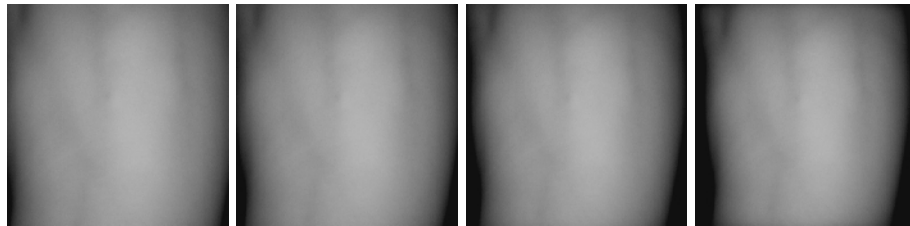


(a) Original

(b) R=300

(c) R=320

(d) R=340



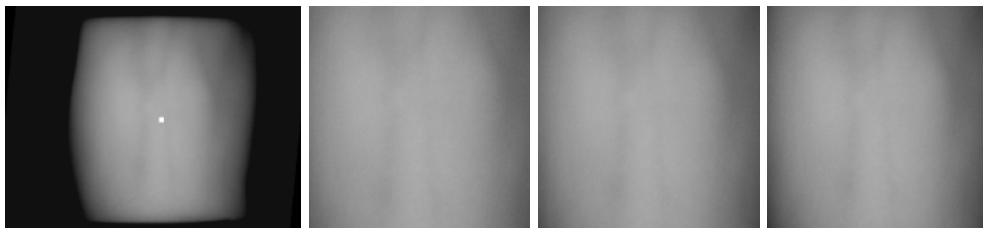
(e) R=360

(f) R=380

(g) R=400

(h) R=420

(13) Left hand of No.7 individual

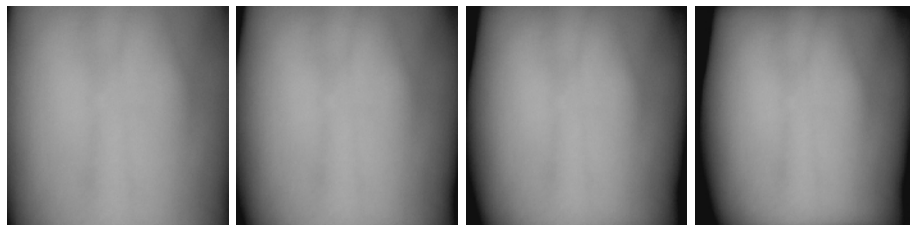


(a) Original

(b) R=300

(c) R=320

(d) R=340



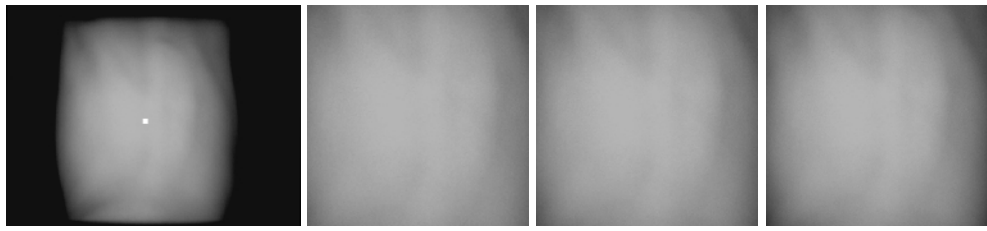
(e) R=360

(f) R=380

(g) R=400

(h) R=420

(14) Right hand of No.7 individual

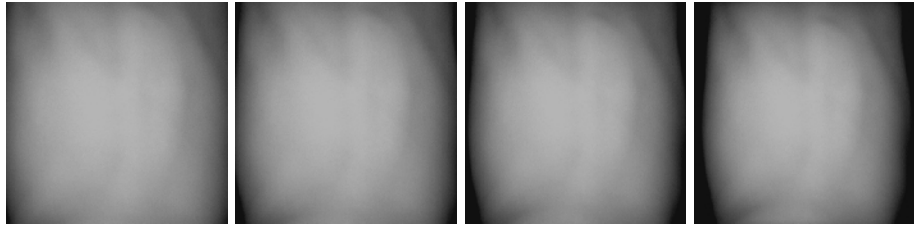


(a) Original

(b) R=300

(c) R=320

(d) R=340



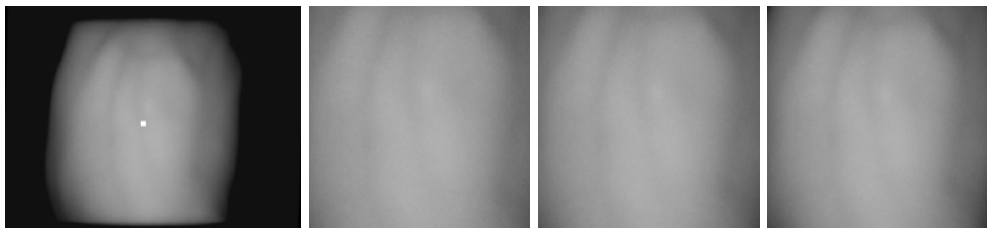
(e) R=360

(f) R=380

(g) R=400

(h) R=420

(15) Left hand of No.8 individual



(a) Original

(b) R=300

(c) R=320

(d) R=340



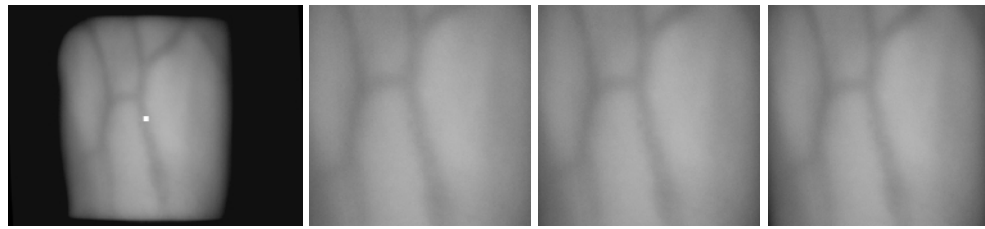
(e) R=360

(f) R=380

(g) R=400

(h) R=420

(16) Right hand of No.8 individual

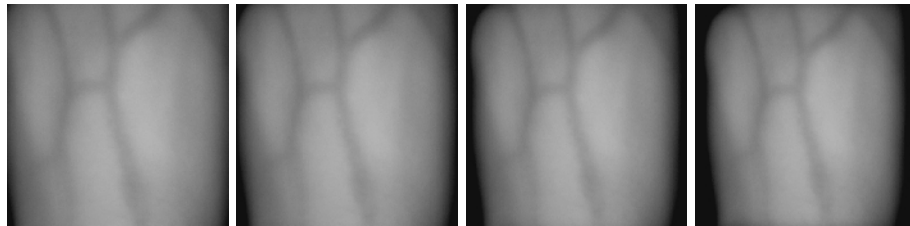


(a) Original

(b) R=300

(c) R=320

(d) R=340



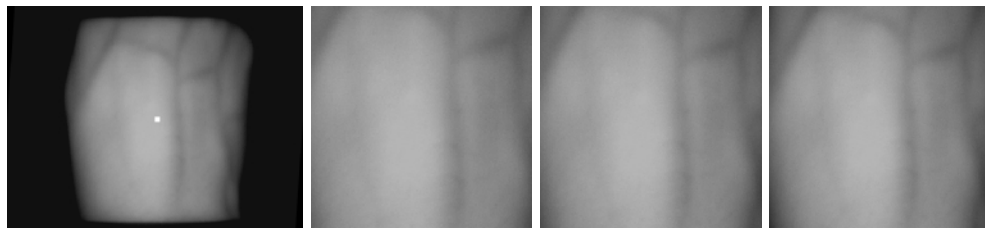
(e) R=360

(f) R=380

(g) R=400

(h) R=420

(17) Left hand of No.9 individual

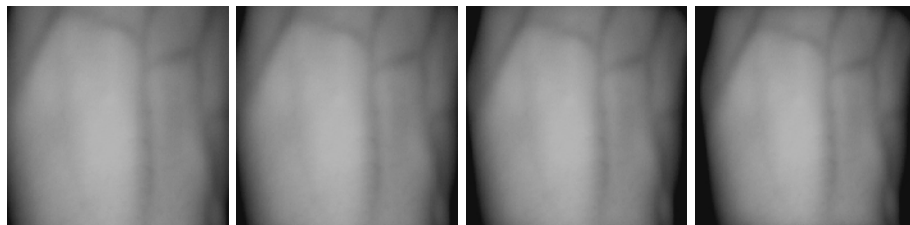


(a) Original

(b) R=300

(c) R=320

(d) R=340



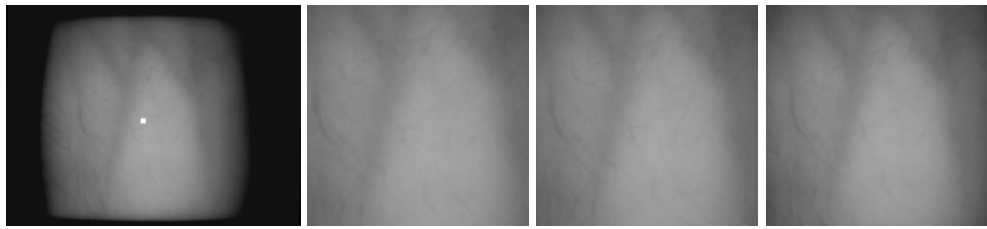
(e) R=360

(f) R=380

(g) R=400

(h) R=420

(18) Right hand of No.9 individual

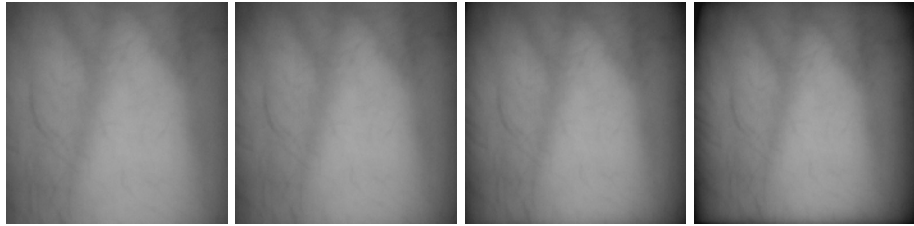


(a) Original

(b) R=300

(c) R=320

(d) R=340



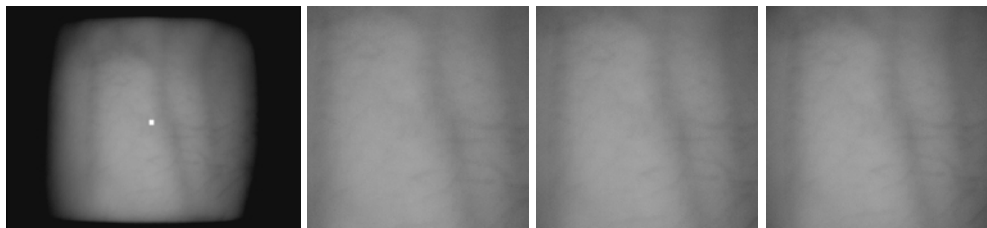
(e) R=360

(f) R=380

(g) R=400

(h) R=420

(19) Left hand of No.10 individual

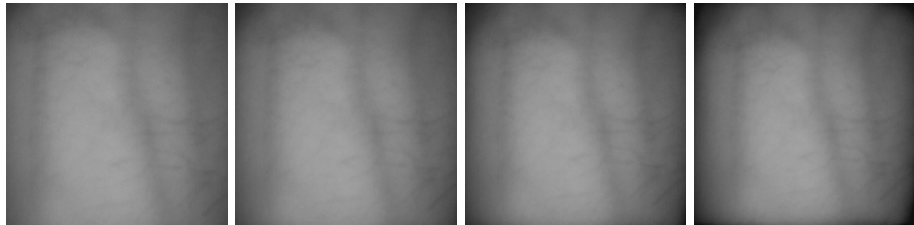


(a) Original

(b) R=300

(c) R=320

(d) R=340



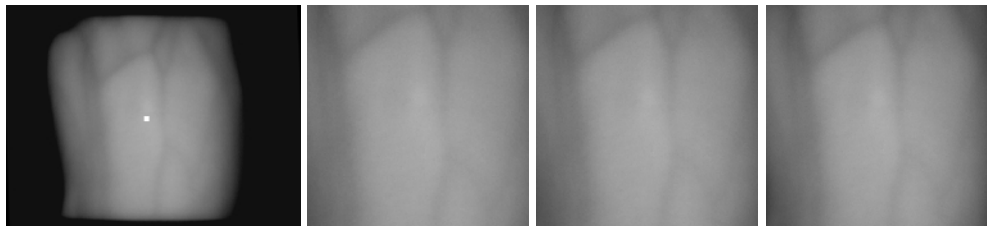
(e) R=360

(f) R=380

(g) R=400

(h) R=420

(20) Right hand of No.10 individual

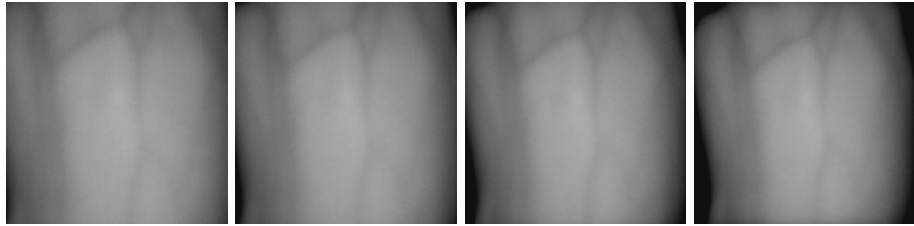


(a) Original

(b) R=300

(c) R=320

(d) R=340



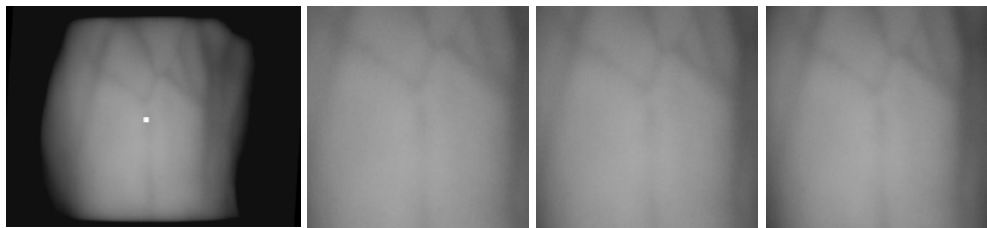
(e) R=360

(f) R=380

(g) R=400

(h) R=420

(21) Left hand of No.11 individual

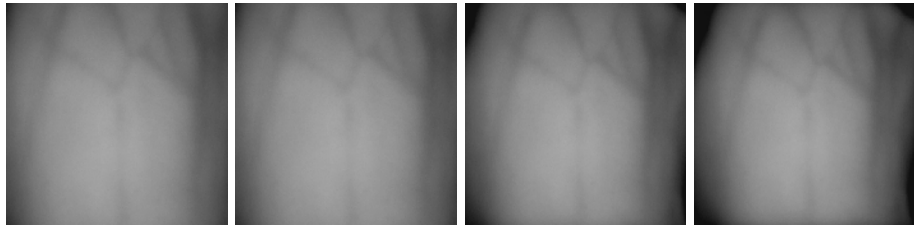


(a) Original

(b) R=300

(c) R=320

(d) R=340



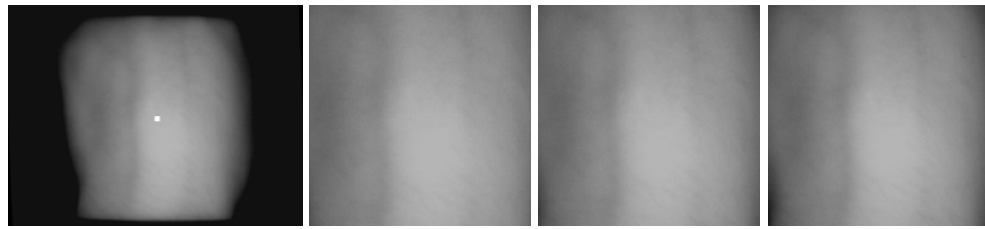
(e) R=360

(f) R=380

(g) R=400

(h) R=420

(22) Right hand of No.11 individual

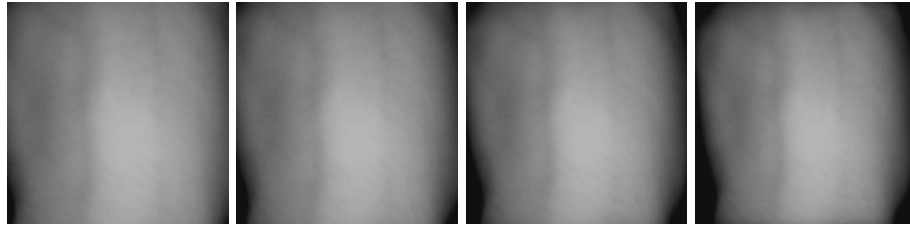


(a) Original

(b) R=300

(c) R=320

(d) R=340



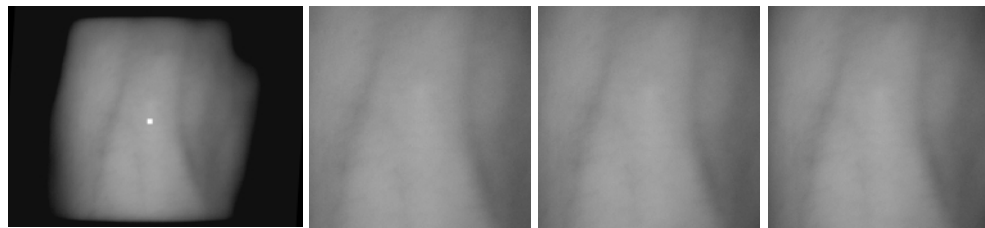
(e) R=360

(f) R=380

(g) R=400

(h) R=420

(23) Left hand of No.12 individual

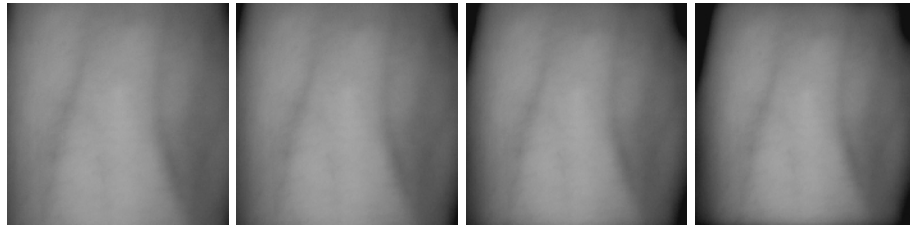


(a) Original

(b) R=300

(c) R=320

(d) R=340



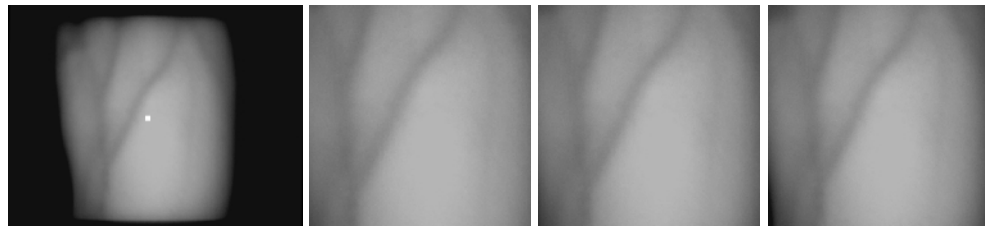
(e) R=360

(f) R=380

(g) R=400

(h) R=420

(24) Right hand of No.12 individual



(a) Original

(b) R=300

(c) R=320

(d) R=340



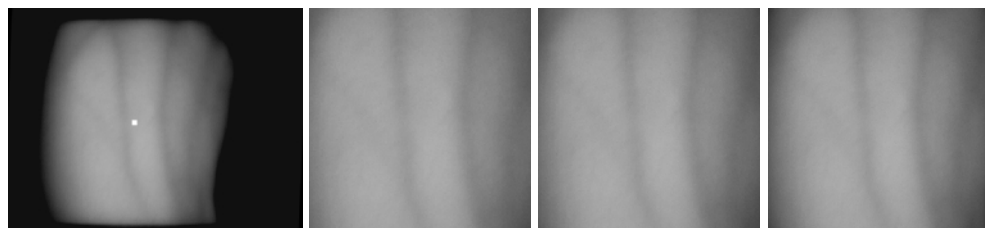
(e) R=360

(f) R=380

(g) R=400

(h) R=420

(25) Left hand of No.13 individual

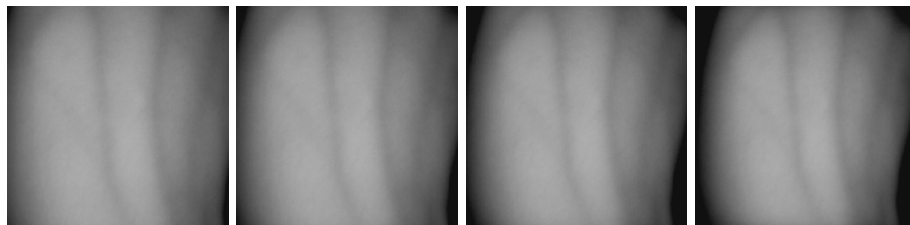


(a) Original

(b) R=300

(c) R=320

(d) R=340



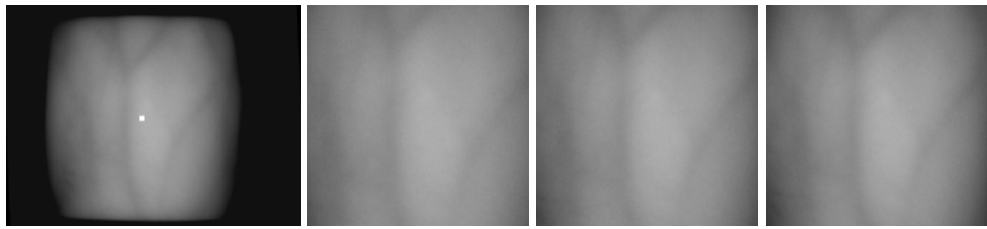
(e) R=360

(f) R=380

(g) R=400

(h) R=420

(26) Right hand of No.13 individual

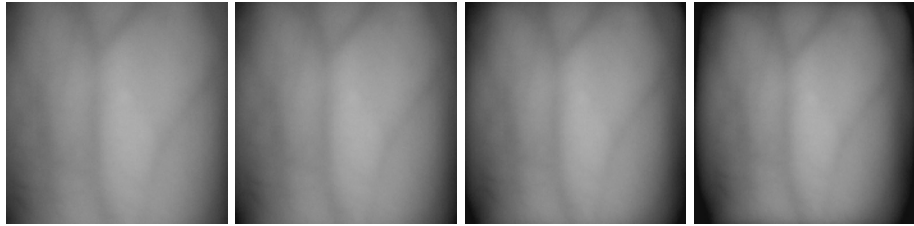


(a) Original

(b) R=300

(c) R=320

(d) R=340



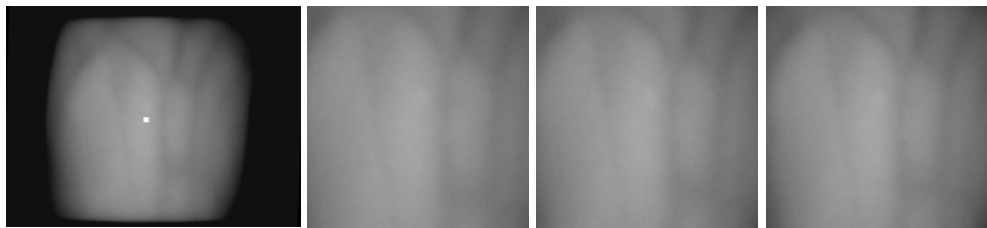
(e) R=360

(f) R=380

(g) R=400

(h) R=420

(27) Left hand of No.14 individual

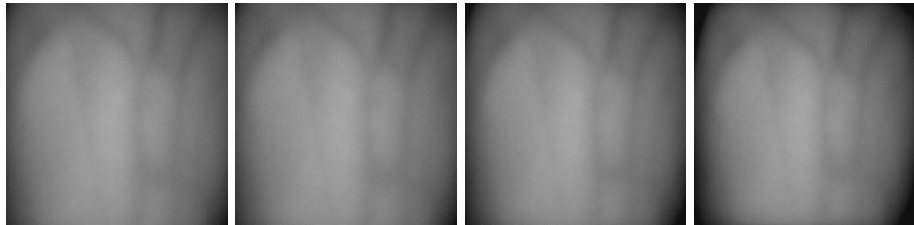


(a) Original

(b) R=300

(c) R=320

(d) R=340



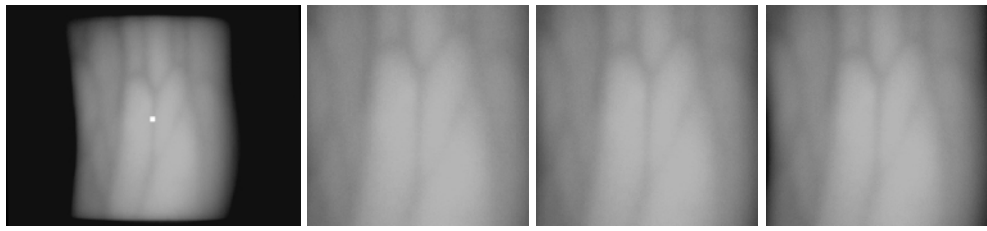
(e) R=360

(f) R=380

(g) R=400

(h) R=420

(28) Right hand of No.14 individual

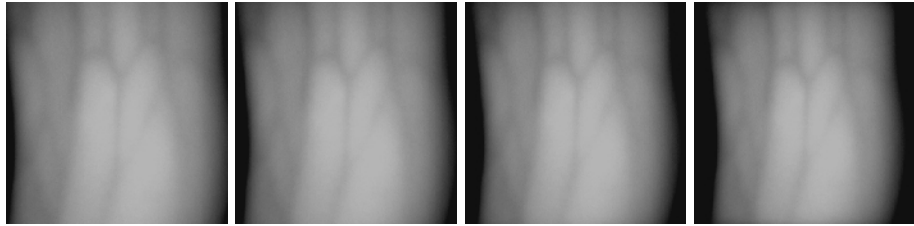


(a) Original

(b) R=300

(c) R=320

(d) R=340



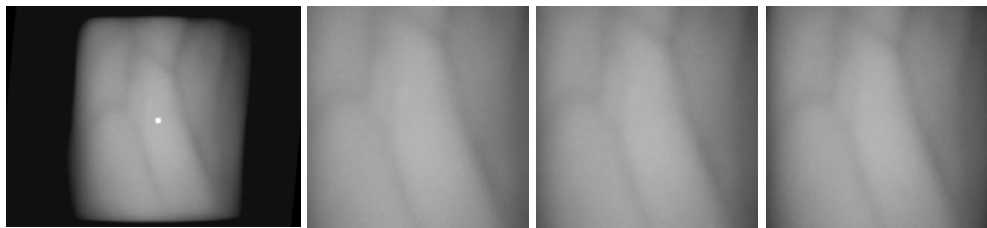
(e) R=360

(f) R=380

(g) R=400

(h) R=420

(29) Left hand of No.15 individual

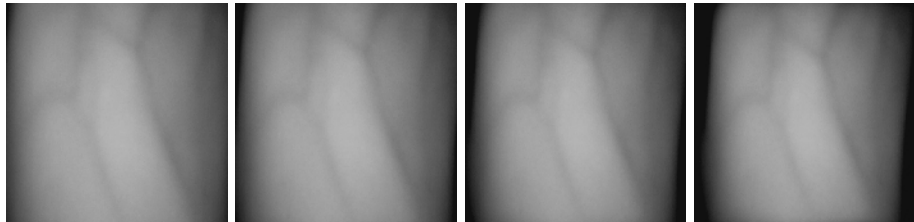


(a) Original

(b) R=300

(c) R=320

(d) R=340



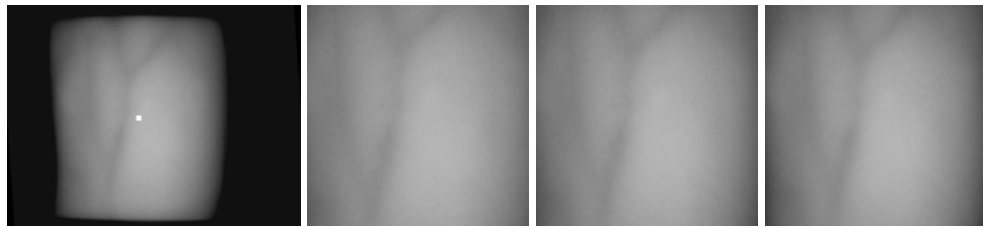
(e) R=360

(f) R=380

(g) R=400

(h) R=420

(30) Right hand of No.15 individual



(a) Original

(b) R=300

(c) R=320

(d) R=340



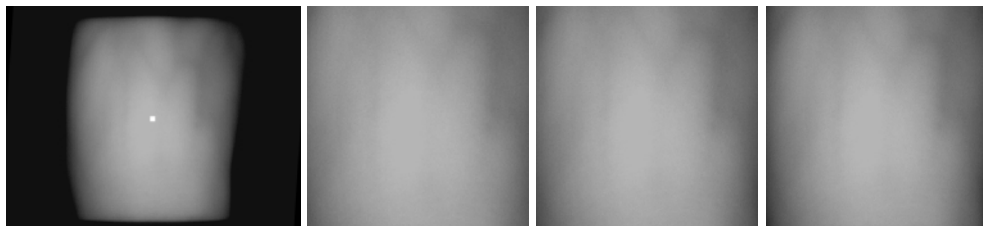
(e) R=360

(f) R=380

(g) R=400

(h) R=420

(31) Left hand of No.16 individual

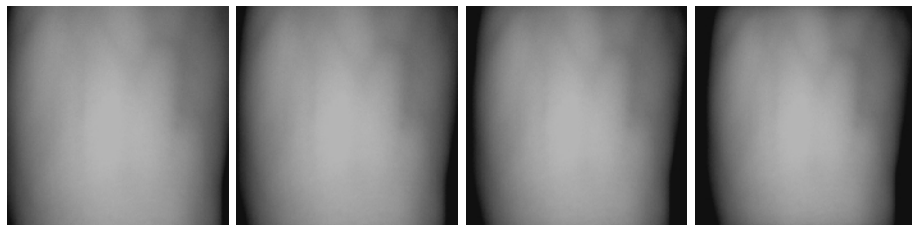


(a) Original

(b) R=300

(c) R=320

(d) R=340



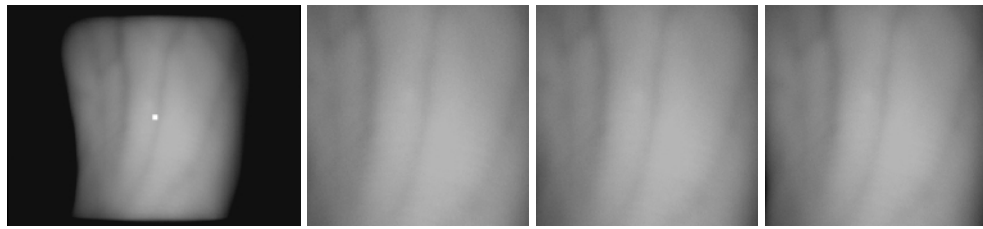
(e) R=360

(f) R=380

(g) R=400

(h) R=420

(32) Right hand of No.16 individual

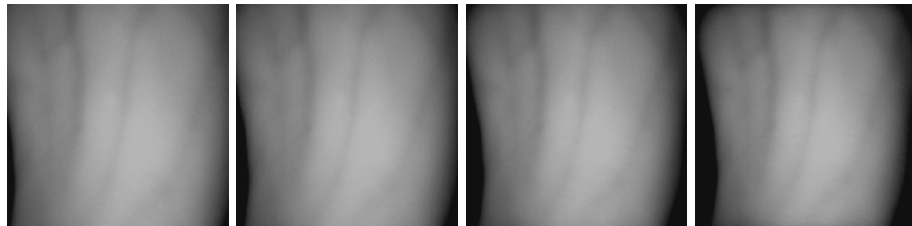


(a) Original

(b) R=300

(c) R=320

(d) R=340



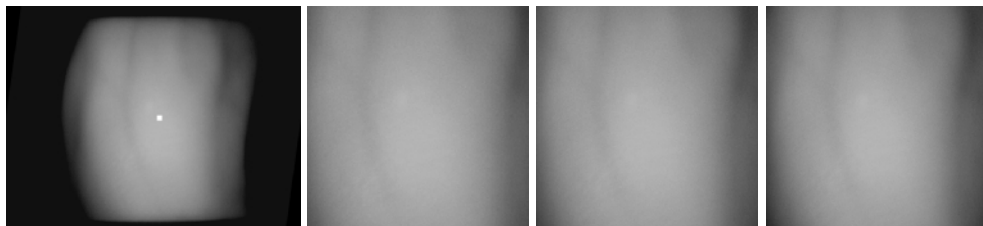
(e) R=360

(f) R=380

(g) R=400

(h) R=420

(33) Left hand of No.17 individual



(a) Original

(b) R=300

(c) R=320

(d) R=340



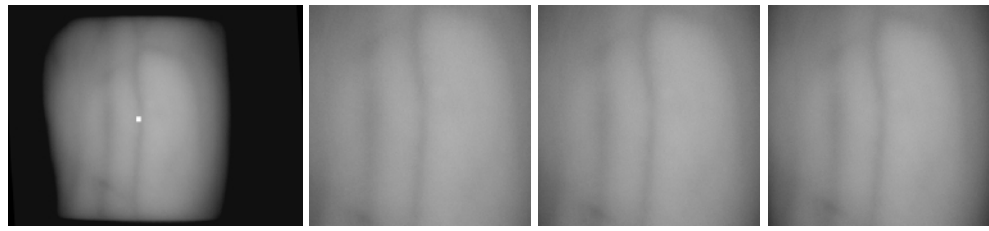
(e) R=360

(f) R=380

(g) R=400

(h) R=420

(34) Right hand of No.17 individual

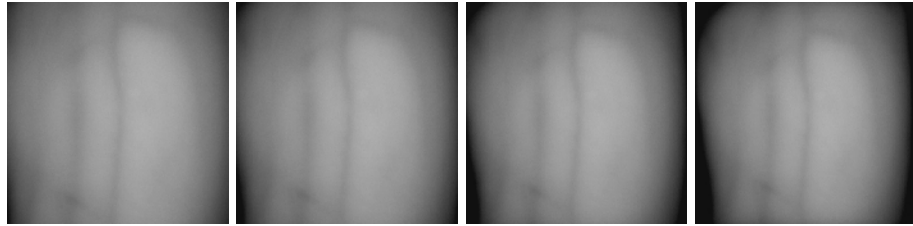


(a) Original

(b) R=300

(c) R=320

(d) R=340



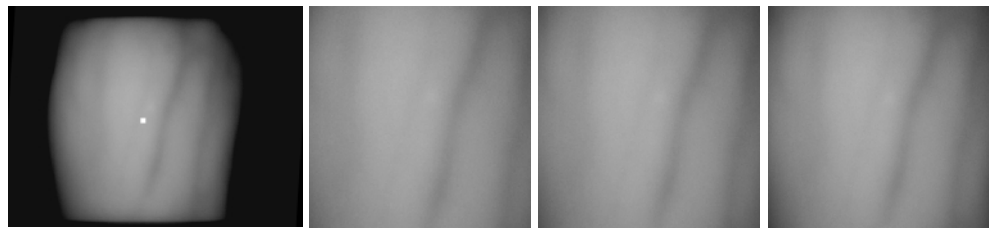
(e) R=360

(f) R=380

(g) R=400

(h) R=420

(35) Left hand of No.18 individual



(a) Original

(b) R=300

(c) R=320

(d) R=340



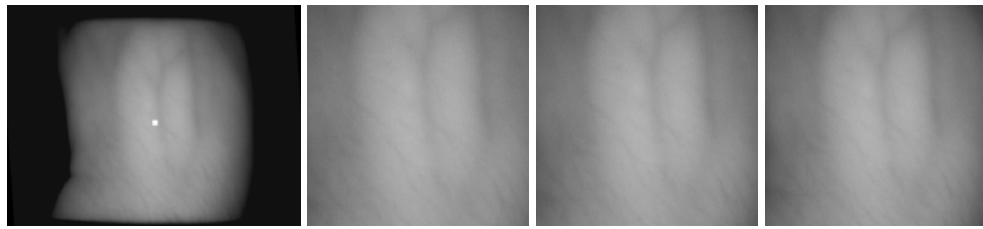
(e) R=360

(f) R=380

(g) R=400

(h) R=420

(36) Right hand of No.18 individual

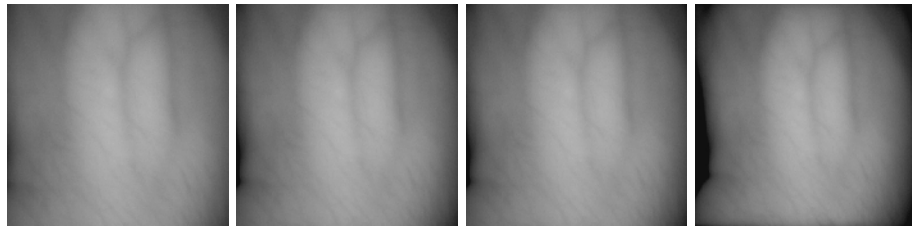


(a) Original

(b) R=300

(c) R=320

(d) R=340



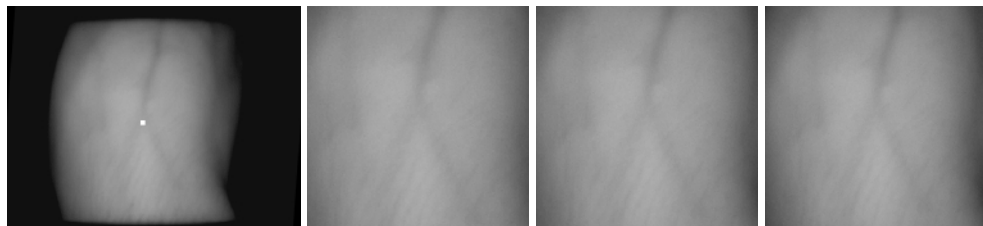
(e) R=360

(f) R=380

(g) R=400

(h) R=420

(37) Left hand of No.19 individual

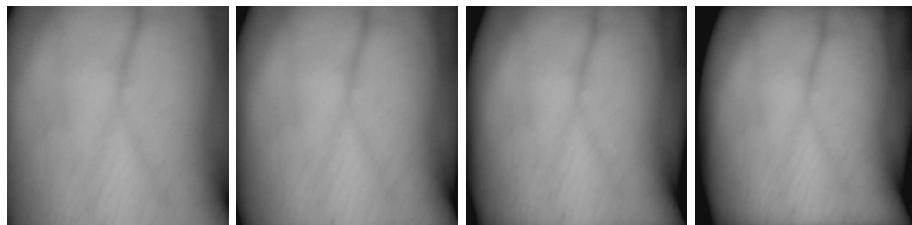


(a) Original

(b) R=300

(c) R=320

(d) R=340



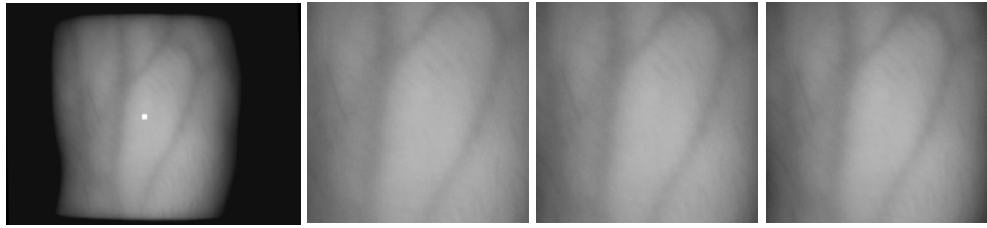
(e) R=360

(f) R=380

(g) R=400

(h) R=420

(38) Right hand of No.19 individual

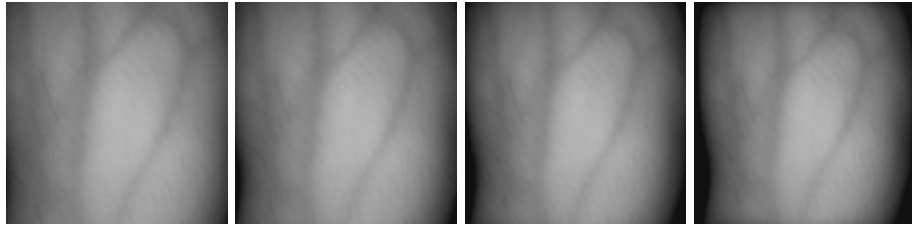


(a) Original

(b) R=300

(c) R=320

(d) R=340



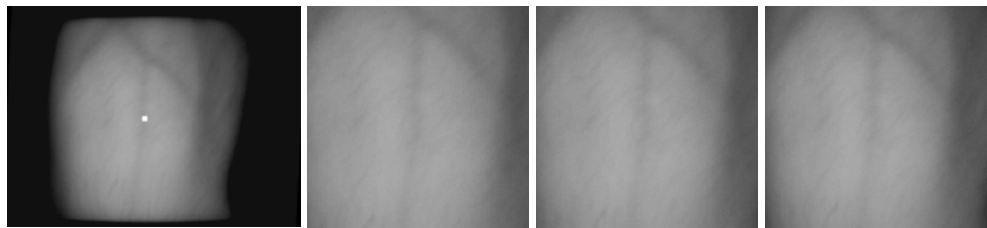
(e) R=360

(f) R=380

(g) R=400

(h) R=420

(39) Left hand of No.20 individual

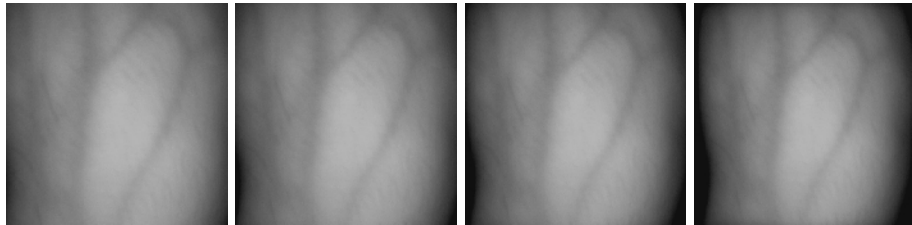


(a) Original

(b) R=300

(c) R=320

(d) R=340



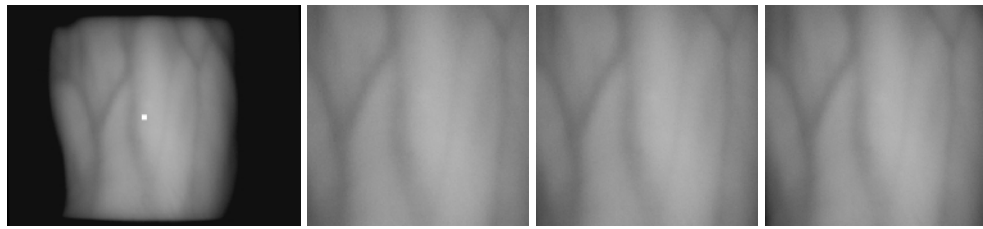
(e) R=360

(f) R=380

(g) R=400

(h) R=420

(40) Right hand of No.20 individual

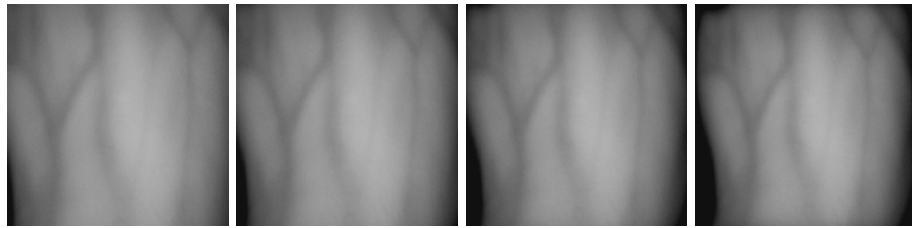


(a) Original

(b) R=300

(c) R=320

(d) R=340



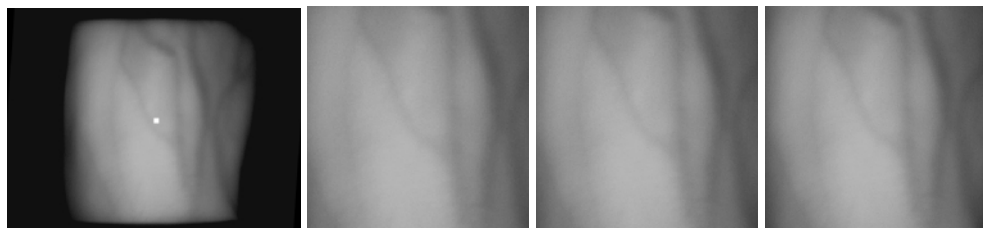
(e) R=360

(f) R=380

(g) R=400

(h) R=420

(41) Left hand of No.21 individual

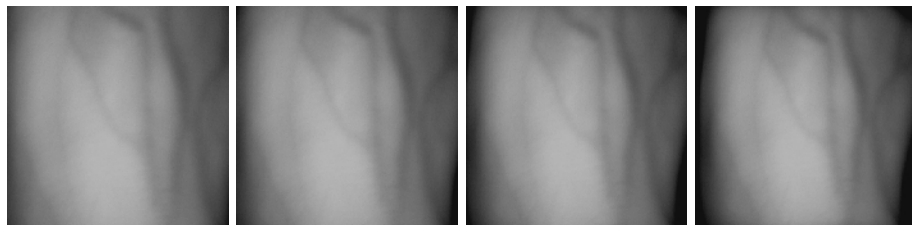


(a) Original

(b) R=300

(c) R=320

(d) R=340



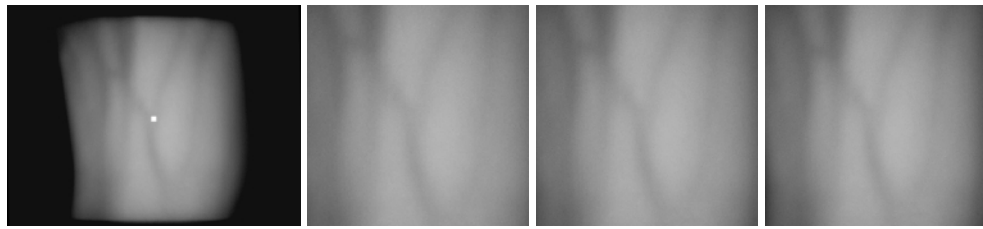
(e) R=360

(f) R=380

(g) R=400

(h) R=420

(42) Right hand of No.21 individual



(a) Original

(b) R=300

(c) R=320

(d) R=340



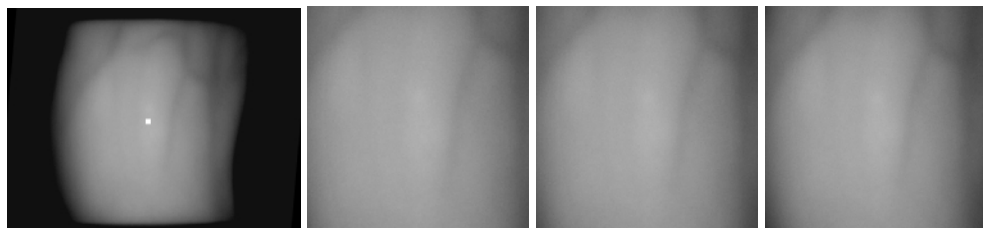
(e) R=360

(f) R=380

(g) R=400

(h) R=420

(43) Left hand of No.22 individual

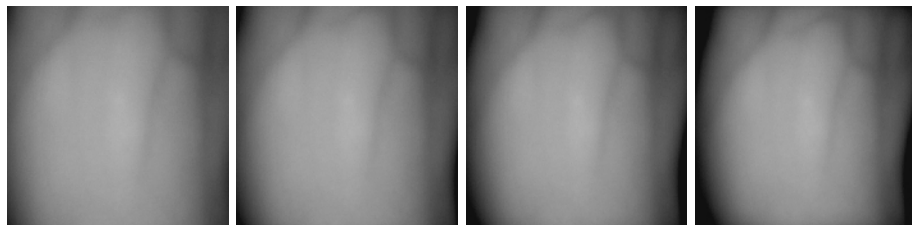


(a) Original

(b) R=300

(c) R=320

(d) R=340



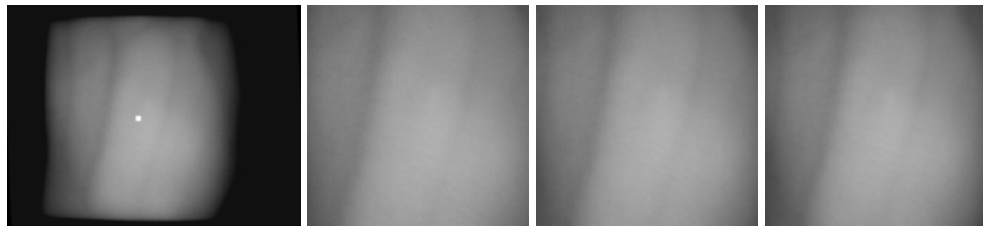
(e) R=360

(f) R=380

(g) R=400

(h) R=420

(44) Right hand of No.22 individual

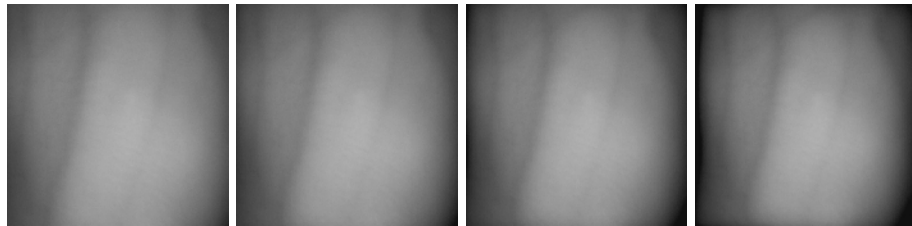


(a) Original

(b) R=300

(c) R=320

(d) R=340



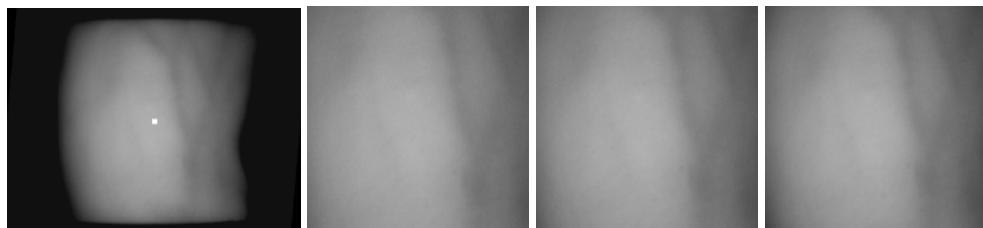
(e) R=360

(f) R=380

(g) R=400

(h) R=420

(45) Left hand of No.23 individual

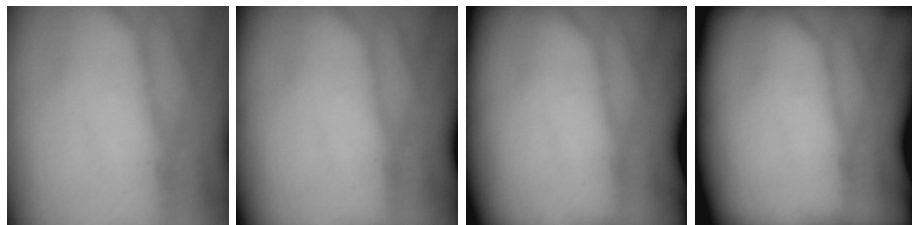


(a) Original

(b) R=300

(c) R=320

(d) R=340



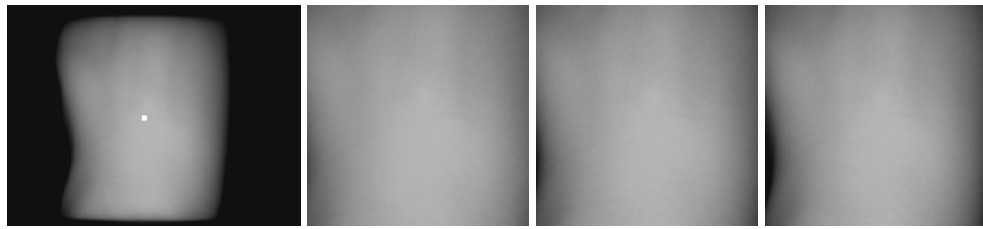
(e) R=360

(f) R=380

(g) R=400

(h) R=420

(46) Right hand of No.23 individual

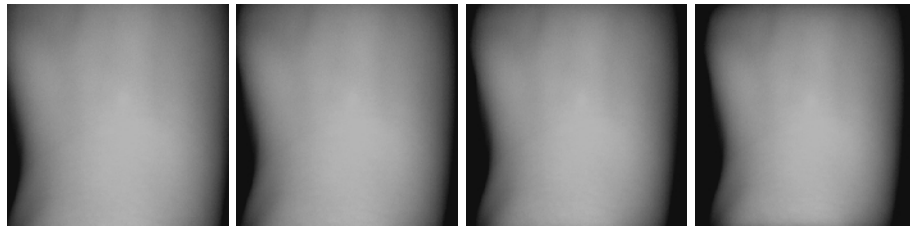


(a) Original

(b) R=300

(c) R=320

(d) R=340



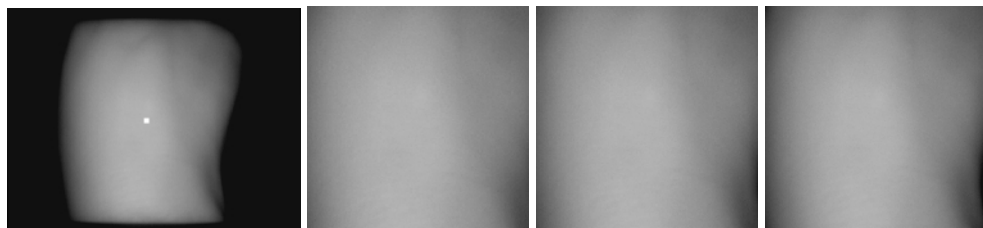
(e) R=360

(f) R=380

(g) R=400

(h) R=420

(47) Left hand of No.24 individual

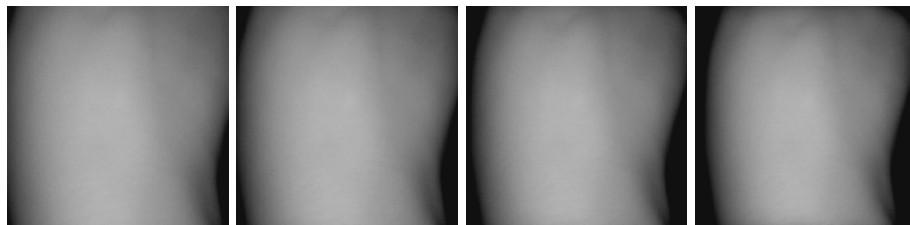


(a) Original

(b) R=300

(c) R=320

(d) R=340



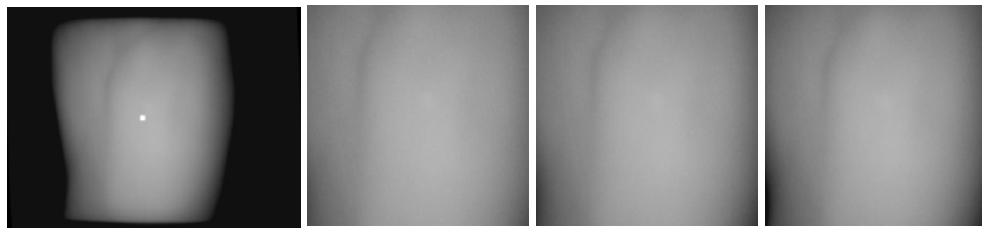
(e) R=360

(f) R=380

(g) R=400

(h) R=420

(48) Right hand of No.24 individual



(a) Original

(b) R=300

(c) R=320

(d) R=340



(e) R=360

(f) R=380

(g) R=400

(h) R=420

(49) Left hand of No.25 individual



(a) Original

(b) R=300

(c) R=320

(d) R=340



(e) R=360

(f) R=380

(g) R=400

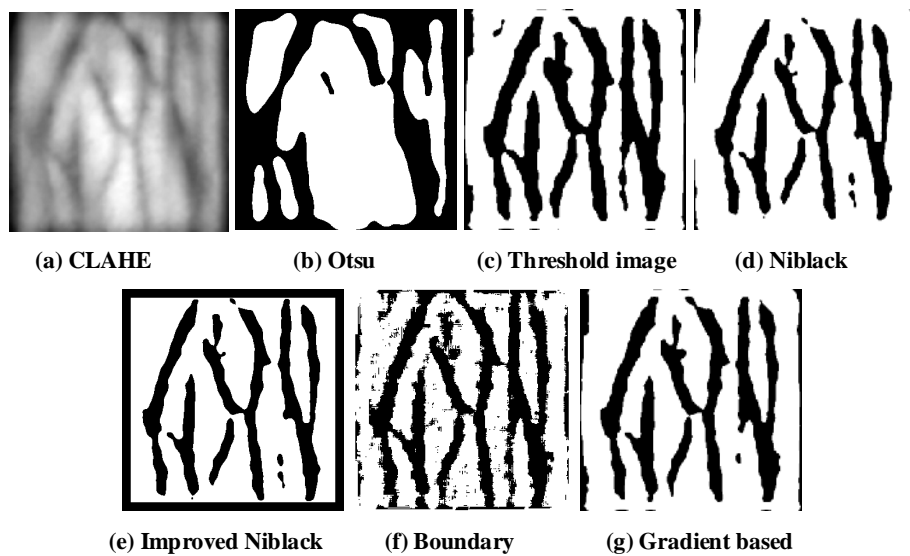
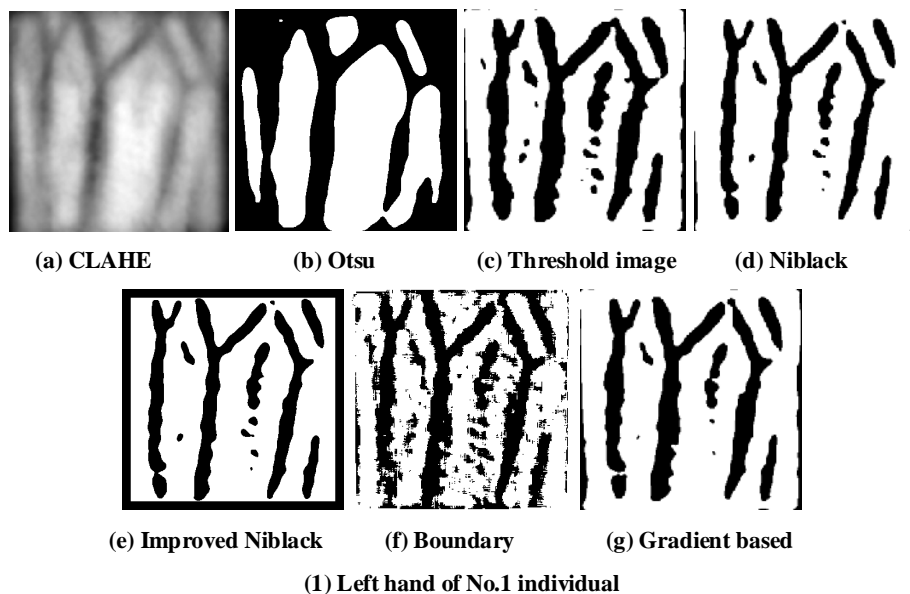
(h) R=420

(50) Right hand of No.25 individual

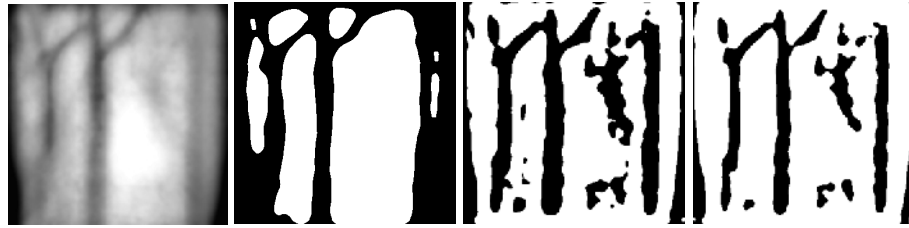
Figure A-1 Results of ROI extraction with R ranging from 300 to 420

Appendix B. RESULTS OF SEGMENTATION

This appendix gives the results of segmentation methods. 25 of all 102 individuals are listed, including left and right hand for each one. For every hand, the first image is the image before segmentation, sequent are results of Otsu, Threshold Image, Niblack ($L=15$), improved Niblack ($L=15$), the boundary method and the gradient based method ($a = 0.01$, $b = 0.02$, $N=L=15$).



(2) Right hand of No.1 individual

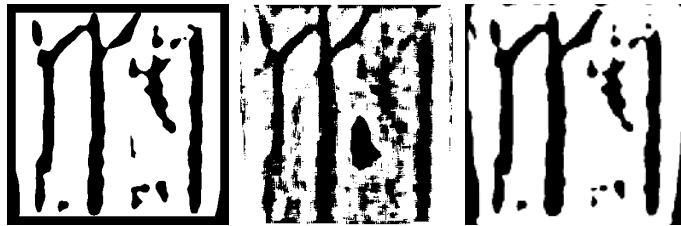


(a) CLAHE

(b) Otsu

(c) Threshold image

(d) Niblack

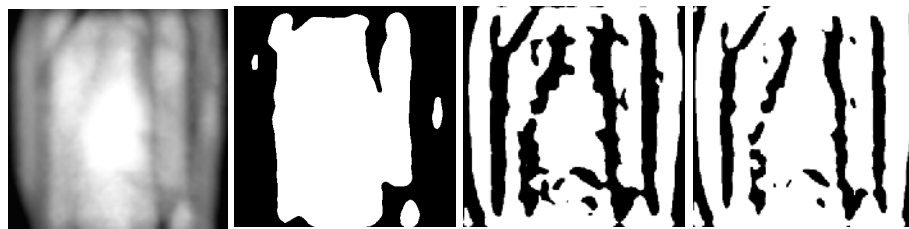


(e) Improved Niblack

(f) Boundary

(g) Gradient based

(3) Left hand of No.2 individual

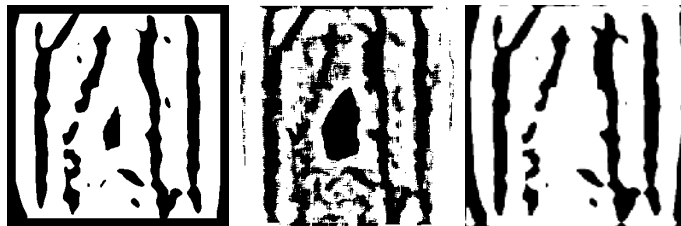


(a) CLAHE

(b) Otsu

(c) Threshold image

(d) Niblack

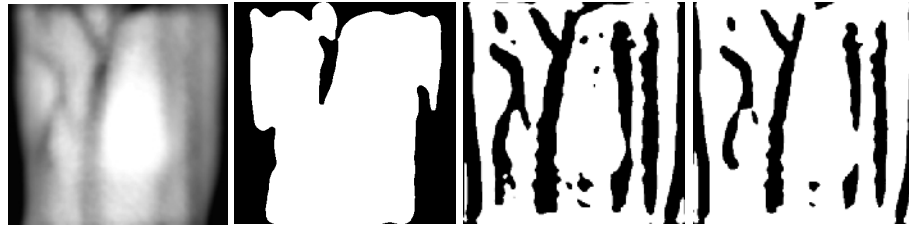


(e) Improved Niblack

(f) Boundary

(g) Gradient based

(4) Right hand of No.2 individual

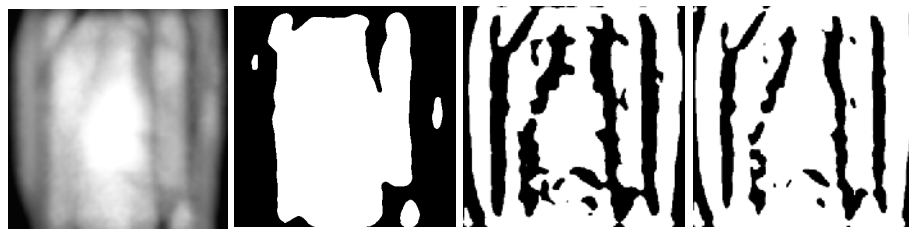


(a) CLAHE (b) Otsu (c) Threshold image (d) Niblack

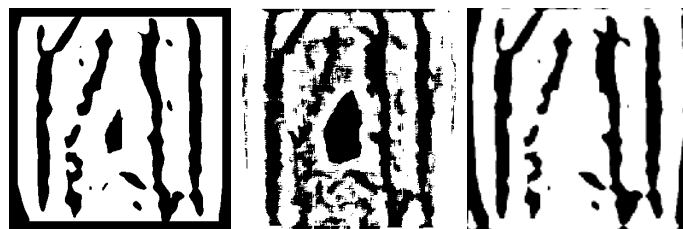


(e) Improved Niblack (f) Boundary (g) Gradient based

(5) Left hand of No.3 individual

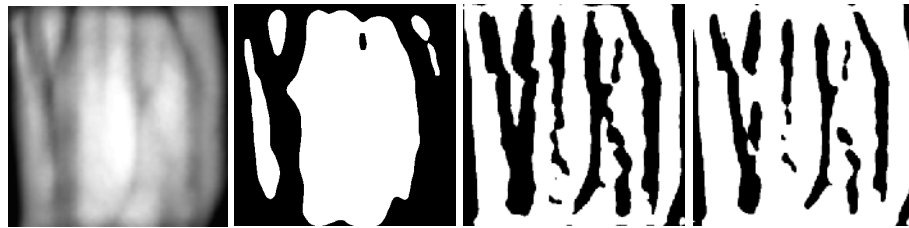


(a) CLAHE (b) Otsu (c) Threshold image (d) Niblack



(e) Improved Niblack (f) Boundary (g) Gradient based

(6) Right hand of No.3 individual

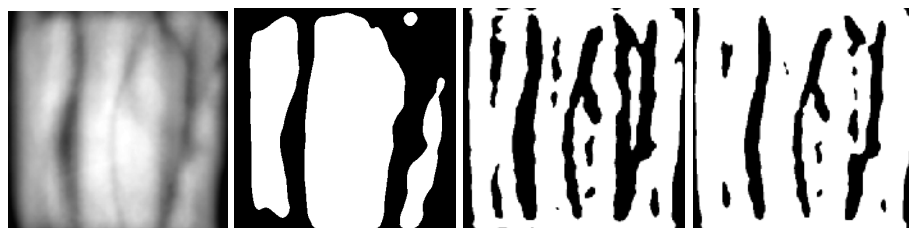


(a) CLAHE (b) Otsu (c) Threshold image (d) Niblack



(e) Improved Niblack (f) Boundary (g) Gradient based

(7) Left hand of No.4 individual

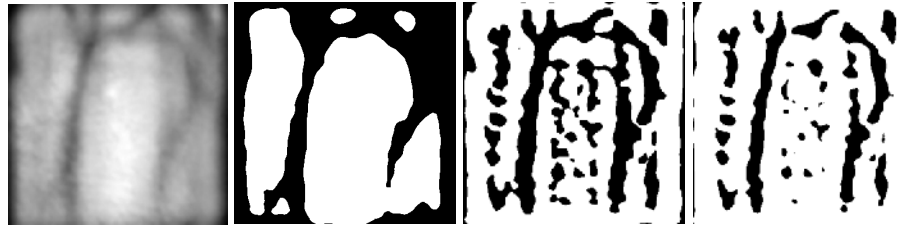


(a) CLAHE (b) Otsu (c) Threshold image (d) Niblack



(e) Improved Niblack (f) Boundary (g) Gradient based

(8) Right hand of No.4 individual

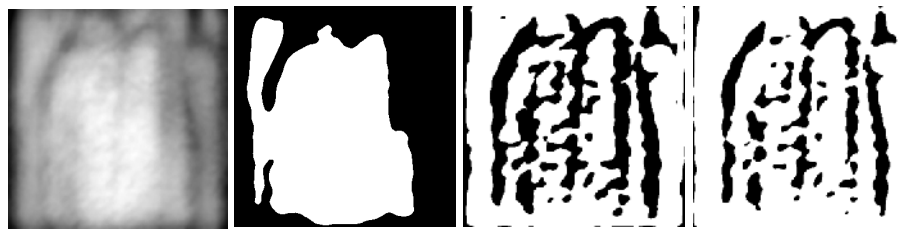


(a) CLAHE (b) Otsu (c) Threshold image (d) Niblack

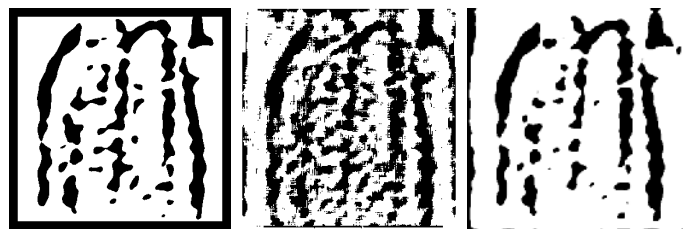


(e) Improved Niblack (f) Boundary (g) Gradient based

(9) Left hand of No.5 individual

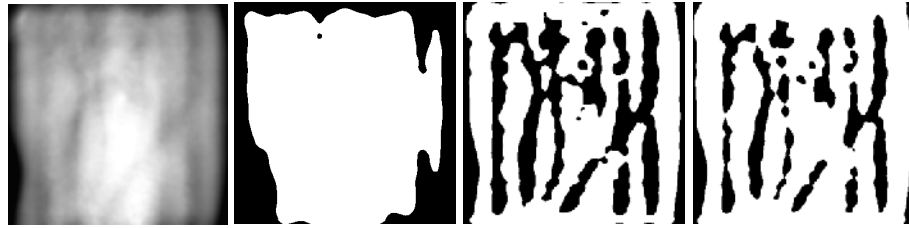


(a) CLAHE (b) Otsu (c) Threshold image (d) Niblack



(e) Improved Niblack (f) Boundary (g) Gradient based

(10) Right hand of No.5 individual

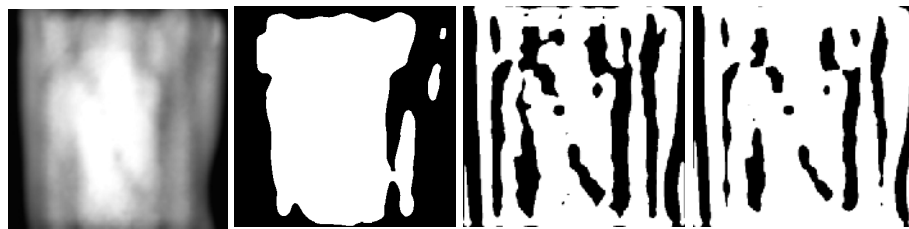


(a) CLAHE (b) Otsu (c) Threshold image (d) Niblack



(e) Improved Niblack (f) Boundary (g) Gradient based

(11) Left hand of No.6 individual

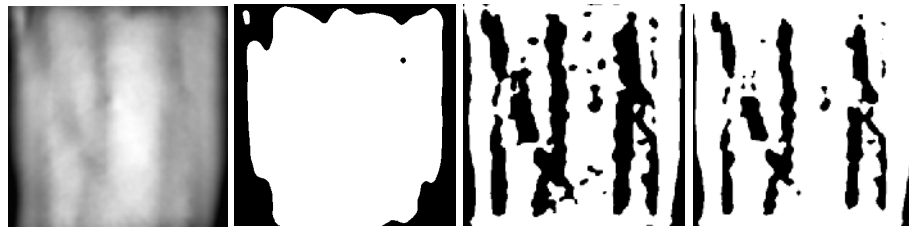


(a) CLAHE (b) Otsu (c) Threshold image (d) Niblack

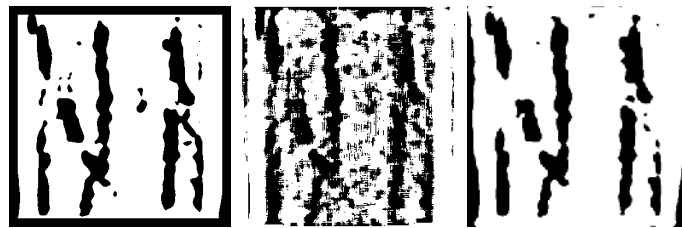


(e) Improved Niblack (f) Boundary (g) Gradient based

(12) Right hand of No.6 individual

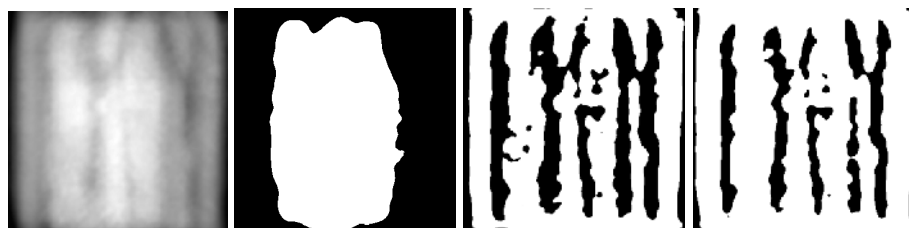


(a) CLAHE (b) Otsu (c) Threshold image (d) Niblack

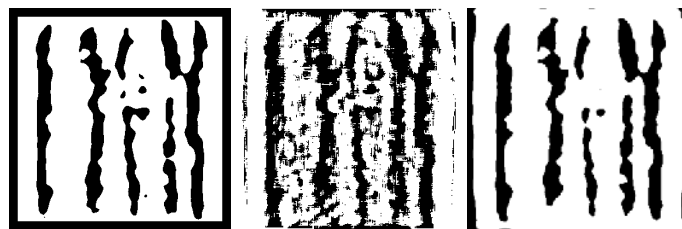


(e) Improved Niblack (f) Boundary (g) Gradient based

(13) Left hand of No.7 individual

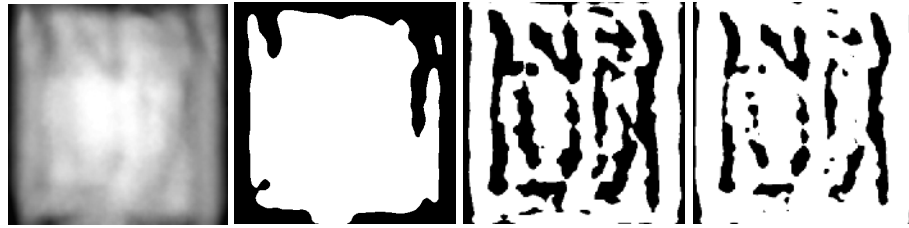


(a) CLAHE (b) Otsu (c) Threshold image (d) Niblack



(e) Improved Niblack (f) Boundary (g) Gradient based

(14) Right hand of No.7 individual

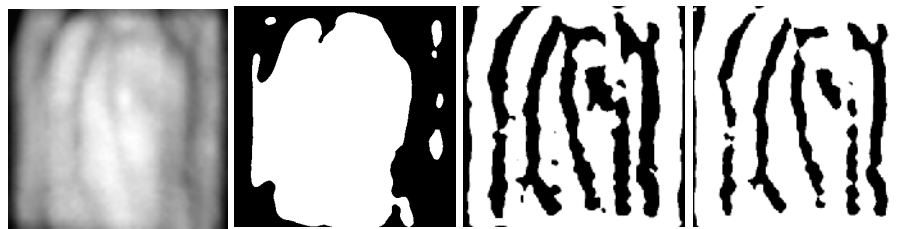


(a) CLAHE (b) Otsu (c) Threshold image (d) Niblack



(e) Improved Niblack (f) Boundary (g) Gradient based

(15) Left hand of No.8 individual

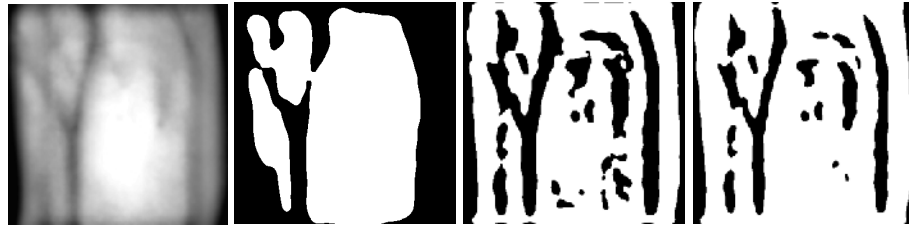


(a) CLAHE (b) Otsu (c) Threshold image (d) Niblack

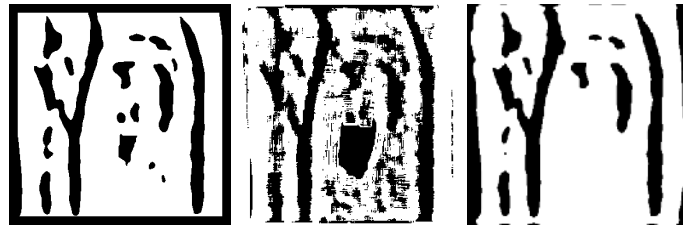


(e) Improved Niblack (f) Boundary (g) Gradient based

(16) Right hand of No.8 individual



(a) CLAHE (b) Otsu (c) Threshold image (d) Niblack



(e) Improved Niblack (f) Boundary (g) Gradient based

(17) Left hand of No.9 individual



(a) CLAHE (b) Otsu (c) Threshold image (d) Niblack

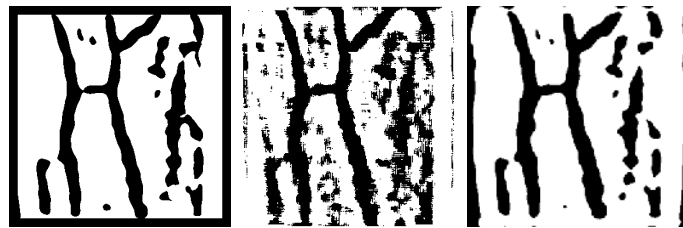


(e) Improved Niblack (f) Boundary (g) Gradient based

(18) Right hand of No.9 individual

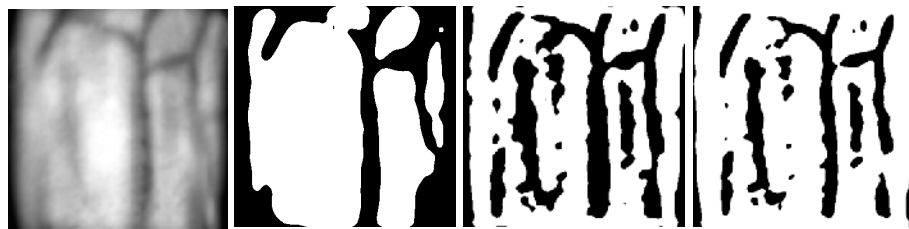


(a) CLAHE (b) Otsu (c) Threshold image (d) Niblack



(e) Improved Niblack (f) Boundary (g) Gradient based

(19) Left hand of No.10 individual

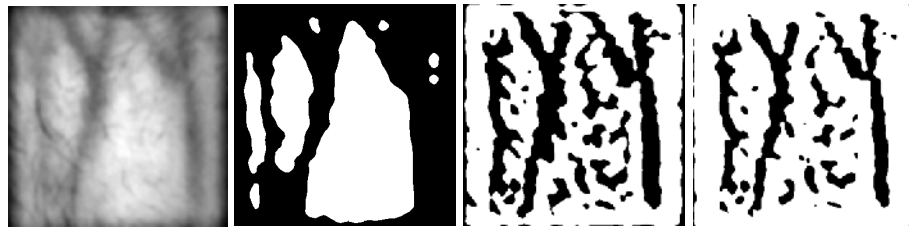


(a) CLAHE (b) Otsu (c) Threshold image (d) Niblack

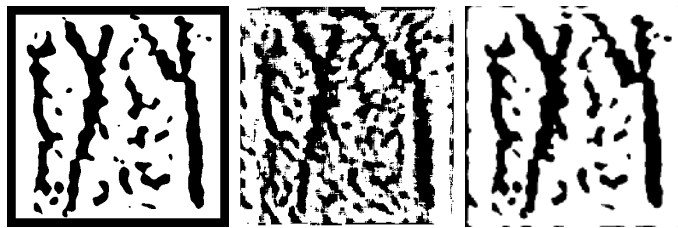


(e) Improved Niblack (f) Boundary (g) Gradient based

(20) Right hand of No.10 individual

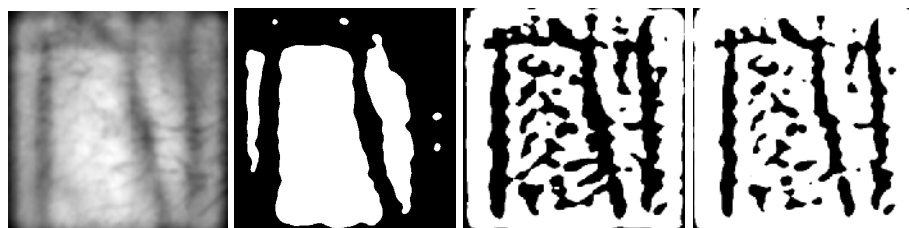


(a) CLAHE (b) Otsu (c) Threshold image (d) Niblack



(e) Improved Niblack (f) Boundary (g) Gradient based

(21) Left hand of No.11 individual

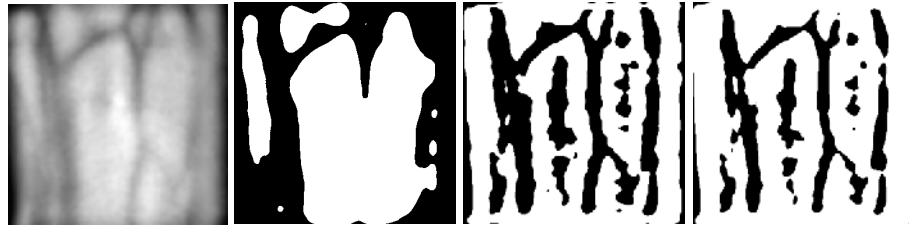


(a) CLAHE (b) Otsu (c) Threshold image (d) Niblack



(e) Improved Niblack (f) Boundary (g) Gradient based

(22) Right hand of No.11 individual



(a) CLAHE (b) Otsu (c) Threshold image (d) Niblack



(e) Improved Niblack (f) Boundary (g) Gradient based

(23) Left hand of No.12 individual

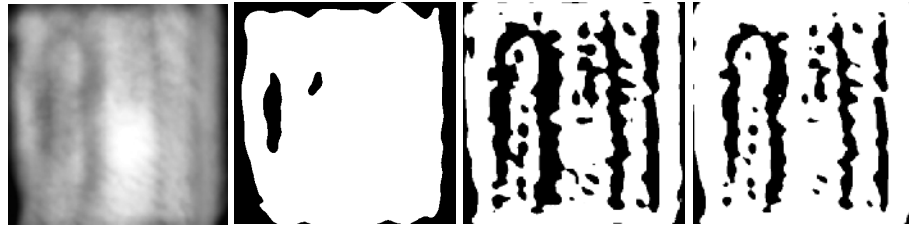


(a) CLAHE (b) Otsu (c) Threshold image (d) Niblack

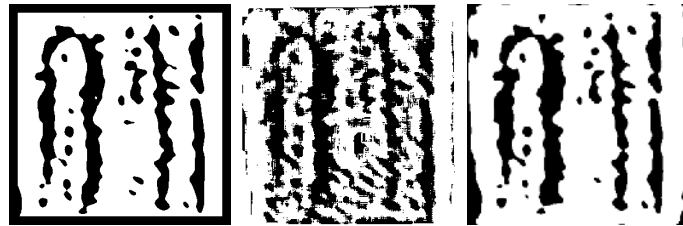


(e) Improved Niblack (f) Boundary (g) Gradient based

(24) Right hand of No.12 individual

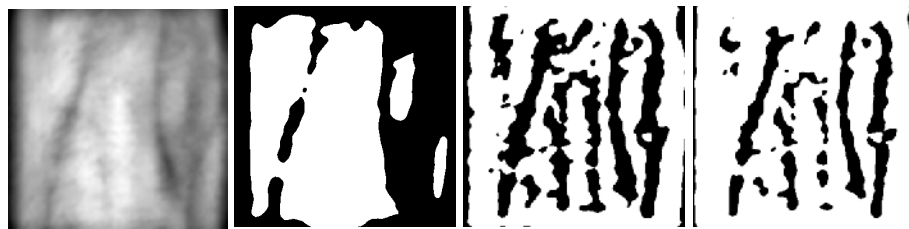


(a) CLAHE (b) Otsu (c) Threshold image (d) Niblack



(e) Improved Niblack (f) Boundary (g) Gradient based

(25) Left hand of No.13 individual

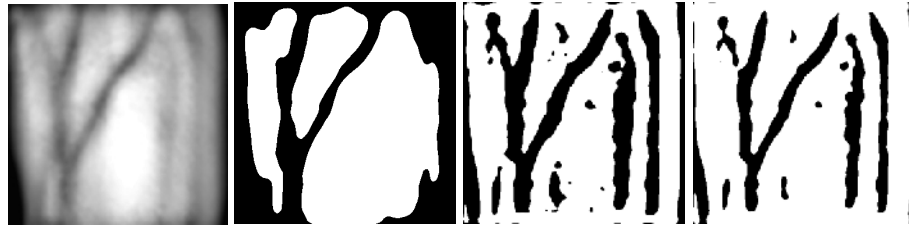


(a) CLAHE (b) Otsu (c) Threshold image (d) Niblack

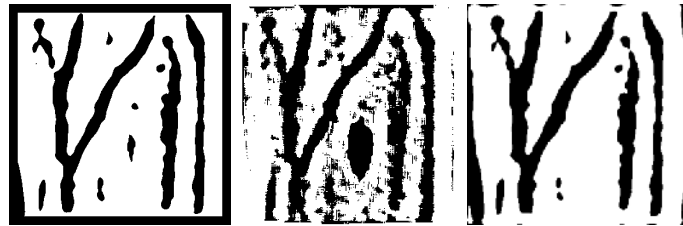


(e) Improved Niblack (f) Boundary (g) Gradient based

(26) Right hand of No.13 individual

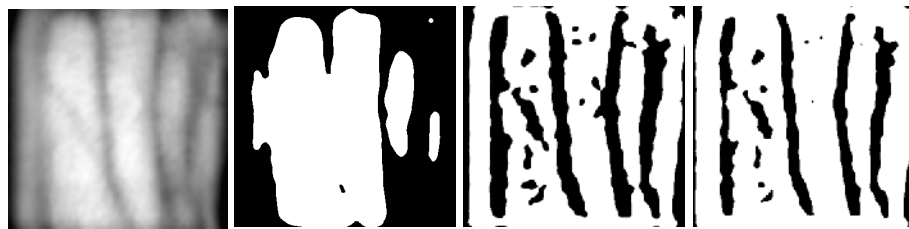


(a) CLAHE (b) Otsu (c) Threshold image (d) Niblack

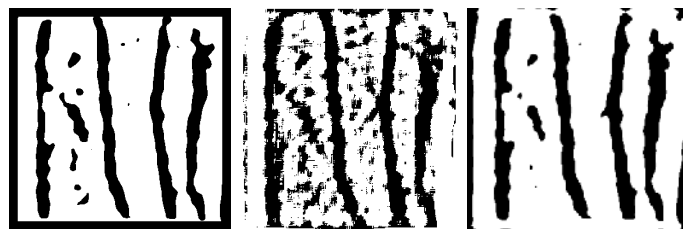


(e) Improved Niblack (f) Boundary (g) Gradient based

(27) Left hand of No.14 individual

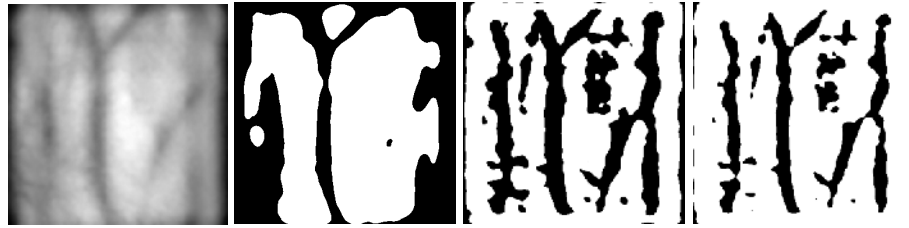


(a) CLAHE (b) Otsu (c) Threshold image (d) Niblack



(e) Improved Niblack (f) Boundary (g) Gradient based

(28) Right hand of No.14 individual

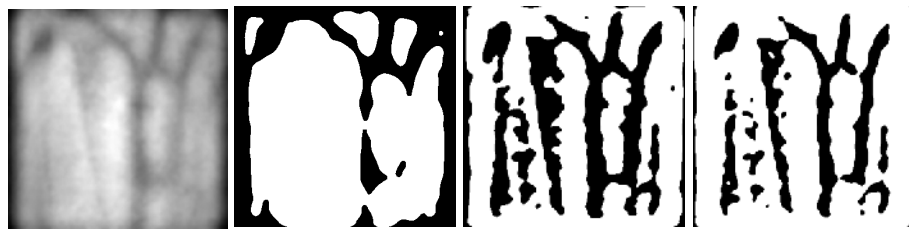


(a) CLAHE (b) Otsu (c) Threshold image (d) Niblack



(e) Improved Niblack (f) Boundary (g) Gradient based

(29) Left hand of No.15 individual



(a) CLAHE (b) Otsu (c) Threshold image (d) Niblack

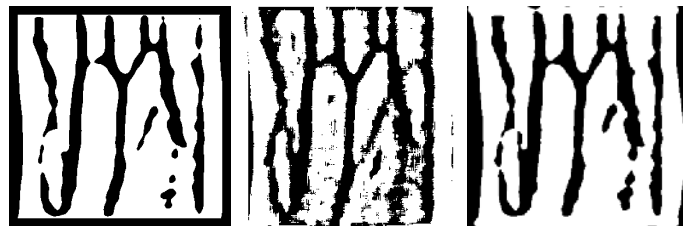


(e) Improved Niblack (f) Boundary (g) Gradient based

(30) Right hand of No.15 individual



(a) CLAHE (b) Otsu (c) Threshold image (d) Niblack

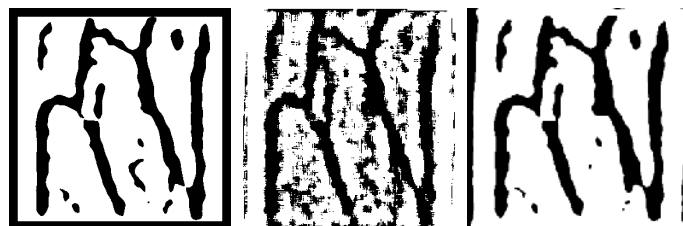


(e) Improved Niblack (f) Boundary (g) Gradient based

(31) Left hand of No.16 individual

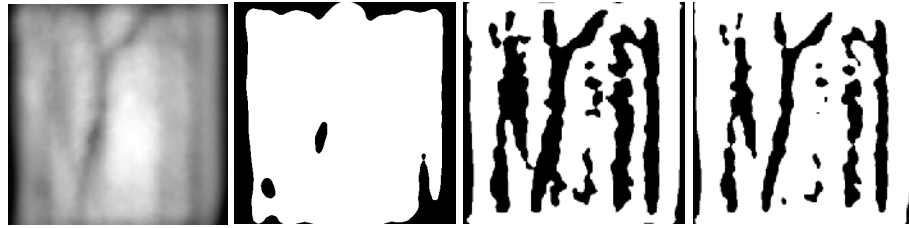


(a) CLAHE (b) Otsu (c) Threshold image (d) Niblack



(e) Improved Niblack (f) Boundary (g) Gradient based

(32) Right hand of No.16 individual

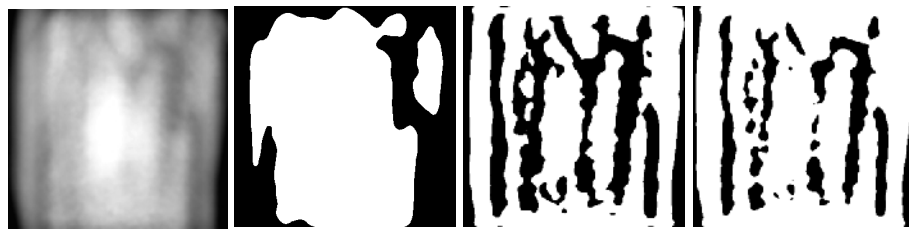


(a) CLAHE (b) Otsu (c) Threshold image (d) Niblack

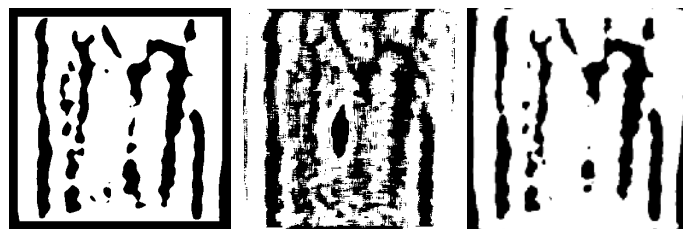


(e) Improved Niblack (f) Boundary (g) Gradient based

(33) Left hand of No.17 individual



(a) CLAHE (b) Otsu (c) Threshold image (d) Niblack

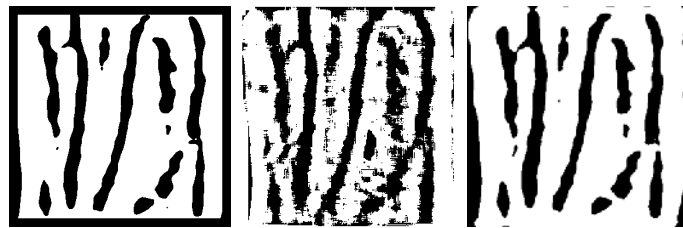


(e) Improved Niblack (f) Boundary (g) Gradient based

(34) Right hand of No.17 individual



(a) CLAHE (b) Otsu (c) Threshold image (d) Niblack



(e) Improved Niblack (f) Boundary (g) Gradient based

(35) Left hand of No.18 individual

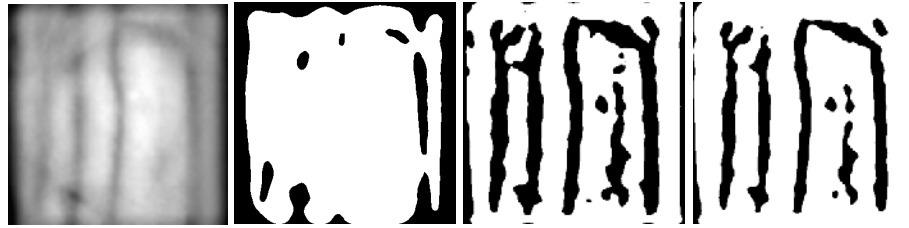


(a) CLAHE (b) Otsu (c) Threshold image (d) Niblack



(e) Improved Niblack (f) Boundary (g) Gradient based

(36) Right hand of No.18 individual



(a) CLAHE (b) Otsu (c) Threshold image (d) Niblack



(e) Improved Niblack (f) Boundary (g) Gradient based

(37) Left hand of No.19 individual

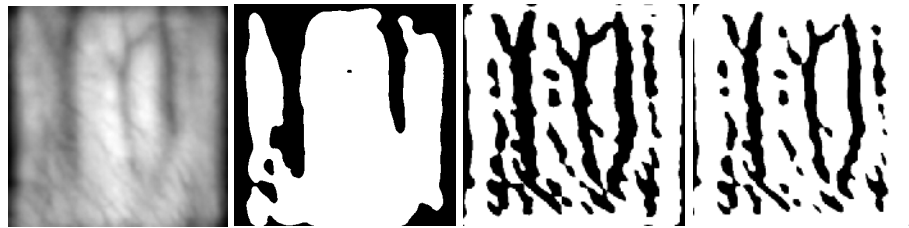


(a) CLAHE (b) Otsu (c) Threshold image (d) Niblack

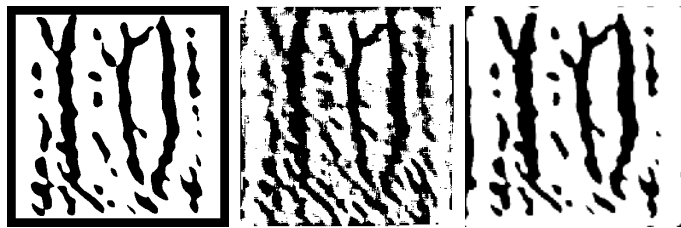


(e) Improved Niblack (f) Boundary (g) Gradient based

(38) Right hand of No.19 individual



(a) CLAHE (b) Otsu (c) Threshold image (d) Niblack



(e) Improved Niblack (f) Boundary (g) Gradient based

(39) Left hand of No.20 individual

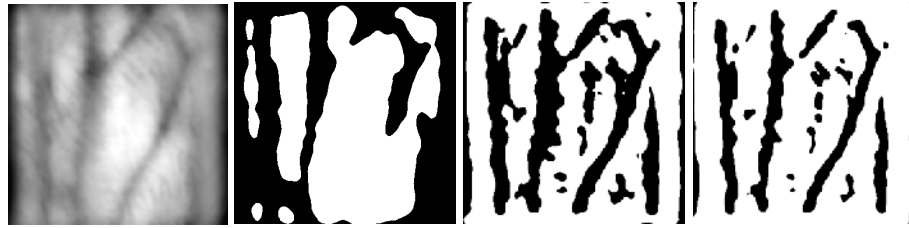


(a) CLAHE (b) Otsu (c) Threshold image (d) Niblack



(e) Improved Niblack (f) Boundary (g) Gradient based

(40) Right hand of No.20 individual



(a) CLAHE (b) Otsu (c) Threshold image (d) Niblack



(e) Improved Niblack (f) Boundary (g) Gradient based

(41) Left hand of No.21 individual



(a) CLAHE (b) Otsu (c) Threshold image (d) Niblack



(e) Improved Niblack (f) Boundary (g) Gradient based

(42) Right hand of No.21 individual

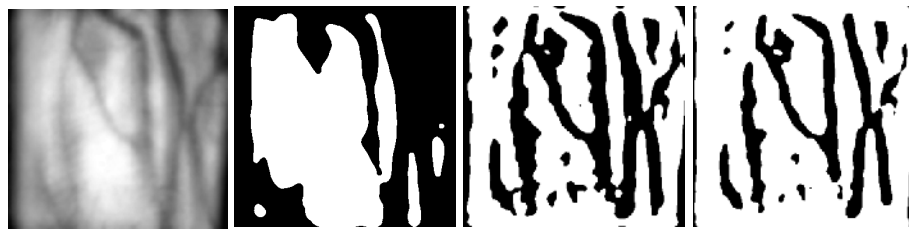


(a) CLAHE (b) Otsu (c) Threshold image (d) Niblack



(e) Improved Niblack (f) Boundary (g) Gradient based

(43) Left hand of No.22 individual

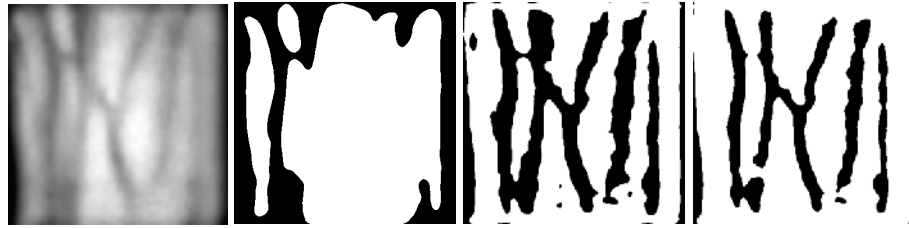


(a) CLAHE (b) Otsu (c) Threshold image (d) Niblack



(e) Improved Niblack (f) Boundary (g) Gradient based

(44) Right hand of No.22 individual

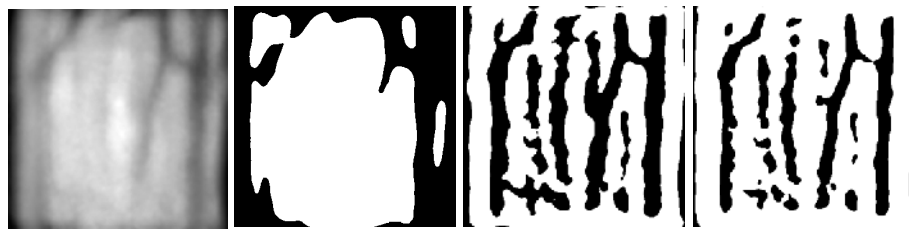


(a) CLAHE (b) Otsu (c) Threshold image (d) Niblack



(e) Improved Niblack (f) Boundary (g) Gradient based

(45) Left hand of No.23 individual



(a) CLAHE (b) Otsu (c) Threshold image (d) Niblack

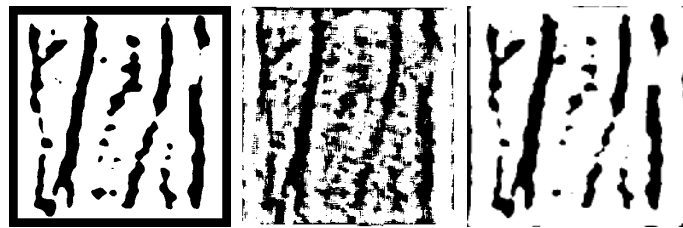


(e) Improved Niblack (f) Boundary (g) Gradient based

(46) Right hand of No.23 individual

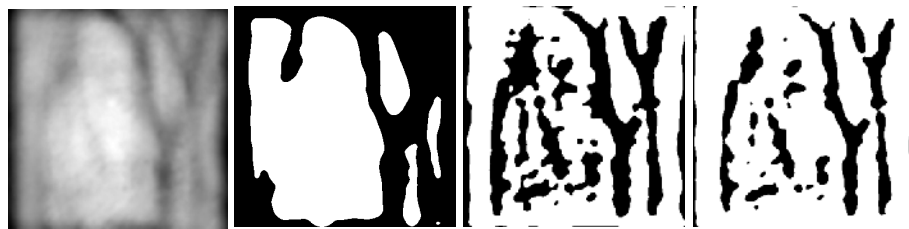


(a) CLAHE (b) Otsu (c) Threshold image (d) Niblack



(e) Improved Niblack (f) Boundary (g) Gradient based

(47) Left hand of No.24 individual

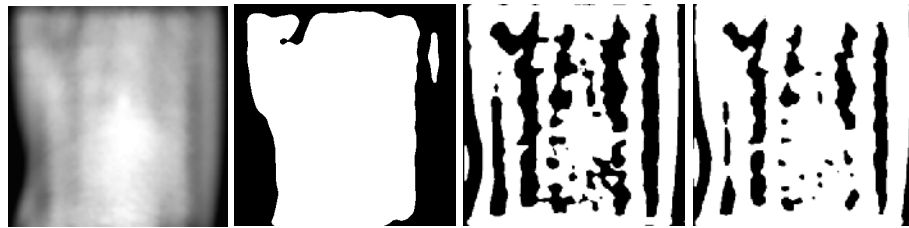


(a) CLAHE (b) Otsu (c) Threshold image (d) Niblack



(e) Improved Niblack (f) Boundary (g) Gradient based

(48) Right hand of No.24 individual

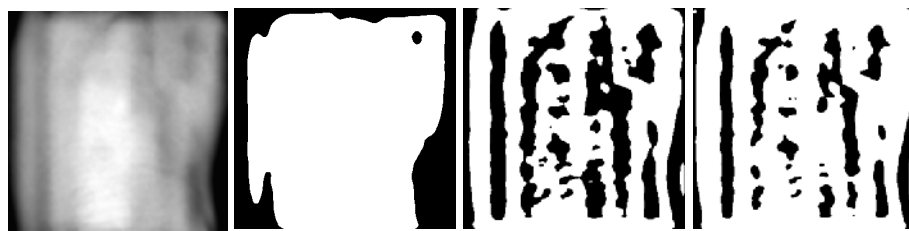


(a) CLAHE (b) Otsu (c) Threshold image (d) Niblack

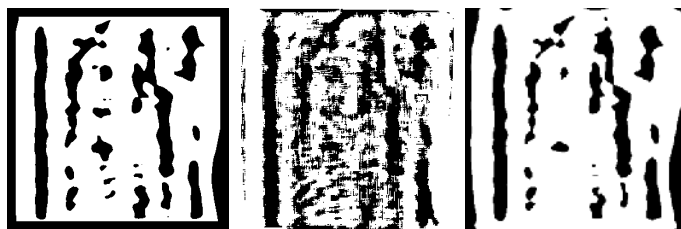


(e) Improved Niblack (f) Boundary (g) Gradient based

(49) Left hand of No.25 individual



(a) CLAHE (b) Otsu (c) Threshold image (d) Niblack



(e) Improved Niblack (f) Boundary (g) Gradient based

(50) Right hand of No.25 individual

Figure B-1 Results of segmentation methods

Appendix C. PUBLICATIONS

- [1] Wang, Y., Li, K., Cui, J., Shark, L. and Varley, M., *Study of Hand-dorsa Vein Recognition*, 6th International Conference on Intelligent Computing (ICIC'10), AUG 18-21, 2010 Changsha, CHINA (**EI20104313332457**)
- [2] Wang, Y., Li, K. and Cui, J., *Hand-dorsa Vein Recognition Based on Partition Local Binary Pattern*, 10th International Conference on Signal Processing (ICSP'10) Oct. 24-28, 2010, Beijing, CHINA (**EI20110213573899**)
- [3] Wang, Y., Li, K., Shark, L. and Varley, M., *Hand-dorsa Vein Recognition Based on Coded and Weighted Partition Local Binary Patterns*, International Conference on Hand-based Biometrics (ICHB2011), Nov. 17-18, 2011, Hong Kong. (**EI20120114651943**)
- [4] Wang, Y., Fan, Y., Liao, W., Li, K., Shark, L. and Varley, M., *Hand Vein Recognition Based on Multiple Keypoints Sets*, International Conference on Biometrics (ICB 2012), 2012, India (**EI20124015496759**)
- [5] Wang, Y., Yan, Q., Li, K., *Hand vein recognition based on multi-scale LBP and wavelet*, Proceedings of 2011 International Conference on Wavelet Analysis and Pattern Recognition (ICWAPR 2011), 2011, pp. 214-218 (**EI20114514486679**)
- [6] Cui, J., Wang, Y., Li, K., *DHV image registration using boundary optimisation*, 6th International Conference on Intelligent Computing (ICIC'10), AUG 18-21, 2010 Changsha, CHINA. (**EI20104313332458**)